

5-2016

# Direct band gap gallium antimonide phosphide (GaSbxP<sub>1-x</sub>) for solar fuels.

Harry Benjamin Russell  
*University of Louisville*

Follow this and additional works at: <https://ir.library.louisville.edu/etd>

Part of the [Electronic Devices and Semiconductor Manufacturing Commons](#), [Nanoscience and Nanotechnology Commons](#), [Other Chemical Engineering Commons](#), [Other Chemistry Commons](#), [Other Engineering Commons](#), [Other Engineering Science and Materials Commons](#), and the [Semiconductor and Optical Materials Commons](#)

---

## Recommended Citation

Russell, Harry Benjamin, "Direct band gap gallium antimonide phosphide (GaSbxP<sub>1-x</sub>) for solar fuels." (2016). *Electronic Theses and Dissertations*. Paper 2382.  
<https://doi.org/10.18297/etd/2382>

This Doctoral Dissertation is brought to you for free and open access by ThinkIR: The University of Louisville's Institutional Repository. It has been accepted for inclusion in Electronic Theses and Dissertations by an authorized administrator of ThinkIR: The University of Louisville's Institutional Repository. This title appears here courtesy of the author, who has retained all other copyrights. For more information, please contact [thinkir@louisville.edu](mailto:thinkir@louisville.edu).

DIRECT BAND GAP GALLIUM ANTIMONIDE PHOSPHIDE ( $\text{GaSb}_x\text{P}_{1-x}$ ) FOR  
SOLAR FUELS

By

Harry Benjamin Russell

Bachelor of Engineering, University of Louisville, 2009

Master of Engineering, University of Louisville, 2011

A Dissertation

Submitted to the Faculty of the  
J.B. Speed School of Engineering  
in Fulfillment of the Requirements  
for the Degree of

Doctor of Philosophy  
in Chemical Engineering

Department of Chemical Engineering  
University of Louisville  
Louisville, KY 40292

May 2016



DIRECT BAND GAP GALLIUM ANTIMONIDE PHOSPHIDE ( $\text{GaSb}_x\text{P}_{1-x}$ ) FOR  
SOLAR FUELS

By

Harry Benjamin Russell

Bachelor of Engineering, University of Louisville, 2009

Master of Engineering, University of Louisville, 2011

A Dissertation Approved on

April 22, 2016

By the Following Dissertation Committee

---

Dr. Mahendra Sunkara (Dissertation Director)

---

Dr. Xiao-an Fu

---

Dr. Thomas Starr

---

Dr. Jacek Jasinski

---

Dr. Shamus McNamara

---

Dr. Todd Deutsch

---

Dr. Madhu Menon

## ACKNOWLEDGEMENTS

First, I would like to thank Dr. Sunkara for all of the opportunities afforded to me during my research career at the University of Louisville. Dr. Sunkara took a chance on me when I was still finding my way in life and without his help I would not be in the position I am today.

Thanks also go to Dr. Fu, Dr. Starr, Dr. McNamara, Dr. Jasinski, Dr. Deutsch and Dr. Menon for serving on my thesis committee. My dissertation studies would not have been nearly as extensive without the expertise provided by each committee member. Special thanks go to Dr. Menon for providing DFT calculations that were pivotal in my research. Special thanks also go Hank Paxton for his fundamental role in building and operating the HVPE reactor with me, to Alejandro Martinez for performing PEC testing and to Dr. Jasinski for performing TEM measurements. I would also like to acknowledge all of my colleagues that I have worked with in both the CVD lab and Conn Center over my graduate research career. I have relied on all of you at times and appreciate all the help I have been given.

Finally, I would like to thank my loving family. Rhoniann, Gabriel, Lilian and Harry: Thank you for your daily support and encouragement even when times were tough. Mom and Dad: Without the hardwork and ethics you taught me I'd never have accomplished this. Daniel: Thank you for always believing in me and encouraging me to take chances.

## ABSTRACT

Direct Band Gap Gallium Antimonide Phosphide

(GaSb<sub>x</sub>P<sub>1-x</sub>) Alloys for Solar Fuels

Harry Benjamin Russell

April 22, 2016

Photoelectrochemical water splitting has been identified as a promising route for achieving sustainable energy future. However, semiconductor materials with the appropriate optical, electrical and electrochemical properties have yet to be discovered. In search of an appropriate semiconductor to fill this gap, GaSbP, a semiconductor never tested for PEC performance is proposed here and investigated. Density functional theory (DFT+U) techniques were utilized to predict band gap and band edge energetics for GaSbP alloys with low amount of antimony. The overall objective of this dissertation is to understand the suitability of GaSb<sub>x</sub>P<sub>1-x</sub> alloys for photoelectrochemical water splitting application. Specifically, the goals are to develop synthesis methods, grow GaSb<sub>x</sub>P<sub>1-x</sub> alloys, understand their optical and photoelectrochemical properties, and compare experimental values with theoretical predictions.

DFT+U calculations suggested that with less than 1% Sb incorporated into GaP, an indirect to direct band gap transition should occur. Furthermore, predictions with band edge positions for  $\text{GaSb}_x\text{P}_{1-x}$  alloys with small amount of Sb composition suggest band edge straddling of the water splitting reaction. Preliminary experiments were performed using reactive vapor transport in a microwave plasma reactor. The experiments primarily resulted in growing  $\text{GaSb}_x\text{P}_{1-x}$  nanowires. Extensive characterization using electron microscopy and X-ray diffraction and photoluminescence spectroscopy corroborated the predictions using DFT+U calculations. Initial experimentation utilized a plasma transport scheme of Ga and Sb metals with di-tert-butyl-phosphine gas on the reactor to synthesis  $\text{GaSb}_x\text{P}_{1-x}$  nanowires. Transmission Electron Microscopy (TEM) and X-ray Diffraction (XRD) confirmed ternary alloying of these  $\text{GaSb}_x\text{P}_{1-x}$  nanowires. Direct band gaps were observed between 1.7 eV and 2.2eV with  $\text{GaSb}_x\text{P}_{1-x}$  compositions between 3% and 6%. However, the method used here is not suitable for growing single crystal films.

In order to grow single crystal films on silicon substrates, a new reactor was designed and built for halide vapor phase epitaxy method. Experiments using Halide Vapor Phase Epitaxy (HVPE) reactor were conducted using silicon and sapphire substrates. Experiments using excessive Gallium yielded microwire morphologies. Further experiments with reduced Gallium precursor temperature allowed for growth of quality crystalline films on silicon substrate. The films grown at different temperatures exhibited different amounts of antimonide alloying. The resulting samples exhibited direct band gaps of 1.7 to 2.1 eV evidenced by UV-Vis diffuse reflectance spectroscopy..

Room temperature photoluminescence corroborated these findings. Photoelectrochemical studies of the HVPE grown samples show that they can be highly photoactive materials under the proper growth conditions. The best performing sample had saturated photovoltages of .75 eV and a photoactivity of 8 mA/cm<sup>2</sup> under unbiased conditions and 4 suns illumination. This photocurrent saturated to 11 mA/cm<sup>2</sup> at 1 V vs. Ag/AgCl external bias.

In summary, the work presented here provides fundamental insight into growth and properties of GaSbP alloy samples with low amount of Sb incorporation. The experimental data corroborates predictions by DFT+U technique in terms of indirect to direct band gap transition, band gap as a function of Sb incorporation and band edge energetics for photoelectrochemical water splitting. This work also provides first of its kind use of halide vapor phase epitaxy technique for the growth of GaSbP alloys. Photoactivity data suggests that these materials are highly promising for photoelectrochemical devices.



## TABLE OF CONTENTS

	PAGE
ACKNOWLEDGEMENTS.....	iii
ABSTRACT.....	iv
LIST OF	
FIGURES.....	x
CHAPTER	
1. INTRODUCTION.....	1
1.1 GLOBAL ENERGY CHALLENGE.....	1
1.2 SOLAR ENERGY .....	2
1.3 PHOTOELECTROCHEMICAL WATER SPLITTING.....	3
1.4 PROPOSED APPROACH.....	6
1.5 OBJECTIVES OF THIS STUDY.....	8
1.6 THESIS ORGANIZATION.....	9
2. BACKGROUND.....	11

2.1 WORKING PRINCIPLES OF THE PHOTOELECTROCHEMICAL	
WATER SPLITTING CELL.....	11
2.2 STATE OF THE ART SEMICONDUCTOR REVIEW FOR	
PHOTOELECTROCHEMICAL WATER SPLITTING.....	23
2.3 III-V NANOWIRES VS. EPITAXY.....	30
2.4 HALIDE VAPOR PHASE EPITAXY OF III-V'S.....	32
3. EXPERIMENTAL METHODS.....	35
3.1 COMPUTATION TECHNIQUES: DENSITY FUNCTIONAL THEORY..	35
3.2 REACTIVE VAPOR TRANSPORT METHOD FOR GROWING GASBP	
NANOWIRES.....	36
3.3 HALIDE VAPOR PHASE EPITAXY REACTOR.....	37
3.4 MATERIALS CHARACTERIZATION.....	56
3.5 ELECTROCHEMICAL AND PHOTOELECTROCHEMICAL	
CHARACTERIZATION .....	58
4. COMPUTATIONAL STUDIES AND EXPERIMENTAL VALIDATION OF	
GASBP ALLOYS.....	61
4.1 DENSITY FUNCTIONAL THEORY.....	61
4.2 GASBP AMORPHOUS NANOWIRES.....	64
4.3 SINGLE CRYSTAL GASBP NANOWIRES.....	67
5. HALIDE VAPOR PHASE EPITAXIAL AND PHOTOELECTROCHEMICAL	
CHARACTERIZATION OF GASBP FILMS.....	77
5.1 REACTION CHEMISTRY.....	77

5.2 SYNTHESIS AND MATERIALS CHARACTERIZATION OF HVPE GROWN GASBP.....	80
5.3 PHOTOELECTROCHEMICAL TESTING OF HVPE GROW GASBP.....	105
6. CONCLUSIONS.....	118
7. RECOMMENDATIONS FOR FUTURE EXPERIMENTATION.....	122
7.1 CHANGES WITH REACTOR DESIGN AND OPERATION.....	122
7.2 RECOMMENDED EXPERIMENTS USING HVPE.....	125
7.3 ELECTRICAL AND PEC DEVICE CHARACTERIZATION.....	125
REFERENCES.....	127
CURRICULUM VITAE.....	137

## LIST OF FIGURES

Figure 1.1 Band diagram schematics for (a) n-type Schottky, (b) p-type Schottky and (c) tandem PEC cell configurations	4
Figure 1.2 Band edge placement of GaSb, GaN, InP, GaInP <sub>2</sub> and GaP vs. with respect to the hydrogen evolution reaction and oxygen evolution reaction potentials	7
Figure 2.1. Standard AM1.0 and AM1.5 solar irradiation spectrum from the standard tables for solar spectral irradiances ASTM G173-03	14
Figure 2.2. Typical Schottky-type PEC water splitting testing cell	15
Figure 2.3: Voltage vs. distance plots for various SC and metal counter electrode band energy level positions with respect to the OER and HER redox levels. Figures 2.3a-d show band configuration of a non-working n-type semiconductor (a) before contact, (b) after equilibration with the electrolyte, (c) after illumination and (d) with an external bias to make the configuration functional for PEC water splitting.	20
Figure 3.1 An illustration of a reaction scheme attempted for HVPE	39
Figure 3.2 Reaction scheme including PCl <sub>3</sub> chemistry	39
Figure 3.3 Process flow diagram of custom-designed HVPE reactor	40
Figure 3.4 Photographs of the assembled reactor. The precursor boats for Ga and Sb are shown in (a) and (b). Process readouts and controllers are shown in (c). An overview of	

the reactor is shown in (d). The induction heater during operation is shown in (e). The $\text{PCl}_3$ bubbler is shown in (f).	42
Figure 3.5 (a) temperature controllers for the tube furnace and (b) temperature programming for tube furnace ramping.	44
Figure 3.6 Photographs showing induction heater, pyrometer and on/off controller in the HVPE reactor assembly.	46
Figure 3.7 (a) the $\text{PCl}_3$ bubbler assembly and (b) MKS Type 247 gas controller that controls gas flow rate and bubbler pressure.	47
Figure 3.8 Carbon susceptor with deposition from previous reaction.	50
Figure 3.9 Pressure control valve orifice before and after cleaning procedure.	51
Figure 3.10 Photograph of quartz vacuum compression adapter and diagrams showing the fitting before and after modification	54
Figure 3.11 Diagrams of set-up before and after modification.	55
Figure 4.1 A 216 atom Supercell of $\text{GaP}_{.963}\text{Sb}_{.037}$ optimized using DFT calculations and comparison of density of states diagrams for (b) GaP and (c) $\text{GaP}_{.963}\text{Sb}_{.037}$ showing the direct optical band gap transition.	62
Figure 4.2 (a) Change in band gap and (b) percent change in d-spacing for # of Sb atoms incorporated in the 216 atom supercell. Both plots were obtained from DFT calculations.	63
Figure 4.3 Valence band maximum and conduction band minimum positions calculated by the generalized Harrison's approach as a function of Sb concentration in $\text{Ga}(\text{Sb})\text{P}$ at $\text{pH} = 7$ alongside the redox potentials for the HER and OER.	65

Figure 4.4 HRTEM imaging of an amorphous nanowire that contains Ga, Sb, P, Cu and O. Figure 2b-c show 3 TEM-EDAX point source measurements along an nanowire indicating an antimony copper eutectic droplet led nanowire growth.

66

Figure 4.5 (a) A high resolution transmission electron micrograph of a  $\text{GaSb}_x\text{P}_{(1-x)}$  nanowire; (b) A scanning electron micrograph of  $\text{GaSb}_x\text{P}_{(1-x)}$  Nanowires; and (c) An EDS line scan for composition using transmission electron microscopy showing Ga, Sb and P concentration across a radial cross section of the  $\text{GaSb}_x\text{P}_{(1-x)}$  nanowire from part a.

67

Figure 4.6 X-Ray Diffraction pattern of  $\text{GaSb}_x\text{P}_{(1-x)}$  samples indicating alloy compositions. Individual concentrations were determined to be  $x_{\text{Sb}} = 0.121, 119, 106, 100$  and  $0.059$  (from top to bottom).

69

Figure 4.7 Tauc plot analysis for the direct allowed transition from UV-Vis diffuse reflectance for the  $\text{GaSb}_x\text{P}_{(1-x)}$  samples indicating direct band gap transitions from  $1.33 \text{ eV}$  up to  $1.72 \text{ eV}$ .

70

Figure 4.8 – (a) Visible photoluminescence spectra at liquid nitrogen temperature ( $77 \text{ K}$ ) for  $\text{GaSb}_x\text{P}_{(1-x)}$  alloy containing peaks at  $1.73$  and  $1.84 \text{ eV}$  and a peak at  $2.3 \text{ eV}$  for GaP control sample; (b) Visible photoluminescence from various regions (A–E) of  $\text{GaSb}_x\text{P}_{(1-x)}$  nanowire film sample at room temperature that exhibit peaks at  $1.74 \text{ eV}$  (A),  $1.77 \text{ eV}$  (B),  $1.84 \text{ eV}$  (C),  $1.89 \text{ eV}$  (D), and  $2.21 \text{ eV}$  (E).

72

Figure 4.9 – Raman of  $\text{GaSb}_x\text{P}_{(1-x)}$  against (a) GaSb and (b) GaP control samples. Major peaks for  $\text{GaSb}_x\text{P}_{(1-x)}$  are observed at  $201 \text{ cm}^{-1}$ ,  $356 \text{ cm}^{-1}$ ,  $390 \text{ cm}^{-1}$ ,  $417 \text{ cm}^{-1}$ ,  $464 \text{ cm}^{-1}$ ,  $637 \text{ cm}^{-1}$  and  $750 \text{ cm}^{-1}$ .

74

Figure 4.10 – Fundamental photoelectrochemical characterization including linear sweep voltammetry showing an approximate photocurrent density of  $40 \mu\text{A}/\text{cm}^2$  at  $-0.65 \text{ eV}$  (a), open circuit potential under chopped illumination indicating p-type conductivity (b) and unbiased 2 electrode chronoamperometry under chopped illumination showing approximately  $15 \mu\text{A}/\text{cm}^2$  photoactivity and confirming true water splitting. 75

Figure 5.1 – Photograph of reactor immediately following the induction heater zone. On the left, black and silver deposition can clearly be seen on the reactor tube, in the middle a thick gas cloud can clearly be seen in the quartz tube. 81

Figure 5.2 – Photography and electron microscopy for sample A3 grown. Sample was collected from quartz tube wall after attempting to deposit GaSbP at  $T_{\text{dep}} = 900^\circ\text{C}$ . (a) Photograph, (b) SEM and (c) TEM for A3-orange. (d) Photograph and (e) cross section SEM for A3-gray and (f) photograph and (g) SEM for A3-black. 84

Figure 5.3 XRD pattern for sample A3-gray and A3-black showing the 111-peak region for GaSb and GaP. Peaks can clearly be seen for sample A3-gray at approximately  $27.8^\circ$  and  $27.9^\circ$  that indicate compositions of  $\text{GaSb}_{0.17}\text{P}_{0.83}$  and  $\text{GaSb}_{0.13}\text{P}_{0.87}$  respectively. 85

Figure 5.4 Optical band gap properties of sample A3-gray. (a) Tauc plot of the n=2 direct allowed band gap transition indicating a  $1.72 \text{ eV}$  direct band gap and (b) Photoluminescence spectrum at 77K also indicating a  $1.72 \text{ eV}$  direct band gap. 86

Figure 5.5 (a) Photograph and (b-c) cross section SEM images of sample A4. A thickness of approximately 250 micrometers was observed. 88

Figure 5.6 Optical and structural characterization of sample A4. (a) Tauc plot for n=2 direct allowed band gap transition indicating a  $1.72 \text{ eV}$  direct band gap. (b) XRD pattern

showing the 111-peak region for GaSb and GaP. A peak is clearly observed at  $28.3^\circ$  indicating the sample is pure GaP. (c) Multiple photoluminescence measurements at different discrete locations on sample A4 indicating several direct band gap responses between 1.72 eV and 2.2 eV. 90

Figure 5.7 (a) Photograph and (b-c) cross section SEM images of sample A6. Faceted microwire geometries are clearly observed with diameters up to  $5\mu\text{m}$  91

Figure 5.8 (a) Tauc plot for the  $n=2$  direct allowed band gap transition band gap transition for sample A6 indicating a 1.9 eV direct band gap and (b) multiple photoluminescence measurements performed at 77 K at different discrete locations on sample A6 indicating several direct band gap responses between 1.7 eV and 2.2 eV. 92

Figure 5.9 Normalized XRD data of the region around the (111) peaks of GaP and GaSb for samples A4 through A12. Peaks are clearly observed from  $27.8^\circ$  up to  $28.3^\circ$  indicating compositions between  $\text{GaSb}_{.037}\text{P}_{.963}$  to  $\text{GaSb}_{.127}\text{P}_{.833}$ . Samples A4 and A12 show XRD peaks identical to GaP. 93

Figure 5.10 (a,c) Photographs and (b,d) cross section SEM images of samples A8 and A9 respectively. Both samples exhibit microwire conglomerate geometries with thicknesses of approximately  $150\mu\text{m}$  and more densely packed growth near the growth interface. 95

Figure 5.11 Optical measurements for samples A8 and A9. (a,b) Tauc plots for the  $n=2$  direct allowed band gap transition for samples A8 and A9, respectively, indicating a 1.3 eV and 1.5 eV direct band gaps for sample A8 and 1.2 eV to 1.6 eV direct band gaps for sample A9. (c,d) Multiple photoluminescence measurements performed at 77 K at



different discrete locations on samples A8 and A9, respectively, indicating several direct band gap responses between 1.7 eV and 2.2 eV in each sample. 97

Figure 5.12 (a,c) Photographs and (b,d) cross section SEM images of samples A10 and A11 respectively. Both samples exhibit microwire conglomerate geometries with thicknesses of approximately 200  $\mu\text{m}$  and highly oriented crystallinity with boulder-like features in excess of 10  $\mu\text{m}$ . 98

Figure 5.13 Optical measurements for samples A10 and A11. (a,b) Tauc plots for the  $n=2$  direct allowed band gap transition for samples A10 and A11, respectively, indicating a 1.3 eV and 1.5 eV direct band gaps for sample A8 and 1.2 eV to 1.6 eV direct band gaps for sample A9. (c,d) Multiple photoluminescence measurements performed at 77 K at different discrete locations on samples A10 and A11, respectively, indicating several direct band gap responses between 1.7 eV and 2.2 eV in each sample. 100

Figure 5.14 (a) Photograph and (b,c) cross section SEM images of sample A12. The sample exhibits single crystal features in excess of 30  $\mu\text{m}$  and displays clear evidence of epitaxial growth at the growth interface. The marks perpendicular to the growth interface where the crystal was cleaved are another clear sign of the single crystallinity exhibited. 102

Figure 5.15 Optical measurements for sample A12. (a) Tauc plot for the  $n=2$  direct allowed band gap transition for samples A12 indicating a 2.15 eV direct band gap. (b) Multiple photoluminescence measurements performed at 77 K at different discrete locations on samples A12 indicating several direct band gap responses between 1.7 eV and 2.15 eV. 103

Figure 5.16 – Fundamental PEC studies of sample A4 at 4 suns illumination in sodium sulfate solution (pH = 9). (a) OCP under chopped illumination for 200 seconds indicating n-type conductivity and (b) chopped illumination LSV measurements exhibiting approximately  $.5 \text{ mA/cm}^2$  photoactivity under bias and high background currents in the dark. 107

Figure 5.17 Fundamental PEC studies for samples A6 with bottom and top contacts, respectively, at 4 suns illumination in sodium sulfate solution (pH = 10). (a,c) OCP under chopped illumination for 200+ seconds indicating n-type conductivity for both samples and (b,d) chopped illumination LSV measurements exhibiting approximately  $0.2 \text{ mA/cm}^2$  and  $0.15 \text{ mA/cm}^2$  maximum photocurrents under bias respectively. 109

Figure 5.18 Fundamental PEC studies for samples A8 and A9, respectively, at 4 suns illumination in 3M sulfuric acid (pH = 0). (a,c) OCP under chopped illumination for 500+ seconds indicating n-type conductivity for both samples and (b,d) chopped illumination LSV measurements exhibiting approximately  $3 \text{ mA/cm}^2$  and  $0.2 \text{ mA/cm}^2$  maximum photocurrents under bias respectively. 110

Figure 5.19 Fundamental PEC studies for samples A10 and A11, respectively, at 4 suns illumination in 3M sulfuric acid (pH = 0). (a,d) OCP under chopped illumination for 500+ seconds indicating n-type conductivity for both samples. (b) Unbiased two-electrode chronoamperometry measurements under chopped illumination for sample A10 exhibiting steady photocurrents between  $4 \text{ mA/cm}^2$  and  $8 \text{ mA/cm}^2$  for 10 minutes. (b,e) chopped illumination LSV measurements exhibiting approximately  $11 \text{ mA/cm}^2$  and  $0.02 \text{ mA/cm}^2$  maximum photocurrents under bias respectively. 112

Figure 5.20 Fundamental PEC studies for sample A12 at 4 suns illumination in 3M sulfuric acid (pH = 0). (a) OCP under chopped illumination for 500+ seconds indicating n-type conductivity and (b) chopped illumination LSV measurements showed approximately 0.05 mA/cm<sup>2</sup> maximum photocurrents under bias. 113

Figure 6.21 – Approximate band edge placement for each sample based upon the observed flatband potentials and band gaps. All samples exhibit n-type conductivity thus the observed flatband potential is used to place the conduction band for the material. The band gap is then used to determine the position of the valence band. The green marker indicates the conduction band energy level, the red marker represents the valence band level based upon the lowest observed bandgap and the blue marker represents the valence band level for the highest observed band gap. 115

Figure 7.1 – Reactor scheme after implementation of proposed changes 124

# CHAPTER 1

## INTRODUCTION

### 1.1 Global energy challenge

The production of clean fuels by utilizing solar energy is one of the most important milestones on the road to a sustainable energy future<sup>7</sup>. Globally, power is currently consumed at a rate of approximately 15 TW and only approximately 11% of that energy came from renewable energy sources according to a report by the US Energy Information Administration (EIA) in 2014. World energy consumption is expected to double by 2050 due to population rise and higher energy demand from developing countries. CO<sub>2</sub> thresholds of 350 ppm and 450 ppm have been proposed by climate scientists as maximum CO<sub>2</sub> limits that need to be observed in order to mitigate catastrophic and potentially irreversible consequences to the earth's climate<sup>8,9</sup>. Carbon dioxide levels have risen from approximately 310 ppm in the 1950's and surpassed the 350 ppm limit in the 1990's. Most recently in August of 2014, a reading of 397.01 ppm was reported by the Mauna Loa Observatory in Hawaii. At the current rate of CO<sub>2</sub> production without ambitious CO<sub>2</sub> mitigation policies the atmospheric concentration of greenhouse gases is expected to reach 685 ppm by 2050. Such a significant rise in greenhouse gas levels will undoubtedly result in changes in patterns of precipitation, glacier liquefaction, sea-level rise and extreme weather conditions. Thus, it is imperative

to the survival of the human race and all other living creatures on earth that fossil fuels be replaced by sustainable energy sources that are free of greenhouse gas emissions.

Many renewable sources have been suggested and researched to provide carbon free alternatives to fossil fuels. Hydro, wave, geothermal and wind renewable energy sources are location based. Biofuels put a strain on agriculture, still have CO<sub>2</sub> emissions when used and typical plants can only convert 1% of incoming light. Nuclear reactors still have waste cleanup once decommissioned and are susceptible to natural disasters such as those recently seen in Japan.

## 1.2 Solar Energy

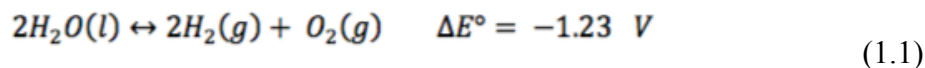
With over 120,000 Terawatts of solar radiation incident to the surface of the Earth, there is no other source of energy capable of providing clean sustainable energy close to that of the Sun. Even if this energy was harnessed through the use of photovoltaics, it is an intermittent source and ways of storing the energy for use at night or on cloudy days is necessary. Short of pumping water uphill to re-use as hydro electricity at night, the only way to store this energy is in the form chemical bonds. Thus, large-scale production of solar hydrogen is proposed as a greenhouse gas free and sustainable form of energy to meet the world's energy demand.

Solar hydrogen can be accomplished by many methods including solar-thermochemical, photosynthetic microbes, photovoltaic-electrolysis and photoelectrochemical (PEC) water splitting<sup>4</sup>. Photovoltaic-electrolysis is the most practical method of sustainable hydrogen production at this time but requires two systems to produce hydrogen. In comparison, direct water splitting using a semiconductor

electrode has several advantages: (a) the electrode fabrication may or may not require certain processing steps necessary for making a complete photovoltaic cell; (b) theoretical maximum efficiency of direct water splitting using a semiconductor electrode can exceed that of non-tandem type PV + electrolysis; (c) no need for wiring for flow of electrons; and (d) allows many potential configurations for PEC reactors.

### 1.3 Photoelectrochemical Water Splitting

PEC water splitting is the most researched of the solar fuel generation routes and has even been defined in past research as the “Holy Grail” of electrochemistry<sup>10</sup>. This method of renewable hydrogen generation works by absorbing incoming light utilizing a semiconductor photoabsorber and converting that energy for direct use in the water splitting reaction shown in equation 1.1.



This technology is, however, still in the materials research phase as new and affordable semiconductor materials with the appropriate band gap, band edge placement, electron mobility, reaction kinetics and chemical stability are still greatly needed to meet the benchmark efficiency of 25% set by the Department of Energy by 2025<sup>11</sup>.

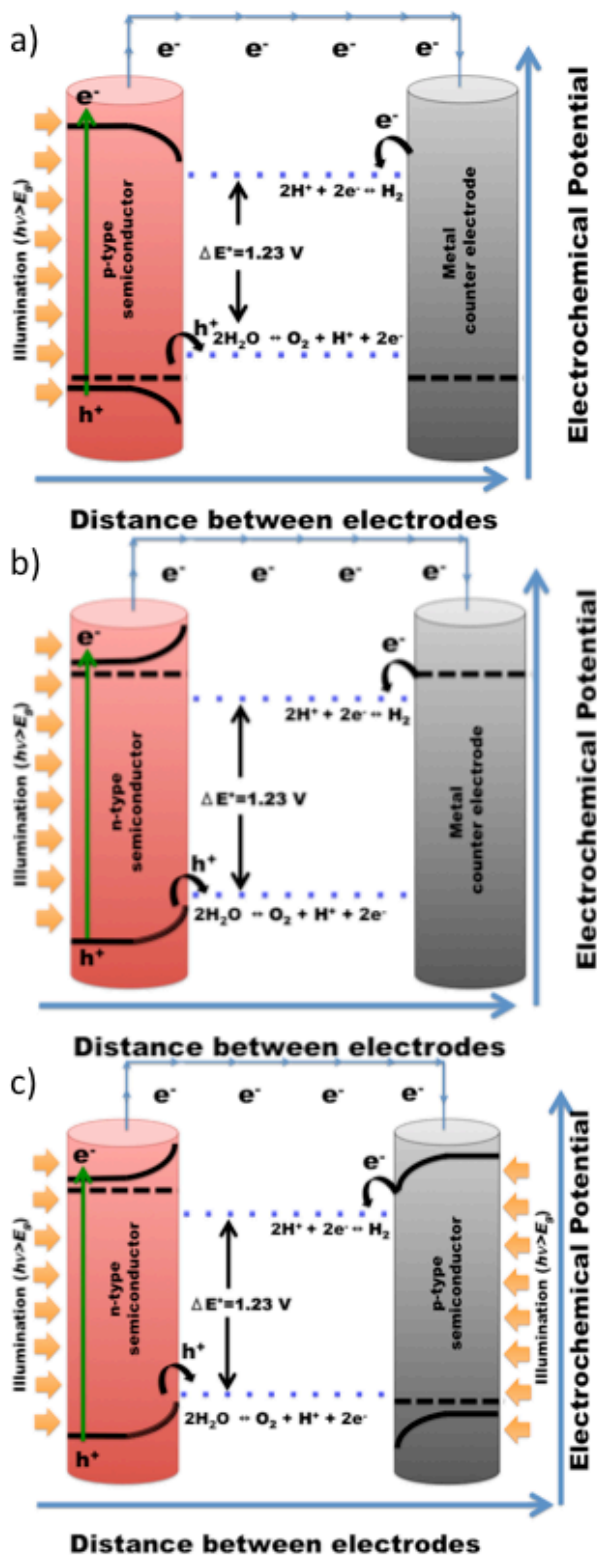


FIGURE 1.1 – Band diagram schematics for (a) n-type Schottky, (b) p-type Schottky and (c) tandem PEC cell configurations

PEC water splitting can be done utilizing many different device configurations. Most important for our research are the single semiconductor Schottky device and the two semiconductor tandem device<sup>4</sup>. For a single semiconductor Schottky device, the band edges of the semiconductor material should straddle the hydrogen evolution and oxygen evolution reactions. Specifically, for a p-type semiconductor, the conduction band must be higher than the HER and the Fermi level lower than the OER as shown in Figure 1.1a. Vice versa, for an n-type semiconductor the valence band should be lower than the OER and the Fermi level higher than the HER as shown in figure 1.1b. Band gap energies of 1.6-2.2 eV are required in order to straddle these potentials, overcome overpotentials required to perform these reactions, compensate for losses within the semiconductor and

absorb as much of the visible light spectrum as possible. The semiconductor is then ohmically contacted with an anode such as ruthenium oxide for a p-type cell or cathode such as platinum for n-type cells. For dual semiconductor tandem devices, two semiconductors are combined in order to perform the HER on the photocathode and the OER on the photoanode as shown in Figure 1.1c. By using two ohmically contacted semiconductors, lower band gap energies can be used and more of the solar spectrum can be absorbed between the two semiconductors. Ideal band gap energies required for a tandem cell are 1.0 eV and 1.7 eV.

To this day, the best performing semiconductor materials for PEC water splitting have been alloys formed by elements from groups III and V from the periodic table and are referred to as III-V's hereafter. The champion semiconductor chosen as the photoabsorber for PEC water splitting has been GaInP<sub>2</sub>. It has a direct band gap of 1.83 eV but its band energetics are not properly aligned to the water splitting reaction as shown in figure 1.2. As such, Turner et al synthesized the material with a monolithic GaAs pn-junction incorporated into the device structure in order to provide the proper bias to overcome the band misalignment<sup>5</sup>. The resulting device achieved 12.4% solar to hydrogen (STH) efficiency. Similarly, the final working PEC water splitting prototype presented by the Joint Center for Artificial Photosynthesis (JCAP) in 2015 utilized a GaInP<sub>2</sub>/GaAs multijunction photoabsorber approach and achieved 10% STH efficiency over 80 hours of continuous operation<sup>12</sup>. Many other III-V ternary alloys have touted tunable band gaps with the ability to straddle the water splitting redox reactions but have not exhibited efficient water splitting. For example, InGaN has a direct tunable band gap that can be readily synthesized throughout the ternary composition range<sup>13</sup>. The best



water splitting performance observed from InGaN has only reached 1.8% STH however<sup>14</sup>.

#### 1.4 Proposed approach

As discussed above, to date, the best performing PEC devices have contained high quality III-V photoabsorber semiconductors.<sup>5,12</sup> All of the binary III-V materials and many of the ternary and quaternary III-V alloys have been thoroughly examined for PEC water splitting. On the other hand, there are still a few of these systems that have not been researched for their use as band gap engineered semiconductors for solar fuels. One such of these ternary alloys is GaSbP. GaP has a 2.3 eV indirect band gap with favorable band edge characteristics but poor charge carrier conductivities and light absorption properties.<sup>15-17</sup> GaSb has a 0.7 eV direct band gap with favorable carrier conductivities but the band gap is too narrow to be used for water splitting<sup>18</sup>. The approximate semiconductor band edges of GaP and GaSb are shown with respect to the water splitting reaction in Figure 1.2. Also, from previous research with GaSbN, it has been shown that a minimal incorporation of Sb into GaN, dramatic changes in the band characteristics were observed.<sup>19</sup> The main idea is that if GaP is alloyed with antimony in the dilute antimonide regime, it is possible to produce direct band gap semiconductors based on  $\text{GaSb}_x\text{P}_{(1-x)}$  alloys that can fully straddle the water splitting reactions. Unlike  $\text{GaSb}_x\text{N}_{1-x}$  alloys, the sizes of Sb with P are closer which should not result in drastic band gap reduction in  $\text{GaSb}_x\text{P}_{1-x}$  with small amounts of Sb. At the same time, alloying in the dilute antimonide regime should lead to an indirect to direct band gap transition and modification of optical absorption properties without introducing deep level trap states.

Most importantly, such alloys can easily be grown single crystal epilayers on to silicon substrates due to allowable lattice mismatch. GaSbP has been the subject of a few studies and as such the dilute GaSb incorporation regime of GaSbP has not been studied.

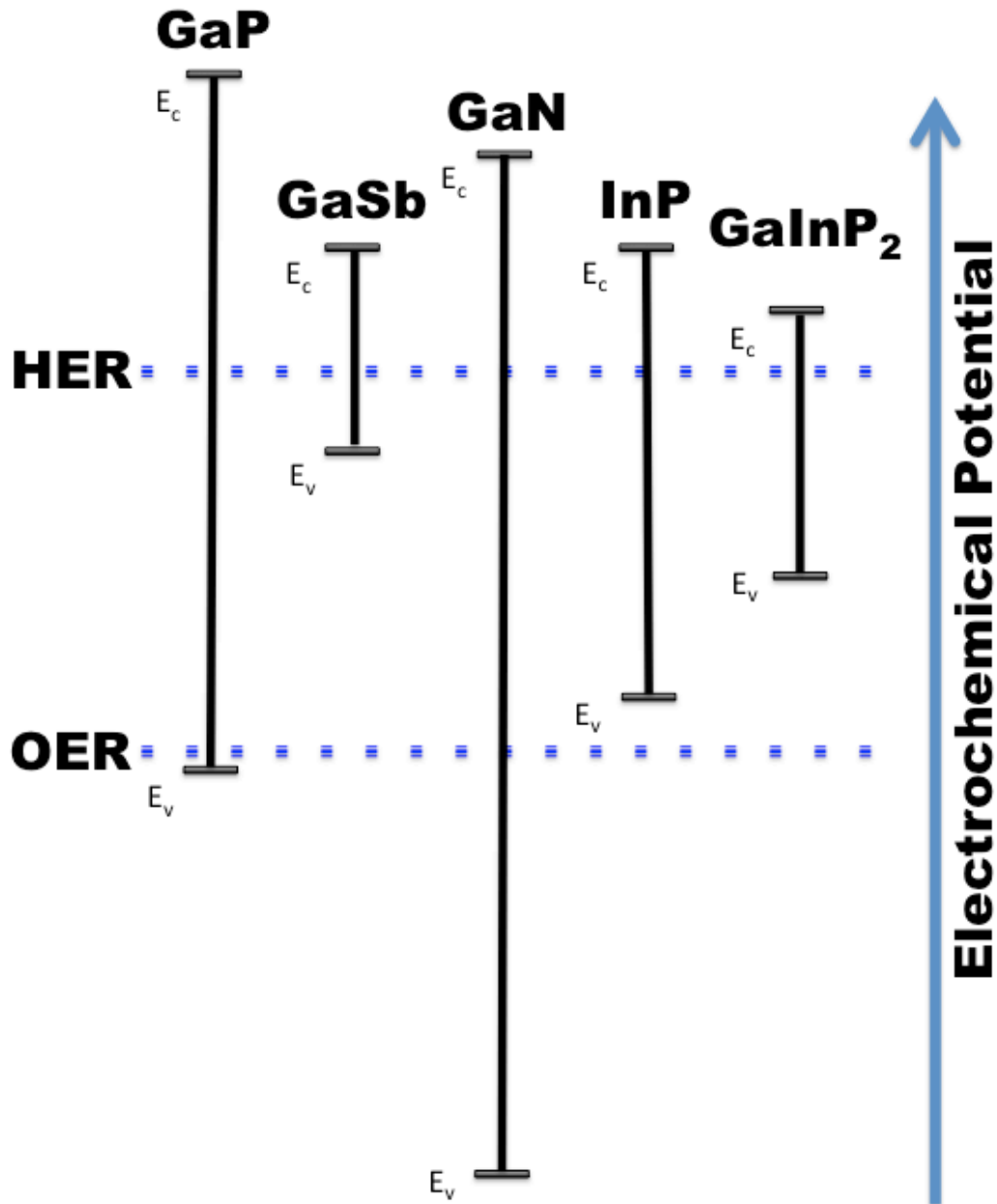


Figure 1.2 – Band edge placement of GaSb<sup>1</sup>, GaN<sup>3</sup>, InP<sup>4</sup>, GaInP<sub>2</sub><sup>5</sup> and GaP<sup>6</sup> with respect to the hydrogen evolution reaction and oxygen evolution reaction potentials.

In order to understand the amount of antimonide alloying needed for indirect to direct band gap transition, Density Functional Theory (DFT+U) calculations were implemented. The results showed that with less than 1% incorporation of GaSb into GaP, a direct band gap transition is observed. Furthermore, the ternary alloy should straddle the water splitting reaction at compositions up to 3% GaSb. Guided by these calculations, we propose the gallium antimonide phosphide ternary alloy system as a semiconductor system potentially capable of meeting the known requirements for efficient photoelectrochemical water splitting.

### 1.5 Objectives of this study

The primary objective of this project is the development of the III-V ternary alloy semiconductor,  $\text{GaSb}_x\text{P}_{1-x}$ , as the working electrode for an efficient photoelectrochemical water splitting device. Specific goals include the following:

- Develop methods for synthesis of GaSbP alloys both in terms of single crystal nanowires (NW) and films.
- Design and build a HVPE reactor to synthesize uniform composition high quality thin film alloys of varying compositions of GaSbP.
- Investigate process conditions for growing GaSbP epilayers on silicon substrates.
- Understand structure-property relationships for GaSbP semiconductors as a function of antimonide composition and compare the experimental data to that predicted using DFT+U techniques

- Investigate photoelectrochemical properties of the  $\text{GaSb}_x\text{P}_{1-x}$  to understand the conductivity type of as-synthesized films, onset potential and photoactivity for the synthesized films.

HVPE is chosen as our primary growth technique because of high growth rates and cheaper precursors than more common III-V growth methods such as metalorganic chemical vapor deposition and molecular beam epitaxy leading to a process that is highly economical and practical.

## 1.6 Thesis organization

The dissertation is organized into eight distinct chapters.

- Chapter 1 provides motivation and rationale for the research path undertaken in this dissertation. The motivation for needing a renewable fuel source, choosing PEC water splitting as the method to accomplish this and reasoning for synthesizing  $\text{GaSbP}$  as the photoabsorber for this cell are all discussed. Furthermore, the objectives to be accomplished during this dissertation are stated.
- Chapter 2 gives both a theoretical and experimental background of PEC water splitting and the many approaches that have been undertaken to perform it.
- Chapter 3 explains the equipment and methods used for all experimental techniques including synthesis, materials characterization and photoelectrochemical testing. The rationale and motivation behind utilizing HVPE and reasoning for the way in which the reactor was built is also discussed.

- Chapter 4 discusses the preliminary studies done to motivate growth of GaSbP via HVPE including DFT+U calculations, co-evaporative synthesis of amorphous GaSbP NWs and plasma transport synthesis of single crystal GaSbP NWs.
- Chapter 5 contains the results of HVPE growth and discussion of those results.
- Chapter 6 contains the conclusions to be made from these results.
- Chapter 7 will discuss future recommendations for experiments utilizing GaSbP and HVPE.

## CHAPTER 2

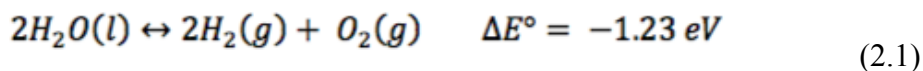
### BACKGROUND

In this chapter, a thorough background of PEC water splitting including the working principles, semiconductor classes that have been researched and state-of-the-art materials in the field is presented. This review clearly shows that III-V materials have been the best performing class of materials to date and that ternary III-V's provide the ability to grow high-quality, tunable band gap semiconductors that may have the ideal characteristics for PEC water splitting. This review of semiconductor classes provides the rationale for investigating GaSbP for water splitting. Also the advantages and disadvantages of having nanowire/microwire architectures versus epitaxial films for PEC water splitting. Finally, the progress and challenges in using HVPE method for growing single crystal quality, III-V materials is reviewed.

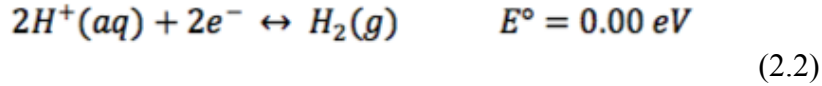
#### 2.1 Working principles of the PEC water splitting cell

##### Photoelectrolysis

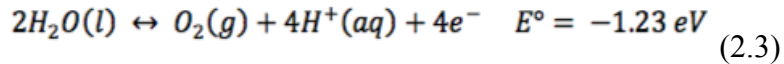
True PEC water splitting was first accomplished by Fujishima and Honda in 1972 via the catalysis of  $\text{TiO}_2$ .<sup>20</sup> The full reaction is written as:



The water splitting reaction consists of two half-reactions that take place at separate electrodes. Reduction occurs at the cathode, forming gaseous hydrogen via the hydrogen evolution reaction HER, which proceeds as follows:



The other half the reaction occurs at the anode where oxygen is released via the OER as follows:



By virtue of the two reactions occurring at separate electrodes, hydrogen and oxygen are capable of being evolved separately, captured and used later.

Water splitting is a non-spontaneous reaction requiring a minimum  $\Delta G = 237.2 \text{ kJ/mol}$  or  $E_{rxn}^\circ = -1.23 \text{ V}$  to carry forth. Utilizing the Planck relation, the required wavelengths to provide 1.23 eV or more energy can be obtained as shown below.

$$\lambda = hc/eE, c = 2.998 * 10^{17} \frac{nm}{s}, h = 6.625 * 10^{-34}, e = 1.60 * 10^{-19} C \quad (2.4)$$

(Where, e is the electronic charge magnitude, E is the energy of the photon in eV, h is Planck's constant, c is the speed of light under vacuum and  $\lambda$  is the photon wavelength in nm).

Based upon the above relationship, wavelengths equal or less than 1010 nm will provide 1.23 eV or more energy is required to generate the energy necessary to drive the water

splitting reaction. The Earth's atmosphere filters out certain wavelengths of the solar spectrum and according to the Beer-Lambert law the intensity of solar radiation decreases exponentially with distance. To accommodate for this, the Air Mass standard was developed and is referred to as "AM-X" with "X" representing the air mass coefficient and can be determined by the following correlation.

$$X = \frac{I}{I_0} = \frac{I_0}{I_0 \cos\theta} = \frac{1}{\cos\theta} \quad (2.5)$$

Where  $I$  is the light intensity after it has passed a certain distance through the atmosphere,  $I_0$  is the intensity of light prior to reaching the atmosphere and  $\theta$  is the angle between the light path and a point on earth. The most commonly used air mass standards are AM0, AM1 and AM1.5 which were measured in the NIST G173-03 standard<sup>2</sup>. AM0 represents the solar flux to be expected in space without the earth's atmosphere to interfere. AM1 represents the solar flux at the point exactly normal to the surface of the earth. AM1.5 represents the average solar flux at 37° incident to the earth during the day and is the standard spectrum used for solar testing. The AM0, AM1 and AM1.5G spectrum is shown in Figure 2.1<sup>2</sup>.



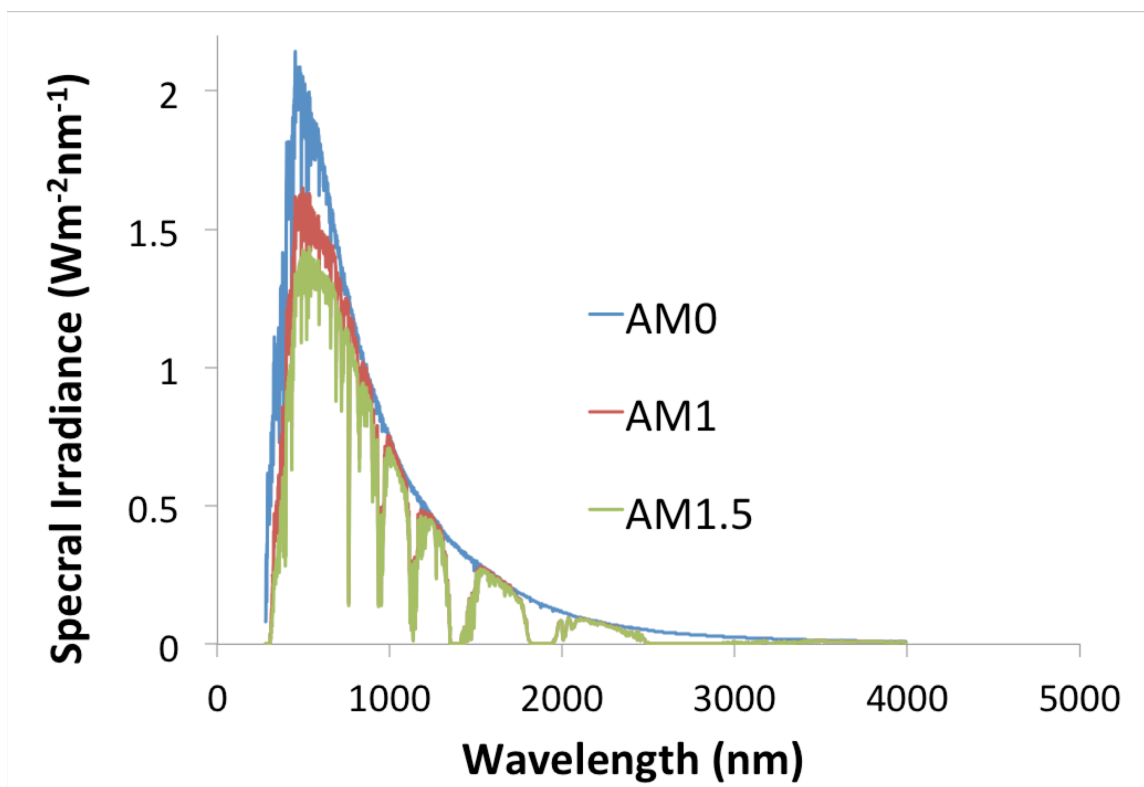


Figure 2.1. Standard AM0, AM1 and AM1.5 solar irradiation spectrum from the standard tables for solar spectral irradiances ASTM G173-03.<sup>2</sup>

Energy can be provided for PEC water splitting by utilizing the band gap of a semiconductor to absorb photons with sufficient energy. In a basic Schottky type PEC water splitting cell, a single semiconductor is used as either the photo-anode to drive the OER or photo-cathode to drive the HER. A more in depth discussion of semiconductor principles will be discussed later in this chapter. When testing this type of PEC cell, the semiconductor is designated as the working electrode (WE) while the catalytic metal used for the other electrode is designated as the counter electrode (CE). To understand at what relative potential reactions are occurring, a reference electrode (RE) such as Ag/AgCl is used as the third electrode. A basic three-electrode photoelectrochemical water splitting

setup is shown in Figure 2.2.

With the RE, bias is applied to the WE relative to the known reference potential based on RE used so that the working voltage of the WE can be known. Under illumination,

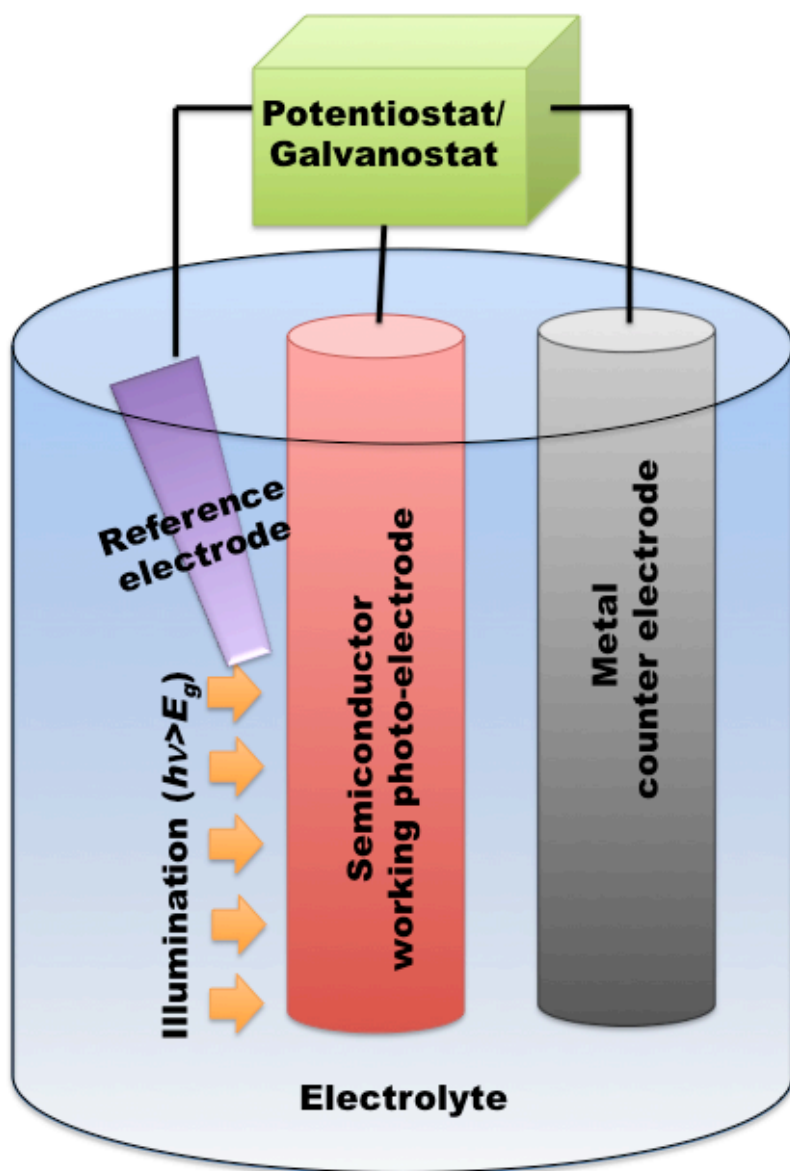


Figure 2.2. Typical Schottky-type PEC water splitting testing cell

photons are absorbed by the semiconductor WE, split into electron-hole pairs (ehp) and utilized between the WE and CE to split water.

## Semiconductor/electrolyte interface and the working PEC cell

The most basic water splitting PEC cell arrangement is one containing a single semiconductor. This type of configuration is referred to as a Schottky type PEC watersplitting cell. More advanced multijunction cells are possible and provide increased theoretical performances due to increased absorption and built in layers to provide built-in bias. As such, only the principles of single Schottky-type interaction will be discussed here.

When contact takes place between a semiconductor and electrolyte, the Fermi levels of both the semiconductor and electrolyte equilibrate with each other<sup>21,22</sup>. For discussion, a schottky type PEC water splitting cell with an n-type semiconductor photoanode and a metal cathode will be considered. When considering an electrochemical interaction, it is helpful to utilize the electrochemical scale where voltage is referred relative to the normal hydrogen electrode (NHE). All reference to energy level for the rest of this chapter will be in regard to the electrochemical scale. In this typical Schottky type configuration, the conduction and valence band energy levels need to straddle the HER and OER redox levels for un-assisted water splitting. When contact is made between the SC and electrolyte, a capacitance is formed at the interface causing a positive charge to accumulate at the surface of the semiconductor. This capacitance causes a Helmholtz layer in the electrolyte to be formed as the negative ions in the electrolyte are attracted to positive charges at the semiconductor interface. Further discussion of this double layer can be found in the literature<sup>23-25</sup>. It is due to this layer that the energy band levels stay pinned at the SC/electrolyte interface and don't change during electrochemical reaction. This energy level pinning is different for each

individual semiconductor/electrolyte system. A change in the Fermi level of the semiconductor also results in a change in the bulk positions of the conduction and valence bands of the material, each shifting equally. When a shift like this occurs, a bending of the energy band levels occurs between the bulk of the semiconductor and electrolyte interface resulting in a space charge region being formed with an electric field attracting the negative ions to the interface. The direction of band bending has a direction determined by the Fermi band energy level of the SC compared to that of the redox potential of the electrolyte. In an n-type semiconductor, the OER redox potential is positive of the semiconductor Fermi level. Thus, whenever equilibration occurs between the semiconductor-electrolyte interface (SCEI) a negative shift in bands occurs.

This band bending creates a favorable pathway for photogenerated holes to be used by the OER at the SCEI while electrons are driven into the bulk of the semiconductor and ultimately to the metal cathode in order to provide electrons for the HER. This clearly illustrates that PEC water splitting at the SCEI is a minority carrier driven process. The catalytic metal material used as the counter electrode will have a density of carriers that is orders of magnitude greater than the SC and has the same Fermi level of the bulk SC. Under illumination, charges are generated that are opposite in charge to that of the electric field within the space charge region. This causes flattening of the bands. Under saturated illumination, these bands completely unbend to an energy level known as the flat band potential ( $U_{fb}$ ) of the semiconductor. In an n-type semiconductor,  $U_{fb}$  is the maximum possible Fermi level under saturated illumination in the semiconductor without applying external bias. For p-type semiconductors,  $U_{fb}$  is the minimum possible Fermi level under saturated illumination without applying external

bias.

Figure 2.3 shows voltage vs. distance diagrams for both working and non-working semiconductor configurations for PEC water splitting. For n-type semiconductors, in order to provide electrons thermodynamically capable of driving the HER at the metal cathode, the Fermi level of the cathode needs to be at a higher potential than the HER, therefore the Fermi level of the SC needs to be at this same energy level under illumination. Figure 2.3a-d show an n-type semiconductor that has the appropriate band straddling to perform water splitting but requires some form of external bias because the flat band potential is too high to easily provide electrons to the metal cathode to perform the HER. Figure 2.3a shows the band edge positions of the respective PEC cell components prior to SC/electrolyte contact though the metal cathode/electrolyte contact has been made. The semiconductor's conduction, valence and flat band potentials are shown with respect to the HER and OER redox levels and the cathode Fermi level has equilibrated to that of the electrolyte redox potentials<sup>21,26</sup>. Figure 2.3b shows the energy levels of the SCEI after contact has been made and equilibration has occurred. At the SCEI, the conduction band and valence band energy levels are pinned at the same energy as before contact. On the other hand, the Fermi level of the semiconductor equilibrates with that of the electrolyte and this causes the conduction band and valence band energy levels in the bulk of the semiconductor to shift or bend with the Fermi energy level an amount equal to the difference between the electrolyte Fermi level and semiconductor flat band potential. Figure 2.3c shows the SCEI band energy levels after illumination. Ehps are created and the holes generated have an immediately favorable energetic pathway to participate in the OER. The electrons

ejected into the conduction band flow through the back contact to the metal cathode whose Fermi level is at an energy level too low to drive the HER. Figure 2.3d shows the same semiconductor/cathode configuration except with a provided external bias. The bias is in a direction that gives the metal cathode a Fermi level higher than the HER, thus providing a favorable pathway for electrons to be used by the HER. Figure 2.3e shows the ideal n-type semiconductor band energies to drive spontaneous water splitting under illumination. The conduction and valence bands straddle the HER and OER and the flat band potential is at a higher energy level than the HER. Upon equilibration with the electrolyte and illumination, the Fermi level of the SC and subsequently the metal cathode provides a favorable energetic pathway to provide electrons to the HER. Figure 2.3f shows the ideal p-type band energy level configuration for Schottky type PEC water splitting. The conduction and valence bands straddle the HER and OER just as in the case of the n-type electrode and the flatband potential is at an energy level slightly higher than the OER. Ehp's are created and electrons have an immediate favorable energetic pathway to drive the HER at the semiconductor surface. Holes are driven to the metal cathode where the Fermi level is at an energy level favorable to drive the OER.

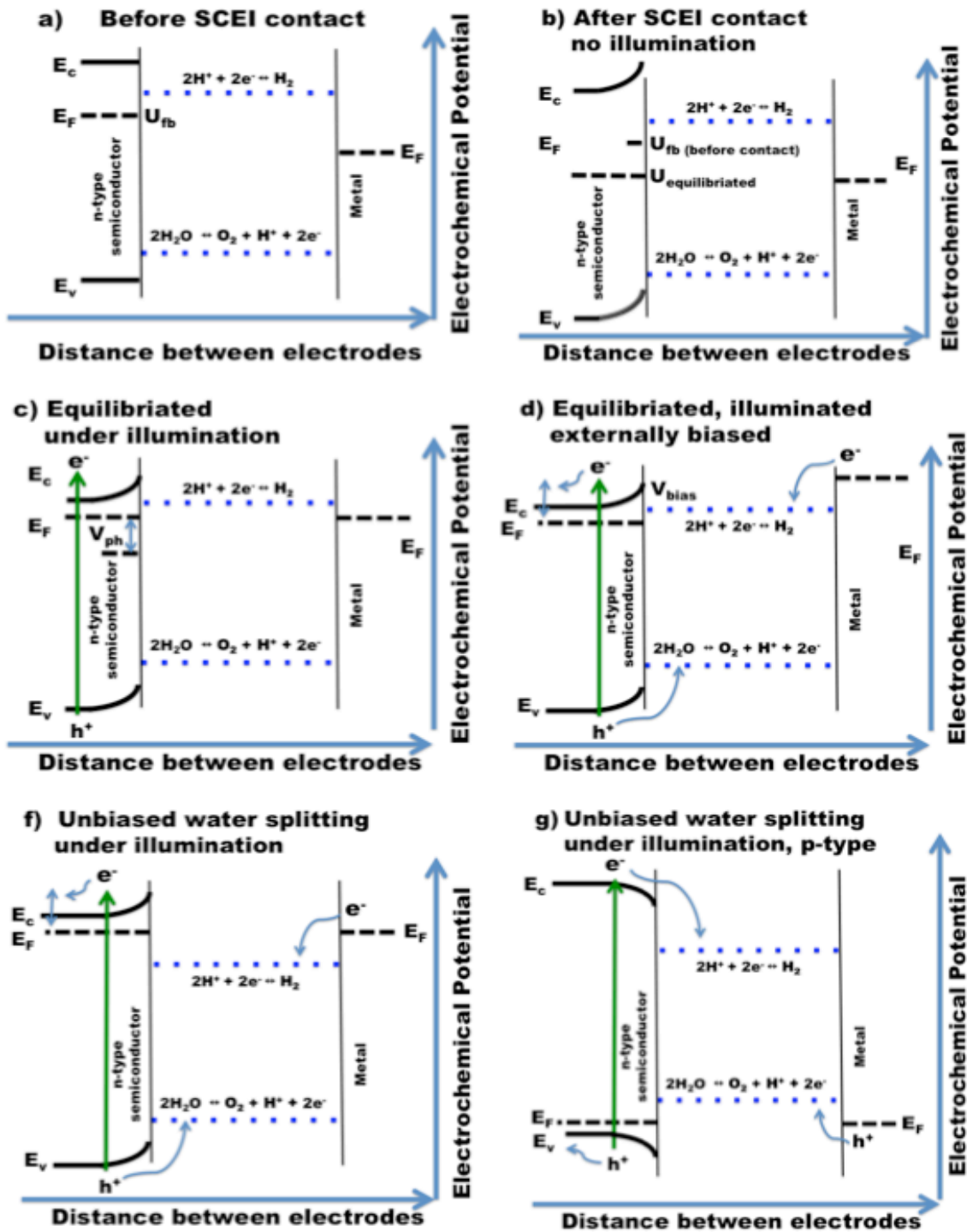


Figure 2.3: voltage vs. distance plots for various SC and metal counter electrode band energy level positions with respect to the OER and HER redox levels. Figures 2.3a-d show band configuration of a non-working n-type semiconductor (a) before contact, (b) after equilibration with the electrolyte, (c) after illumination and (d) with an external bias to make the configuration functional for PEC water splitting.

### PEC Material Requirements:

The most basic PEC water splitting cell configuration is the Schottky type water splitting cell that utilizes a single semiconductor. This type of PEC cell has been extensively studied and as such, the materials requirements for efficient water splitting utilizing this type of cell are well known<sup>27</sup>. Extensive research for the requirements for a tandem cell configuration have also been considered, the only place these cells majorly differ is the band gap(s) required for optimal efficiency. For further considerations in this chapter beyond the band gap, only the single electrode configuration will be studied.

First and foremost, the single semiconductor needs to have a minimum band gap 1.7 eV and a maximum band gap of 2.2 eV. This is to ensure the most efficient absorption and conversion of the visible light range where the highest density of solar energy is located. It also provides more bias than the 1.23 V needed for water splitting in order to overcome different losses inherent to the PEC water splitting process. A tandem device requires two semiconductors, one with approximately 1.0 eV band gap and the other with approximately a 1.7 eV band gap. Other major requirements of the semiconductor are that it have appreciable charge carrier conductivity, band edge placement and reaction kinetics. To perform water splitting unless the semiconductor already has favorable conduction band potential higher than the HER, valence band potential lower than the OER and appropriate flat band potential with respect to the half-reaction being driven by the SC. The OER and HER must also be the favorable reactions at the SC surface and not another reaction such as a corrosion reaction. Furthermore,



doping for conductivity can only improve a material to an extent and so the majority and minority carrier conductivities of the semiconductors also play a role in efficient water splitting. Also of major concern for a semiconductor capable of performing efficient water splitting is that it should be stable in aqueous solution. The current benchmark for this stability is that it be stable for more than 1000 hours but much higher stabilities will be necessary<sup>11</sup>. Finally, and probably most importantly, the material needs to be abundant enough to make production affordable on a mass-scale.

### Efficiency

The ultimate parameter to be considered of an operating PEC cell is the efficiency at which it operates. In order to measure the exact solar-to-hydrogen efficiency, a complicated PEC setup requiring a gas capturing and measurement set-up in order to measure every mole of hydrogen produced compared to each photon of incoming light is needed. The next best alternative is to use a potentiostat/galvanostat to measure the energy generated at the semiconductor surface in comparison to all of the incoming light as shown in equation 2.6<sup>28</sup>.

$$\varepsilon = \frac{1.229I_P}{P_t} \quad (2.6)$$

Where  $\varepsilon$  is the solar energy efficiency,  $I_p$  is the photocurrent measured at the semiconductor under illumination and  $P_t$  is the power of the total incoming light. One major assumption of this efficiency is that the Faradaic yield is 100% meaning that all of the generated photocurrent is utilized for the water splitting reaction. If current is being

generated by other reactions at the semiconductor surface such as corrosion reactions, this efficiency is not a true measure of water splitting efficiency. The only way to rule this out is the complicated setup mentioned prior to this. The other major assumption of this efficiency is that no external bias is used. In order to account for external bias, modification can be done to equation 2.6 as shown in equation 2.7.

$$\varepsilon = \frac{(1.229 - V_{bias})I_P}{P_t} \quad (2.7)$$

Where  $V_{bias}$  is the external voltage applied between the semiconductor and counter electrode.

## 2.2 State-of-the-art semiconductor review for photoelectrochemical water splitting

Due to the many semiconductor properties required to be considered for PEC water splitting, one has to choose one of two routes when researching a semiconductor photoabsorber for PEC water splitting. One option is to research a previously un-researched semiconductor system and attempt to discover a semiconductor with all of the requirements to efficiently split water. The other approach would be to take one of the many researched semiconductors and modify them in some way in order to make them suitable for water splitting such as adding protective coatings to materials that aren't stable or doping to improve conductivity. Many semiconductor material types have been explored for use in solar hydrogen production but none have fulfilled all of the requirements. The material classes that have already been investigated fall into the

following categories: metal oxides, silicon based, metal chalcogenides and III-V materials. The advantages and disadvantages for each of the classes of materials are discussed below.

Metal Oxides: Metal oxides have been heavily researched for photoelectrochemical water splitting. This is largely because  $\text{TiO}_2$  was the first material to successfully demonstrate photoelectrochemical water splitting as shown by Fujishima and Honda in 1972<sup>20</sup>.  $\text{TiO}_2$  as well as other 3 eV and wider band gap metal oxide semiconductors such as  $\text{ZrO}_2$ ,  $\text{KTaO}_3$  and  $\text{SrTiO}_3$  have conduction and valence bands that straddle both the HER and OER but their high band gap only allows them to absorb enough of the solar spectrum to have 2% maximum theoretical efficiencies<sup>4</sup>. Cuprous oxide ( $\text{Cu}_2\text{O}$ ) has a favorable 2.0 eV direct band gap and bands favorable for use as a photocathode. Gratzel et al have developed a cuprous oxide device that has the best performance of all current metal oxide semiconductors but shows photocorrosion in aqueous solution<sup>29</sup>. Hematite has a 2.1 eV band gap but suffers from an indirect band gap, poor photovoltage, low minority carrier diffusion length and its conduction band falls short of the HER<sup>30-34</sup>. Major efforts have been taken to overcome these drawbacks such as doping with silicon and using nanomorphologies to reduce the amount minority carriers would have to travel to get to the surface of the material<sup>35,36</sup>. Tungsten trioxide ( $\text{WO}_3$ ) is a 2.6 eV n-type semiconductor that has been used as a photoanode for water splitting<sup>37-39</sup>. It has decent photo absorption characteristics, good electron transport and high stability in acidic aqueous solutions. The band gap however is too wide to absorb enough of the solar spectrum and limits the materials theoretical STH efficiency to below 3%. It also has a

conduction band that falls short of the HER and as such would need some form of external bias to split water. Copper tungstate ( $\text{CuWO}_4$ ) has a band gap of 2.2 eV and its band edges straddle the HER and OER<sup>40,41</sup>.  $\text{CuWO}_4$  unfortunately has poor transport properties that need to be improved before it becomes viable for PEC watersplitting. Bismuth vanadate ( $\text{BiVO}_4$ ) has a band gap of 2.4 eV with band edges sufficient to run the OER but falls just short of the HER<sup>42-44</sup>. The 2.4 eV band gap also limits its efficiency as much of the visible light region is not absorbed. As such, van de Krol et al grew  $\text{BiVO}_4$  utilizing a doping gradient with W and combined it in tandem with a Si solar cell to achieve STH efficiencies as high as 5.2%<sup>45,46</sup>.

Silicon and Silicon Carbide: Due to its heavy use in integrated circuits and solar industries, silicon and silicon carbide have been studied heavily for use in PEC watersplitting. p-type silicon has a band gap of 1.1 eV and well placed band alignment for use as photocathode in a two electrode device. It also has the advantage of having an established market where low defect materials are easily obtained, interface junctions for monolithic devices are easily incorporated and mass production techniques are well established. It unfortunately suffers from having an indirect band gap and corrodes over long term use though many efforts have been made to address these issues such as covalent attachment of methyl groups and ultra-thin layers of nickel.<sup>44,47-49</sup> To date, the most efficient use of Si for PEC water splitting has been the device developed by Domen et al which incorporates three or four spherical Si p-n junction solar cells in tandem as the photoabsorber and encapsulated in epoxy for protection. These Si photovoltaic cells

integrated between NiO and NiFe as the anode and cathode. STH efficiencies of 7.4% and 6.4% were obtained for the 3 and 4 solar cell devices respectively.

Silicon carbide has a band gap of 3.0 eV which, as addressed above, is far too large to efficiently absorb enough light but it straddles the HER and OER potentials. By synthesizing a hydrogenated amorphous silicon carbide and alternating the carbon gas source, the band gap can be readily tuned between 1.9 eV and 2.3 eV, both n and p-type doped and easily integrated into amorphous Si tandem cells<sup>50,51</sup>. The state of the art a-Si/a-SiC tandem cell configuration using an RuO<sub>2</sub> counter electrode as OER catalyst reaches a 6.1% efficiency and had an operation lifetime of over 500 hours<sup>52,53</sup>. The major challenges still involved are the development of a surface barrier to address corrosion, improvement of current matching at each junction, improvement of surface energetics and better performing PV layers as the a-Si is currently limiting the cell to a 7.6% STH efficiency.

Metal Chalcogenides: Metal chalcogenides markets have also seen much development in the thin film PV market and as such have also been looked at for water splitting. Tungsten sulfide (WS<sub>2</sub>) has a 1.4eV band gap and band edges straddle the HER<sup>54</sup>. Molybdenum sulfide (MoS<sub>2</sub>) has a 1.2 eV band gap and is stable in acidic condition making it promising as a photocathode but its conduction band falls short of the HER which would make it require an external bias to split water<sup>55,56</sup>. MoS<sub>2</sub> also shows a metallic behavior inhibiting its use as a photoabsorber. Both Both WS<sub>2</sub> and MoS<sub>2</sub> have band gaps too narrow for unassisted water splitting. As such, efforts have been made to study CuInGaS and CuGaSe<sub>2</sub> by several groups due to their tunable direct band gap

nature by modifying the In:Ga ratio, but have misaligned band edges for water splitting and poor aqueous stability.<sup>57,58,59,60</sup>

III-V Semiconductors: III-V materials are, to date, the best photoabsorber materials known. III-V materials currently hold the records in both photovoltaic cells and photoelectrochemical water splitting. Of the researched III-V materials for water splitting, it can be seen that III-V materials have performed closer to their thermodynamic potentials than any other class of semiconductor.

Indium phosphide (InP) has a direct 1.35 eV band gap and band edges appropriate for use as a photocathode to drive the HER. 11-13% solar to chemical conversion efficiencies calculated under ideal operation conditions were reported by Heller et al by decorating InP with Ru catalyst islands, however, actual STH efficiencies of this magnitude have not been observed.<sup>61</sup>

Gallium phosphide (GaP) is a well-known semiconductor with an indirect band gap of 2.3 eV, band edge alignment desirable both for photoelectrochemical water splitting as well as CO<sub>2</sub> reduction,<sup>16,17,62</sup> and appears to be stable as a photocathode for PEC water splitting under reducing conditions<sup>63,64</sup> GaP is also desirable due to its low lattice mismatch with Silicon of .37%, which allows for the more economical growth of GaP epi-layers using silicon substrates as has been demonstrated by several groups.<sup>65-67</sup> It unfortunately has an indirect band gap which causes a relatively large absorption depth in comparison to the relatively low minority carrier diffusion length<sup>68</sup> and poor surface kinetics.<sup>63</sup>

Gallium antimonide (GaSb) is also well-known with a direct band gap of 0.725 eV<sup>69</sup>. It has been interesting largely as a substrate due to its lattice parameter that

matches many other ternary and quaternary III-V compounds. It has not however been tested for use in PEC water splitting. This has largely to do with its low band gap, only allowing it to efficiently take advantage of a small part of the visible light spectrum.

Much interest has recently been generated in ternary III-V alloys due to their ability to exhibit tunable band gap across a range of energies while still having strong electrical capabilities. In fact, the current state of the art water splitting device is GaInP<sub>2</sub>, a III-V ternary alloy, with a 12.4% water splitting efficiency.<sup>70</sup> GaInP<sub>2</sub> has a band gap of 1.83 eV but its valence band edge potential is higher than the oxygen evolution potential. To overcome this, Turner et al grew the semiconductor as a monolithic tandem cell with built in photovoltaic GaAs p-n junction. The current challenges with this material are the costs of the GaAs growth substrates and photocorrosion of the material. Furthermore, this GaInP<sub>2</sub>/GaAs multijunction strategy was used as the photoabsorber material for the ultimate project device generated by JCAP in 2015, which was able to generate 10% efficiency for 80+ hours<sup>12</sup>.

Gallium nitride has a very wide direct band gap of 3.45 eV, band edge placement capable of splitting water and high stability as a photoanode for direct water splitting. Unfortunately, the wide band gap limits its efficiency to below 2% similarly to SiC making it very inefficient for water splitting. Efforts have been undertaken however to alloy this material into ternary and quaternary structures in order to tune the band gap including the following: InGaN<sup>71</sup>, ZnO:GaN<sup>72</sup>, GaSbN<sup>19</sup>, GaAsPN<sup>73</sup>, and GaPN<sup>73</sup>.

Another ternary III-V alloy, GaPSb has previously been researched by several groups. Initially thought impossible to grow in epitaxial layers due to the 530°C miscibility gap between GaP and GaSb across the entire range of compositions, GaP<sub>(1-</sub>

$x$ )Sb $_x$  epilayers were still eventually synthesized by Stringfellow et al using organometallic vapor phase epitaxy.<sup>74</sup> The layers were grown in several discrete compositions with correlated photoluminescence responses but were localized at 4 approximate compositions. The composition and PL data obtained are as follows  $x_{Sb1}=.14/PL_{Sb1}=1.6eV$ ,  $x_{Sb2}=.3/PL_{Sb2}=1.4eV$ ,  $x_{Sb3}=.37/PL_{Sb3}=1.3eV$  and  $x_{Sb4}=.93/PL_{Sb4}=.794eV$ . GaSbP has further been researched by other groups for its ability to form a Schottky diode with InP,<sup>75</sup> as a vertical cavity emitting surface laser,<sup>76</sup> and the Stranski Krastanov mode growth on GaP.<sup>77</sup> Electron transport in a GaPSb films have also been studied.<sup>78</sup> GaSbP has not, on the other hand, been explored for use as a photoelectrochemical water splitting electrode and the indirect to direct transition has not been observed.

#### Summary of advantages and disadvantages for each material class

Metal Oxides have great aqueous stability but generally have band gaps that are too wide, poor light absorption and poor charge carrier transport. The exception to this is cuprous oxide, however it shows poor stability. Silicon benefits from having good band edge placement as a photocathode and from being an already established technology for high-quality crystal growth. Silicon, however, suffers from an indirect band gap and corrosion in aqueous solution. Amorphous hydrogenated silicon carbide also benefits from the established silicon technologies and an ability to tune the band gap of the material. Corrosion, poor energy matching at junctions, surface energetics and PV layers for tandem cells need to be improved for a-SiC to be viable. Metal chalcogenides tend to have low band gap, poor band alignment and poor aqueous stability. III-V materials have



tunable band gaps within the visible light absorbing region, superb absorption characteristics and high charge carrier mobilities. The biggest drawbacks of using III-V's are that most have stability issues in aqueous solutions, expensive and toxic precursors and expensive substrates are required. Regardless of this, III-V materials have performed closer to their theoretical efficiencies than any other class of materials.

### 2.3 III-V nanowires vs. epitaxial layers

There are two general approaches towards the state of the art water splitting devices being researched currently. Both have shown their strengths and limitations. One of these approaches involves growing semiconductors in high quality planar layers utilizing techniques such as MOCVD. These techniques provide precise control over semiconductor quality and layer thickness but are expensive. The other approach is to grow semiconductors with nanostructured morphologies. Nanostructuring provides greater surface areas than planar films that allow for increased light absorption and surface reaction area. These types of morphologies are more difficult to control however and proper electrical contact between the nano-structures is not always feasible.

There are multiple ways to nanostructure a semiconductor. Nanowires are one of the more popular routes to nanostructuring as it provides desirable attributes to assist in PEC water splitting. One of these advantages is due to the high surface to volume ratio provided by nanowires. With proper orientation, this provides increased surface area for light absorption in the same electrode area compared to planar films. This also provides increased area for reaction to take place. Nanowires can also be grown single crystalline, providing fewer grain boundaries<sup>33,35,79-85</sup> where recombination can occur, than a

polycrystalline film, assuming proper electric contact can be made to each nanowire through proper device structuring<sup>86-88</sup>. High aspect ratio nanostructured morphologies like nanowires and nanorods also provide short diffusion distances to the surface due to minority carriers only needing to diffuse radially to the semiconductor surface. This helps to mitigate recombination due to minority carriers having to traverse distances longer than their respective diffusion lengths as shown in materials such as hematite<sup>89</sup>. Nanostructuring films for PEC has demonstrated better PEC performance than using amorphous and multicrystalline thin films in several systems such as TiO<sub>2</sub>, ZnO and Hematite<sup>90-93</sup>.

On the other hand, all of the best performing solar devices to date have come from high quality planar devices, photovoltaics and PEC included. This has to do with the ability to finely control the layer size and quality of crystal grown using metal organic chemical vapor depositions (MOCVD), molecular beam epitaxy (MBE) and atomic layer deposition (ALD) techniques among others. All photovoltaic records are held by materials containing single crystal layers<sup>94</sup>. The PEC water splitting record also uses high quality single crystalline materials<sup>5</sup>. Quite plainly, high-quality, single crystal layers take the most advantage of semiconductor electrical properties while limiting unwanted effects like recombination.

Current state of the art research on water splitting focused on achieving high efficiencies by growing photovoltaic grade single crystal materials. Faster progress could potentially be made with single crystal nanowire arrays but high surface to volume ratio could introduce high density of surface states within the band gap that could hinder the photo-electrochemical water splitting performance.

## 2.4 Halide vapor phase epitaxial growth of III-V materials

HVPE is a relatively unexplored technique but with tremendous promise. HVPE provides much higher epitaxial growth rates than MOCVD and MBE (100+ microns per hour) and doesn't require expensive precursors necessary for MOCVD making it a much cheaper alternative as well. Due to lower required operating temperatures, HVPE should also require a much lower energy input than doing high-pressure solution growth of semiconductors. The process however produces byproducts that are either toxic or corrosive and thus requires extreme care in designing the reactor. For example, HVPE reactions can require gas phase species from group V of the periodic table such as ammonia, phosphine, and arsine.

Nitrides have been the most explored class of III-Vs grown by HVPE<sup>13,95-110</sup>. InN, GaN, and AlN were all grown in single crystalline layers by Koukitu et al on several substrates including sapphire ( $\text{Al}_2\text{O}_3$ ), silicon carbide (SiC) and gallium arsenide (GaAs)<sup>111</sup>. Gallium nitride was grown utilizing a five-zone tube furnace with  $\text{NH}_3$ ,  $\text{N}_2$  and  $\text{HCl}/\text{N}_2$  gas inlets. The  $\text{HCl}/\text{N}_2$  stream was passed over a gallium boat held at temperatures between 500-1000 °C to react near the initial zones of the heater and yield  $\text{GaCl}$ ,  $\text{GaCl}_2$  and  $\text{GaCl}_3$  in the gas phase. The ammonia and  $\text{GaCl}_x$  gases then react where the substrate is held in the final zone of the heater at 500-900 °C. Across the reviewed publications, this is the typical reactor scheme used for HVPE with variations typically being changes in orientation to vertical setups or utilizing different heating mechanisms such as induction heating. Koukitu et al also grew InN and AlN in a similar manner, replacing In or Al in the Ga boat. This reactor scheme achieved epitaxy rates of over 120

microns per hour in the case of AlN, 60 microns per hour in GaN and .5 microns per hour in InN. Furthermore, many substrate removal techniques to yield free standing wafers were explored including laser lift-off, self-separation, mechanical polishing, reactive-ion etching, chemical etching and spontaneous self-separation. The Koukitu group also grew GaAs (1 monolayer/ 32 second cycle) and InGaAs by atomic layer epitaxy techniques ( $3\text{\AA}/10\text{s}$ ) utilizing HVPE<sup>112,113</sup>.

Gallium phosphide (GaP) was grown by Sudlow et al using a similar reactor scheme except instead of directly utilizing HCl to transport the gallium hydrogen is bubbled through a  $\text{PCl}_3$  source, which reacts and yields both HCl and  $\text{P}_2$  in the gas phase<sup>114</sup>. The HCl then reacts with a pool of Ga and then the  $\text{P}_2$  and  $\text{GaCl}_x$  react at the deposition zone to form epitaxial GaP at growth rates of 80 microns per hour. Yang et al, were able to grow InGaN NWs across the full ternary compositional range of  $\text{In}_x\text{Ga}_{1-x}$  making HVPE also promising for exploring different compositions of ternary III-V alloys, furthermore these samples were characterized for PEC water splitting performance but incapable of splitting water<sup>13</sup>. Epitaxial InP was grown by Park et al reaching growth rates of 20 microns per hour<sup>115</sup>. At the time of this writing, GaSb has not been synthesized by HVPE techniques.

As seen above, HVPE has been accomplished for many III-V alloy systems in several reactor schemes. Utilizing HVPE, growth rates near or above 100 microns per hour have been observed for several systems and ternary alloys have been grown throughout their ternary composition range. Furthermore, the typical precursors used are available on a large scale due to wide use in industry making the process economical as well. The high growth rates and economical precursor costs provided by HVPE could

lend the process to scalable synthesis schemes for advanced III-V manufacturing. Many challenges must be overcome to utilize HVPE however as these very same precursors are toxic, corrosive and pyrophoric, however, making sophisticated safety systems and redundancies mandatory when utilizing this technique on any scale. To date GaSbP alloys have not been synthesized using HVPE. On the other hand, GaSbP has been grown via other epitaxy techniques and Sb-halide precursors such as  $\text{SbCl}_3$  are readily available making HVPE a well-suited candidate for enabling GaSbP epitaxy.

## CHAPTER 3

### EXPERIMENTAL METHODS

This chapter presents the methods undertaken for computation and to complete these studies. The various approximations and parameters utilized to perform these DFT+U calculations on the GaSbP system are explained. This is followed by the procedures for growing GaSbP nanowires in reactive vapor transport experiments done on GaSbP. After this, the design, assembly and operation of the HVPE reactor will be discussed. Next, the structural and optical characterization techniques utilized to study the grown samples are discussed. Finally, the photoelectrochemical techniques undertaken will be discussed.

#### 3.1 Computational Techniques: Density Functional Theory

DFT+U calculations were utilized in collaboration with Professor Madhu Menon at University of Kentucky to investigate the structure and band edge properties of GaSbP. DFT+U has shown tremendous value for predicting band gap in recent reports<sup>1,19,116</sup>. However, fitting existing data can yield negative U values<sup>117-122</sup>. DFT+U calculations approximated at the Perdew-Burke-Ernzerhof approximation level of the generalized gradient approximation.<sup>123</sup> These calculations were implemented using the Vienna Ab-initio simulation package<sup>124-126</sup>. Core electrons are described by the projected augmented

wave potential<sup>125,126</sup>. To more accurately address band gap estimation, the Hubbard correction parameter,  $U$ , was utilized<sup>116</sup> first implemented by Dudarev<sup>22</sup>. Convergence testing led to a 2x2x1 centered pack being utilized for k-vector sampling. These k-values were used in density of states calculations. A kinetic energy limit of 520 eV was deemed acceptable for complete convergence of total system energies within 1 meV and in order to accelerate convergence Gaussian smearing of .05 eV was chosen. Optimal atomic positions were converged upon when each atom had less than 5meV/A force on it.

Structurally optimized supercells were determined before moving onto density of states calculations.  $U$  values for the GGA+ $U$  calculations were as follows: and  $U_p(\text{Sb}) = -4.2$  eV,  $U_d(\text{Ga}) = 6.5$  eV and  $U_p(\text{P}) = -14.5$  eV. Other values for  $U$  were set to zero. Both experimental and theoretical data were utilized to fit band gap and density of states calculations when possible. Convergence for band gap calculations was set to  $10^{-6}$  eV.

### 3.2 Reactive Vapor Transport Method for Growing $\text{GaSb}_x\text{P}_{1-x}$ Nanowires

The first sets of synthesis experiments were performed using a reactive vapor transport. Gallium antimonide and gallium phosphide powders were ball milled together into a powder and placed in a boronitride (BN) crucible. The BN cup with a quartz substrate on top was then placed on a heater inside of a chemical vapor depositon (CVD) reactor that was pumped down to 3.5 millitorr and purged several times with nitrogen. The heater was then raised to temperatures between 650°C and 900°C and the powders were able to be evaporated together and react at the lower temperature quartz substrate at the top of the BN crucible.

The second set of synthesis experiments were performed using reactive transport employing an ASTeX AX 5310 microwave plasma reactor. Intrinsic (111) oriented silicon substrates were first prepared using standard RCA SC1, HF treatment and SC 2 cleaning procedures to ensure the removal of trace metals, organic compounds and native oxides at the silicon surface. Ga and Sb metals were placed on opposite sides of a graphite susceptor with clean growth substrates placed in between. Iron and quartz were also used as substrates in subsequent experimentation. Hydrogen was bubbled through di-tert-butyl-phosphine (DTBP) precursor held at 720 torr at a rate of 20 sccm. Hydrogen was used at a flow rate of 200 sccm. The reactor was cycled to a  $10^{-2}$  torr vacuum three times then filled with hydrogen stream to an atmosphere of 100 torr. The plasma was then ignited and adjusted to plasma power between 800 and 1000W. Upon reaching the target plasma power, the DTBP stream was introduced and the plasma reaction was allowed to carry out for two hours.

### 3.3 Halide Vapor Phase Epitaxy Reactor

Previous efforts have used MOCVD and MBE to grow  $\text{GaSb}_x\text{P}_{(1-x)}$  films<sup>74-76</sup>. MOCVD requires precursors that are very expensive such as trimethyl-gallium, trimethyl-antimony and phosphine. Molecular beam epitaxy requires extremely low pressures, extremely low growth rates and high operation costs (heating and vacuum). High pressure solution growth offers high growth rates and high quality for growing binary III-V semiconductors, it requires high operation costs however (high pressure and heating) and is incapable of growing many ternary alloys due to miscibility gaps under equilibrium conditions.



HVPE is another CVD process capable of growing III-V epilayers. Relative to the aforementioned techniques, there are very few scientific reports available on HVPE synthesis of III-V materials. In a review of III-V materials grown by HVPE less than 20 scientific reports were found among all of the III-V materials. The primary reason behind this is due to the dangerous nature of the precursors involved for reaction. A typical HVPE reactor will utilize HCl gas to generate group III gas phase precursors such as GaCl. Furthermore, to provide group V column gas phase precursors gases such as ammonia or phosphine are required. These gases require the utmost in regard to safety and this drives many researchers away from wanting to use these reaction schemes.

HVPE offers many advantages over the aforementioned growth techniques as well. The precursors required for doing reactions are industry standards and are widely and affordably available, especially in comparison to MOCVD precursors. HVPE also provides much higher growth rates with as high as 100+  $\mu\text{m/hr}$  in comparison to typical growth rates of 5  $\mu\text{m/hr}$  for MOCVD and 1  $\mu\text{m/hr}$  for MBE. It is also a non-equilibrium growth technique potentially enabling the growth of ternary and quaternary alloys. Here, a HVPE reactor is designed and built to be utilized for the growth of GaSbP epitaxial layers. The reactor was built with the utmost safety in mind.

The initial reactor scheme proposed can be seen in Figure 3.1. In this scheme, HCl gas and  $\text{PH}_4$  gas would be flowed over Sb and Ga boats held at different temperatures where the HCl would react with the Sb and Ga to form SbCl and GaCl gas species. The GaCl, SbCl and  $\text{PH}_3$  would react at the 3<sup>rd</sup> deposition temperature zone to form GaSbP. A thorough discussion of reaction chemistry is discussed in Chapter 5.

This proposed scheme was the initial scheme pursued for the HVPE reactor. However, the use of ultra-pure HCl gas and highly toxic phosphine makes the above scheme a difficult proposition.

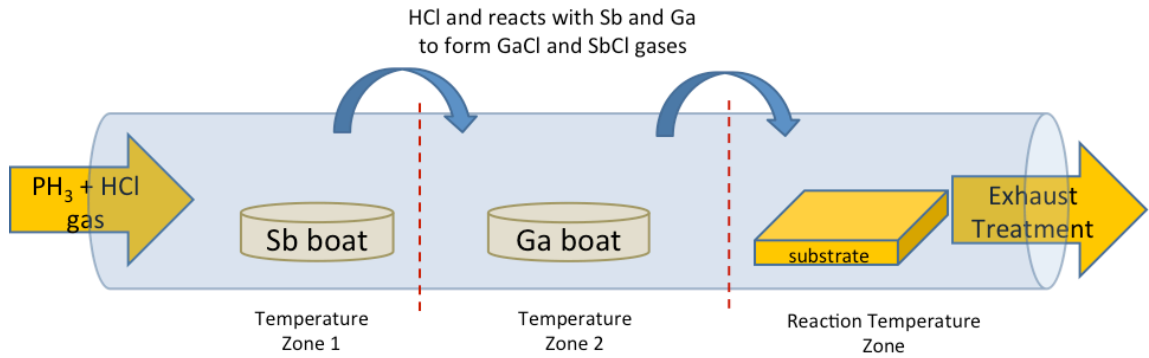


Figure 3.1 An illustration of a reaction scheme attempted for HVPE.

Another possibility is to use  $\text{PCl}_3$  for phosphorous source. When placed in a bubbler,  $\text{H}_2$  gas can be flowed through the bubbler in order to not only provide gas phase phosphorus, but reacts with the  $\text{PCl}_3$  vapor to give both HCl gas and  $\text{P}_2$ . This is much easier to maintain than both HCl and  $\text{PH}_3$  gases and is much easier to obtain. Furthermore,  $\text{PCl}_3$  is an abundant industrial material making it readily available and affordable.

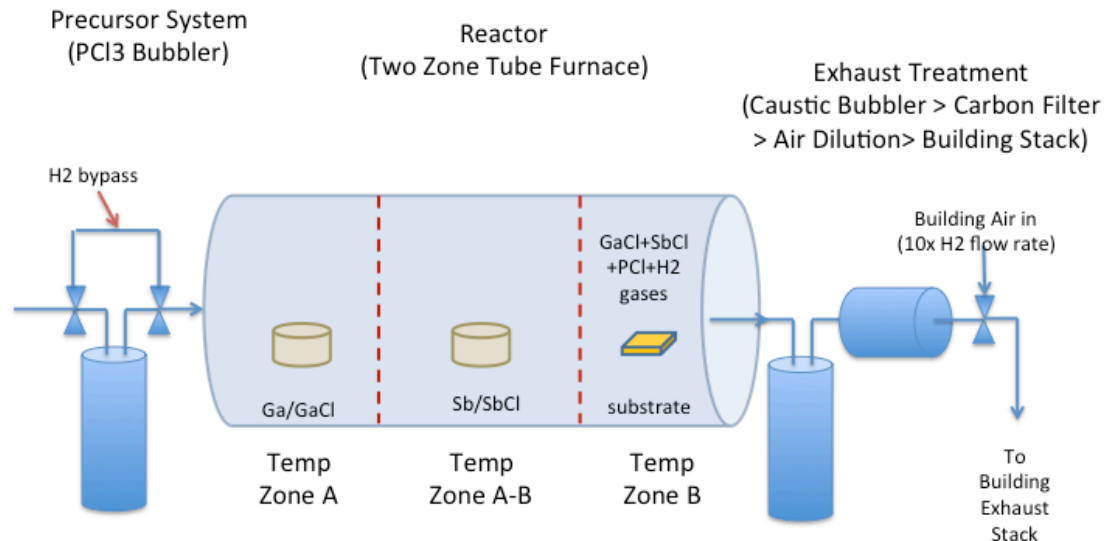


Figure 3.2 – Reaction scheme including  $\text{PCl}_3$  chemistry

The reaction scheme involves flowing  $H_2$  through the  $PCl_3$  bubbler to produce  $HCl$  and  $P_2$  gases. The  $HCl$  gas reacts with Ga and Sb held at different temperatures to form  $GaCl$  and  $SbCl$  gases. The  $GaCl$ ,  $SbCl$  and  $P_2$  gases react at the deposition zone held at a third temperature. The exhaust gases are then pumped through a  $KOH$  bubbler to neutralize both acidic gases and phosphorus containing gases. This reactor scheme was approved with the condition that a third heating source be on top of the in-house provided two-zone furnace and appropriate engineering measures be taken to make the process safe.

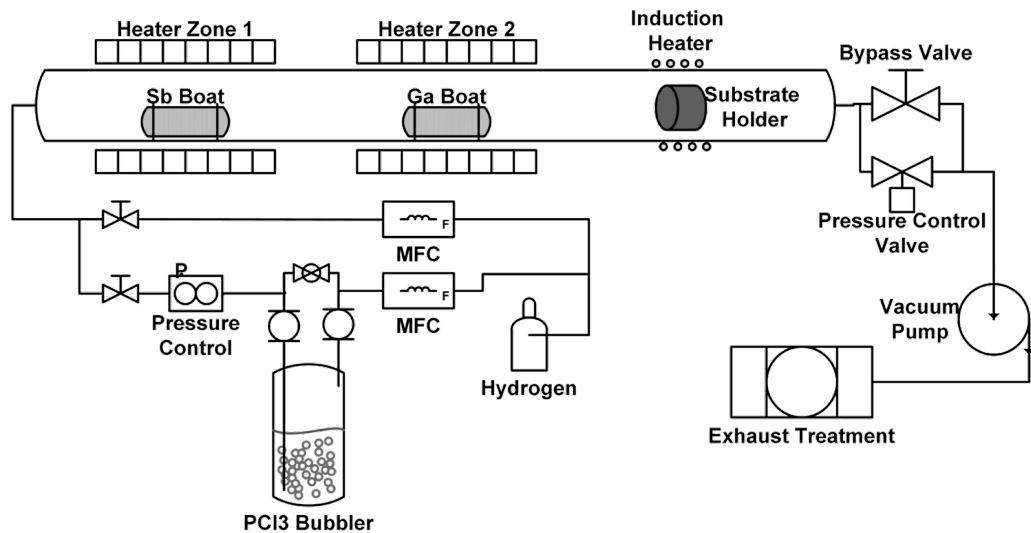


Figure 3.3 Process flow diagram of custom-designed HVPE reactor

### 3.3.1 Reactor Assembly

A process flow diagram of the built reactor is shown in Figure 3.3. The hydrogen line is split into two lines each is controlled by a MKS mass flow controller. The first line provides only  $H_2$  to the reactor at rates between 1-1000 sccm. The second line provides  $H_2$  to the  $PCl_3$  bubbler at rates between 0.1 and 100 sccm. Having this  $H_2$  bypass allows

facile control over both the partial pressure of  $\text{PCl}_3$  and  $\text{H}_2/\text{HCl}$  ratio provided to the reactor. Just after the bubbler, an MKS type 640 pressure controller valve holds the bubbler at a chosen operating pressure. The amount of  $\text{PCl}_3$  available for carrier gas to transport out of the bubbler is controlled by the pressure on the bubbler. The higher the pressure maintained on the bubbler, the lower the ratio of  $\text{PCl}_3$  available to be transported. With these controls, the flow rate of  $\text{PCl}_3$  transported to the reactor can be estimated. Pyrometer readings of the bubbler during operation show that it is approximately  $35^\circ\text{C} \pm 3^\circ\text{C}$ . At the temperature, thermochemical data from JANAF tables were utilized to determine that  $\text{PCl}_3$  at  $35^\circ\text{C}$  has a vapor pressure of 150 torr. Utilizing this partial pressure, the bubbler pressure and the flow rate of the carrier gas, the molar flow rate of  $\text{PCl}_3$  provided to the reactor can be estimated as shown in equation 3.1.

$$m_{\dot{\text{PCl}}_3} = p_{\text{PCl}_3} * P_{\text{bubbler}} * \dot{V}_{\text{carrier}} \quad (3.1)$$

Where  $m_{\dot{\text{PCl}}_3}$  is the molar flow rate of  $\text{PCl}_3$  transported from the bubbler,  $p_{\text{PCl}_3}$  is the partial pressure of  $\text{PCl}_3$  bubbler,  $P_{\text{bubbler}}$  is the pressure the bubbler is held at and  $\dot{V}_{\text{carrier}}$  is the volumetric flow rate of gas being passed through the bubbler.

Manual valves are present for both the  $\text{H}_2$  and  $\text{PCl}_3$  lines just before entering the reactor chamber. These valves proved a positive shut-off for the precursor gases and add another level of safety to the process. The reactor chamber consists of a quartz tube with compression vacuum fittings to allow its use as a CVD reactor. The quartz tube is placed inside of an MTI OTF-1200X-II tube furnace.

Just after this two-zone tube furnace, an induction heater provides the third heating zone. An induction heater adds functionality beyond the capabilities of the tube furnace. The induction heater can heat up at far greater rates than the tube furnace and can reach temperatures of 2000°C with ease while the tube furnace struggles to get above 1000°C. The ability to attain temperatures as high as 2000°C enables any required temperature for III-V growth to be achieved. To pull the lowest vacuum, a large manual

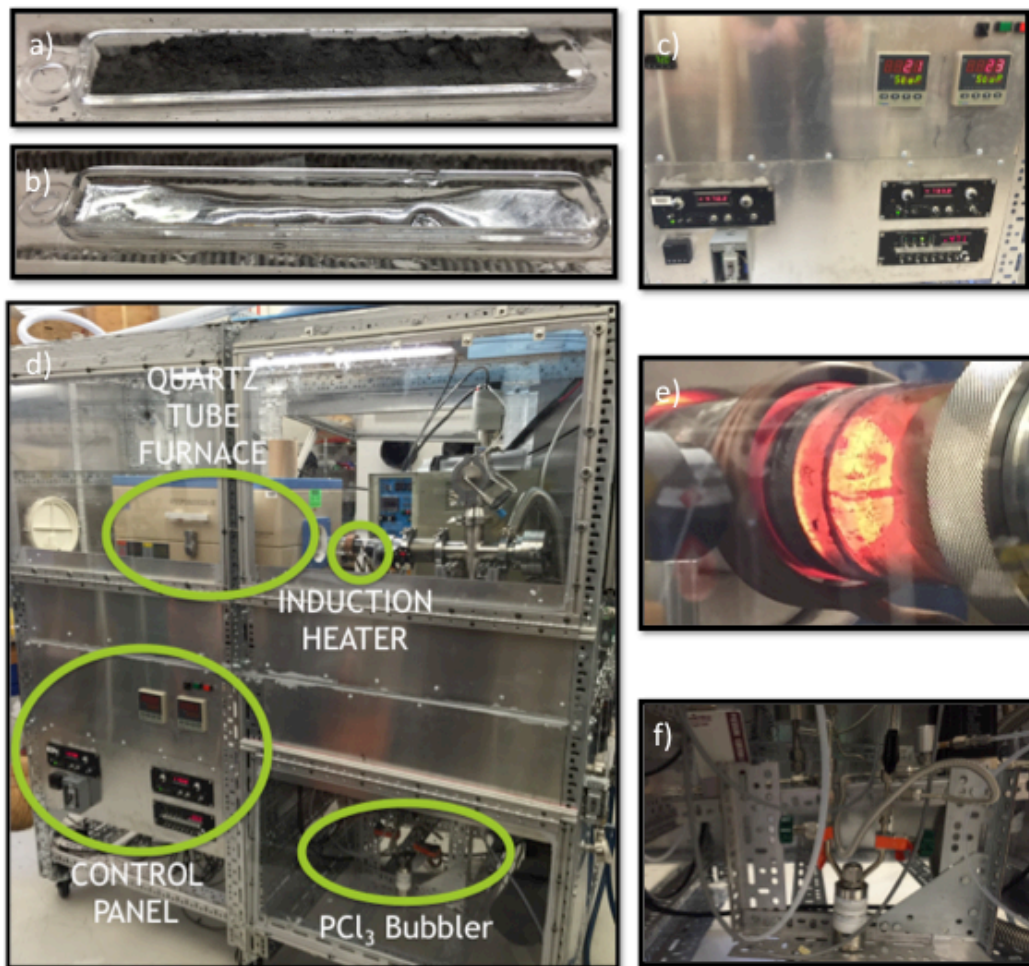


Figure 3.4 – Photographs of the assembled reactor. The precursor boats for Ga and Sb are shown in (a) and (b). Process readouts and controllers are shown in (c). An overview of the reactor is shown in (d). The induction heater during operation is shown in (e). The PCl<sub>3</sub> bubbler is shown in (f).

control valve was used, however, during operation a pressure control valve with a very small orifice was used. The gases are then pumped out of the vacuum pump where they will be treated by a KOH bubbler (further description below) then subsequently diluted with air by at least 10 times.

Photographs of the assembled reactor are shown in Figure 3.4. In Figures 3.4a and 3.4b, the quartz boats holding Sb and Ga metals are shown. In Figure 3.4c, process controls and readouts for the reactor are shown. In Figure 3.4d, an overview of the reactor is shown from outside of the safety enclosure. In Figure 3.4e, the induction heater during operation is shown and finally in Figure 3.4f the  $\text{PCl}_3$  bubbler is shown.

### 3.3.2 Safety Considerations

Even though major safety hazards were overcome by utilizing the  $\text{PCl}_3$  chemistry over HCl and  $\text{PH}_3$ . As such, the utmost in safety is required when preparing the reactor, operating the reactor and even when the reactor is not in use. First and foremost, the reactor was built inside of a custom-built safety enclosure that is held under negative pressure during operation such that if the first line of defense (the reactor chamber) were to be breached, any reactants released would be contained within this safety enclosure. All controls were removed from reactor elements inside the enclosure, such as the temperature controls for the tube furnace, and mounted to the outside of the safety enclosure in order to enable complete operation of the reactor from outside of the safety enclosure. Furthermore, a  $\text{PH}_3$  and  $\text{H}_2$  detector is present inside the reactor enclosure. A thermocouple is also embedded in the ceiling of the safety enclosure so that temperature inside the safety enclosure can be monitored.

Consideration has also been taken for any gases that do not react during operation. Immediately following the vacuum pump is a bubbler filled with 1M KOH. GaCl, SbCl, HCl and PH<sub>3</sub> all readily react with 1M KOH such that any of these exhaust gases that pass through the bubbler should be neutralized. Furthermore, an air dilution line is added after the bubbler that dilutes any remaining undesirable gases by at least 10 times to safe levels.

### 3.3.3 Operation of Reactor

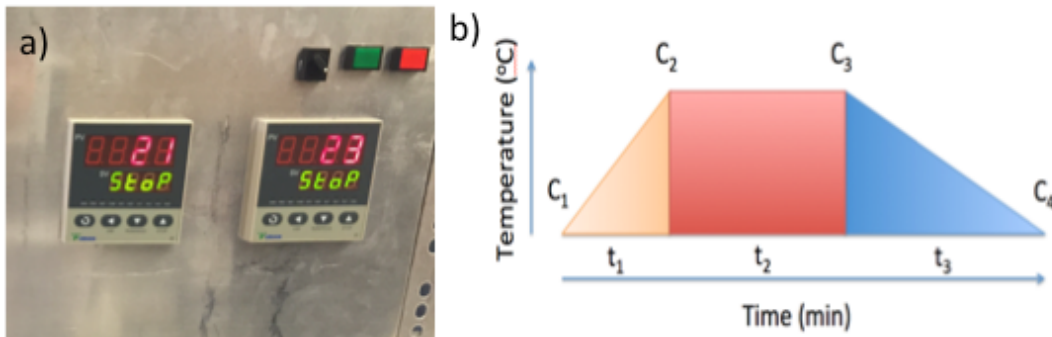


Figure 3.5 (a) temperature controllers for the tube furnace and (b) temperature programming for tube furnace ramping.

Function of the tube furnace's two temperature zones is controlled by temperature controllers for each zone mounted to the front of the safety enclosure as seen in Figure 3.5a. Control of the tube furnace works utilizing a typical temperature ramp scheme for each temperature zone as presented in Figure 5.5b. In order to do this, values for  $C_1$ ,  $t_1$ ,  $C_2$ ,  $t_2$ ,  $C_3$ ,  $t_3$  and  $C_4$  are required.  $C_1$  represents the starting temperature of the tube furnace. The amount of time it takes to ramp from the starting temperature ( $C_1$ ) to the operating temperature of the zone ( $C_2$ ) is indicated by  $t_1$  and was determined by trial and

error to be 35 minutes. This is the fastest the tube furnace can ramp to the highest required temperature, in this case the Ga zone. Upon reaching operating temperature ( $C_2$ ), the amount of time for reaction at this temperature is represented by  $t_2$  and in this case is set to 1 hour.  $C_3$  is again set to the operating temperature (same value as  $C_2$ ) required by the reactor and  $t_3$  is the amount of time required for the tube furnace to cool down (1 hour in our case) back to the starting temperature ( $C_4$ , same value as  $C_1$  in this case).

An induction heater provides the necessary operating temperature at the deposition zone. A pyrometer is used for measuring the temperature at the substrate heater through a viewport located at the end of the reactor. The induction heater and pyrometer are shown in Figure 3.6a and the ON/OFF controller and power switch are shown in Figure 3.6b. In order to keep wear and tear on the induction heater down, a duty cycle of 50% was maintained during operation resulting in an approximate 25°C temperature hysteresis at the carbon susceptor. It is recommended that future work be undertaken to reduce the size of this hysteresis to within 5°C or alternatively implement a PID control loop to allow precise temperature control of the induction heater.



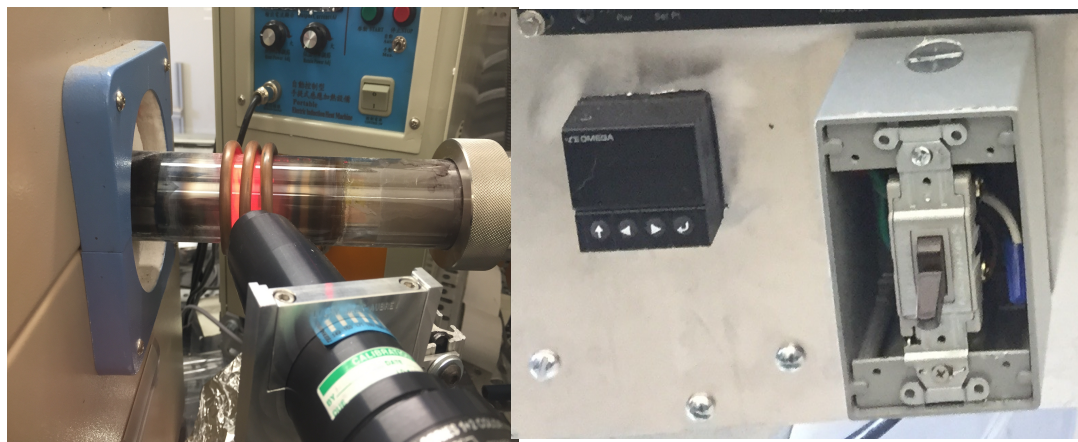


Figure 3.6 Photographs showing induction heater, pyrometer and on/off controller in the HVPE reactor.

PCl<sub>3</sub> bubbler: The PCl<sub>3</sub> bubbler shown in Figure 3.7b was purchased from STREM chemicals prefilled with PCl<sub>3</sub>. An MKS type 640 pressure control valve controls the pressure of the PCl<sub>3</sub> bubbler at all times. The 640 control valve has a built-in capacitance manometer and solenoid valve. Utilizing a set point provided by an MKS type 247 process controller, the solenoid valve opens and closes in order to maintain the set pressure. The PCl<sub>3</sub> bubbler is shown in Figure 3.7a. Pressure in PCl<sub>3</sub> bubbler is maintained at all times.

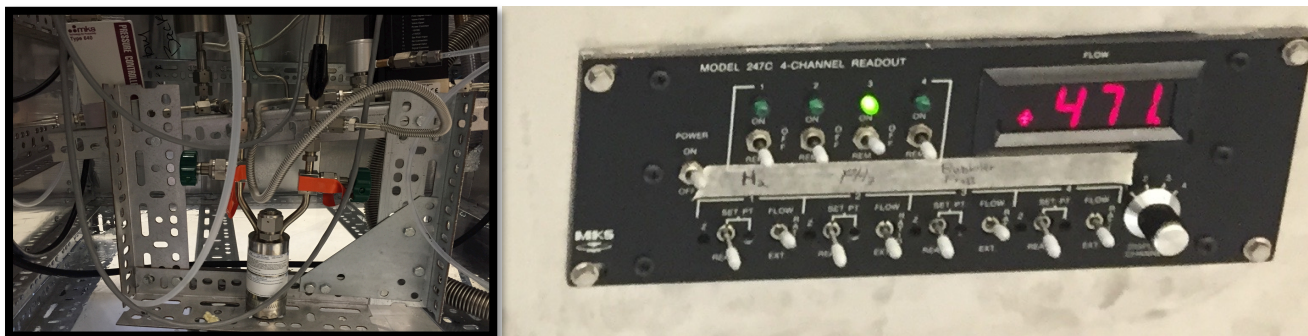


Figure 3.7 (a) the  $\text{PCl}_3$  bubbler assembly and (b) MKS Type 247 gas controller that controls gas flow rate and bubbler pressure.

Typical operating procedure: Upon loading the precursors and deposition stage into the reactor, the following typical operation procedure is utilized. First, vacuum is pulled on the reactor down to 1 torr and cycled to 500 torr with  $\text{H}_2$  three times. This purges virtually all  $\text{O}_2$  and other undesirable gases from the system. After this purge cycle, the reactor pressure is filled to 500 torr with  $\text{H}_2$ . Once reactor pressure is reached, the  $\text{H}_2$  flow is set to a certain rate for operation (125 sccm typically) and the deposition zone is heated to the deposition temperature ( $T_{\text{Dep}}$ ). This is done prior to heating the Ga and Sb precursor zones in order to keep the condensation of reactants from occurring at the deposition substrate surface and only the epitaxial reaction to occur when the appropriate amount of precursors are present.

The tube furnace takes approximately 35 minute to heat up to operating temperatures. Alongside heat-up of the Ga and Sb precursor zones,  $\text{PCl}_3$  is gradually added to the reactor in 5 sccm increments so that phosphorus is available for reaction as the Ga and Sb reactants are first generated. The flow of  $\text{PCl}_3$  is started once temperature for Ga reaches 450 °C then increased by 5 sccm with every 50°C increase until 30 sccm

of  $\text{PCl}_3$  flow till Ga temperature reaches  $700^\circ\text{C}$ . Improvement in this ramp-up procedure could aid in better nucleation and subsequently crystal quality.

Upon reaching precursor temperatures, process conditions are kept constant and the reaction is allowed to carry out for 1 hour. The shutdown is done using the following procedure. First, the  $\text{H}_2$  flow rate is increased to 300 sccm and the tube furnace is shut off. The hydrogen flow rate is increased in order to dilute the available reactants during shutdown. Unfortunately, just as it took 35 minutes for the tube furnace to heat up, it takes nearly twice as long to cool down so as much as possible needs to be done to limit deposition during this stage of the experiment. As the tube furnace cools down, the  $\text{PCl}_3$  is gradually shut off in the opposite manner as they were turned on. As the Ga temperature is decreased from  $700^\circ\text{C}$  to  $450^\circ\text{C}$ , the  $\text{PCl}_3$  flow is decreased by 5 sccm. Instead of just shutting off the flow through the  $\text{PCl}_3$  bubbler at this temperature, flow through the bubbler is diverted through the bypass line and the  $\text{H}_2$  is allowed to purge any remaining  $\text{PCl}_3$  from the line leading to the reactor. Upon  $T_{\text{Ga}}$  reaching  $100^\circ\text{C}$  or lower, the induction heater is switched off and allowed to cool down. Finally, a  $\text{H}_2$  purge cycle is performed 3 times to remove any unwanted gases from the system. The reactor is then vented and the samples are removed using the following unloading procedure.

Unloading/Cleaning/Reloading Procedure: There are several necessary steps to prepare the reactor for operation. At the end of operation of the reactor, a vacuum/purge with  $\text{H}_2$  gas should have been performed. Pumping is continued until the pressure inside reactor reaches approximately 1 torr then refilling it to 500 torr with  $\text{H}_2$  three times. The reactor should then have been vented to the atmosphere and allowed to set overnight. After this

has been done, the following procedures were required between each experiment performed in the reactor. Justification for each step is also included.

(a) *Perform a vacuum/vent cycle 3 times before opening the reactor:* The hydrogen purge cycle performed at the end of each HVPE experiment was used to purge any reactant gases generated during each experiment. Unfortunately, there are also some reactions that can occur between phosphorus and oxygen. In order to mitigate these gases, vacuum should be pulled to 1 torr, then increase to atmospheric pressure three times before opening the reactor and extracting the precursor boats and carbon susceptor that holds the sample.

(b) *Remove the precursors and sample from reactor chamber:* Improvements in procedure have allowed all three reaction elements from the front of the reactor at the KF flange between the gas inputs and quartz tube compression fitting. Using long metal rods with hooks attached at the end, the precursor boats and substrate heater were hooked on to in order to pull them out of the quartz reactor. By accessing only the front of the reactor, the rear of the reactor where the majority of unwanted deposits was left undisturbed.

(c) *Replace empty stage and bake at 900°C for 1 hour under H<sub>2</sub>:* After removing the deposit, the carbon stage was replaced. The method for loading the carbon susceptor is somewhat tedious with the current reactor design as it required access of the back of the reactor where unwanted GaCl and P deposits have accumulated. Future improvements are needed so that these deposits are avoided. These deposits generated gas cloud that made it difficult to hold the temperature stable

at the deposition zone. The gas clouds were caused by previous GaCl deposition in the reaction area and as such needed to be baked off in order to stop the generation of a gas cloud during an experiment.

(d) *Remove stage after repeating purge/vent cycle:* After performing both a hydrogen purge cycles 3 times and an oxygen purge cycle 3 times. The carbon susceptor was removed from the reactor chamber in the same manner as step 2.

(e) *Clean carbon susceptor:* Inevitably during each experiment there was some deposition on the carbon stage as shown in Figure 3.8. This deposition was



Figure 3.8 – Carbon susceptor with deposition from previous reaction.

removed before future experiments were performed. The deposits were finely sanded off the stage leaving it flat and smooth for the next reaction.

(f) *Clean the pressure control valve:* During the course of an experiment deposition occurred at the pressure control valve. The disassembled pressure control valve with deposits on it is shown in Figure 5.9a. The orifice for controlling the pressure is actually quite small and as such any deposition can cause the valve to stick. As such, the pressure control valve was cleaned after each experiment. This required disassembling the VCR fittings on each side of the pressure control valve then completely disassembling the valve inside of the fume hood. The disassembled components were then ultrasonicated in methanol for 30 minutes, rinsed and ultrasonicated in a new methanol solution for 30 more minutes. Removal of the deposits after cleaning is clearly shown in Figure 5.9b. The valve was then reassembled and placed back onto the reactor utilizing two new VCR gaskets.



Figure 3.9 Pressure control valve orifice before and after cleaning procedure.

(g) *Change the pump oil:* Generated reactants reacted with the typical pump oils used in a rotary vane pump. This caused the failure of 3 pumps over the course of these experiments. Furthermore, this reaction caused vapor pressures (60+ torr has been observed) to be emitted from the pump oil once the pump was heated up. As such, after each experiment it was necessary to change the oil in the pump. This required removing the vacuum connections from the pump and removing the pump from the safety enclosure. The contaminated oil was then drained out of the pump. The pump was then refilled with flushing fluid and operated for 1 hour. The flushing fluid was then drained out of the pump and the pump was filled with technical grade white vacuum pump oil. Finally, the pump was reassembled back into the reactor.

(h) *Replace/refill precursor boats:* After each experiment the quartz precursor boats were weighed to see the amount of each precursor lost during the experiment. An appropriate amount of Sb or Ga was then loaded back into the boats and replaced into the reactor.

(i) *Treat Si substrate:* In order to remove the native silicon oxide as well as other organic or metal deposits, a solution of HCl:HF:HNO<sub>3</sub>:DI Water in a 1:1:1:1 ratio was used to etch the samples for 1 hour. The samples were then cleaned with DI water and placed on the carbon susceptor to be loaded into the chamber. Once this step was performed the next experiment needs to be run without any breaks. The reactor could not be loaded then left overnight because this would yield enough time for the Si substrate to oxidize and the vacuum pump could not be operated safely overnight.

- (j) *Reload and position precursors and stage:* Precursor boats were loaded into the reactor from the front and positioned in the middle of their respective temperature zones, the substrate heater was loaded from the back of the reactor and exact position was measured using a premeasured rod.
- (k) *Operation of reactor:* Finally, the experiments were conducted at sub-atmospheric pressures around 500 torr to allow for gas flow inward in the case of leaks.

The above rigorous list of procedures required to prepare the reactor for operation clearly illustrates the need for improvements to the reactor. Several recommendations are provided to make the process an inherently safer process.

3.3.4 Problems and Troubleshooting: In operation of the reactor, there have been many complications that were unforeseen during the design of the reactor. For example, when designing the reactor, excess precaution was taken so that the excess reactants would be captured after they left the vacuum pump. What wasn't considered was just how detrimental these reactants could be to everything deposited on from the deposition zone to the rear of the reactor, vacuum pump included. Another unforeseen phenomenon were the gas clouds generated during operation of the reactor that inhibited line of sight to the deposition stage causing the on/off control to put the induction heater into an infinite work loop where it could heat the substrate heater to temperatures well above the temperature of quartz, representing a major safety hazard in the case of a major breach to the reactor under operation. During the course of the experimentation, many of these problems were overcome. These problems and their solutions are discussed here.



One of the first problems encountered was the difficulty in making leak-tight vacuum connections to the quartz tube utilizing the metal to quartz compression adapters that were provided with the tube furnace. Without a leak-tight seal, oxygen will leak into the reactor during operation and easily oxidize the samples grown. Furthermore, in the adapters current design, the quartz made direct contact with the stainless steel on the inside of the adapters which caused cracking of the tube. An extra set of smaller O-rings were added to the ridge where quartz/metal contact occurred so that, when vacuum was pulled, the quartz tube seated itself up against the O-ring inset in the adapter. Vacuum leaks at the quartz tube adapters stopped occurring after this modification. A photo of a compression fitting and a diagram of the fitting before and after modification are seen in Figure 3.10.

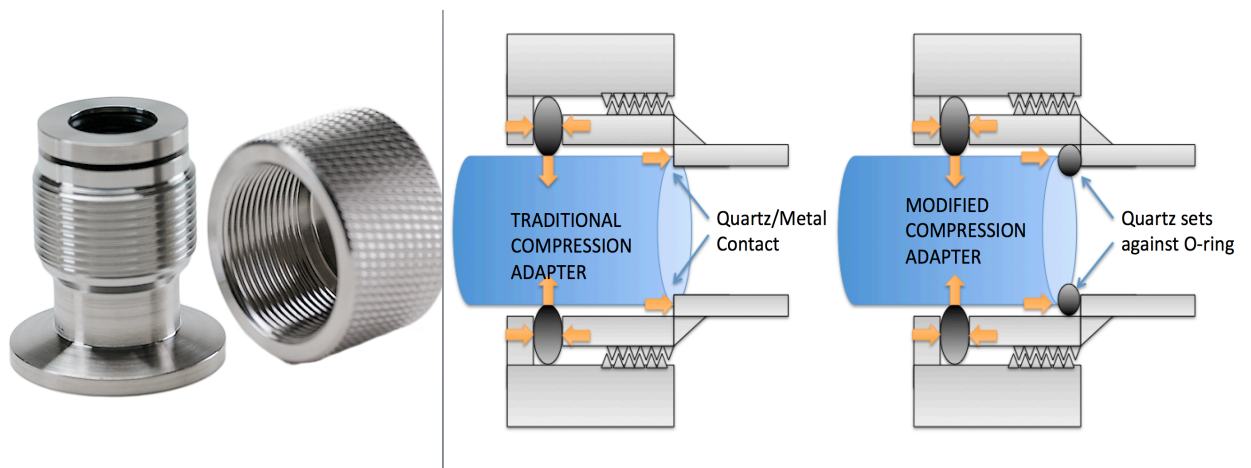


Figure 3.10 Photograph of quartz vacuum compression adapter and diagrams showing the fitting before and after modification.

The next major problem that had to be overcome was the consequences of deposition on the reactor tube and the gas cloud generated. In the initial configuration of the reactor, the pyrometer's line of sight was from the side of the reactor through the quartz tube as can be seen in Figure 3.6a. Within the first set of experiments however it was quickly realized that deposition completely disabled the ability to control temperature at the reaction zone. In order to overcome this, a viewport was installed at the rear of the reactor and the pyrometer was positioned to look through this viewport where no deposition should occur as shown in Figure 3.11. This unfortunately did not fix the issue and needs further modifications of avoiding such deposition.

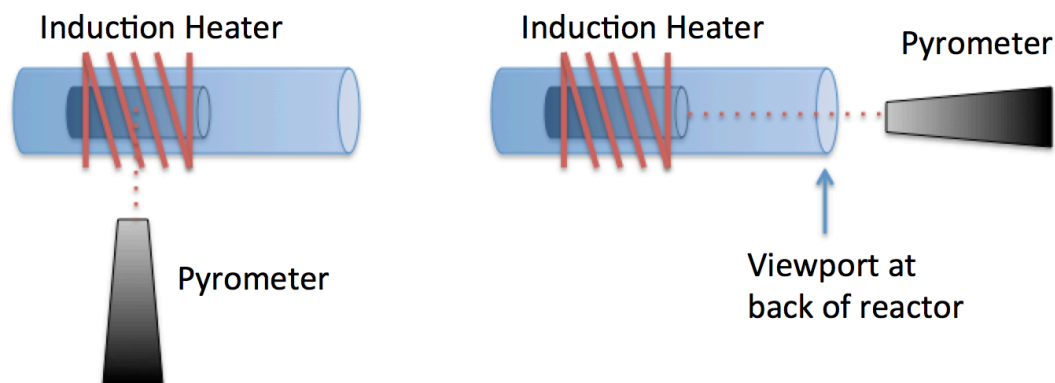


Figure 3.11 Diagrams of set-up before and after modification.

Lastly, due to the detrimental effects of the excess reactants generated during synthesis; many vacuum leaks were found during the course of the experimentation done using the HVPE reactor. Each of these incidences will not be discussed however the method for detecting these leaks will be. Typically to check for vacuum leaks, methanol can be sprayed on a seal while the reactor is under vacuum and an increase in pressure can be seen if there is a leak. This method is not always reliable when the leak is very

small however. In order to detect extremely small leaks, vacuum was pulled on the reactor chamber then refilled to 500 torr with hydrogen and allowed to maintain pressure. A hydrogen detector was then operated and run over the course of the reactor. Even though the reactor is under vacuum conditions, the high diffusion rate of H<sub>2</sub> allows facile detection of H<sub>2</sub> at any leak.

### 3.4 Materials Characterization

#### 3.4.1 Structural Characterization

Morphologies of the resulting GaSb<sub>x</sub>P<sub>1-x</sub> samples were characterized using Tescan and FEI scanning electron microscopes (SEM). Samples were cleaved and the cross sectional interfaces of the GaSbP films were observed in order to identify interface growth, grain boundaries and other growth defects. An estimate of film thickness will also be able to be made from this cross section. Electron dispersive x-ray spectroscopy (EDS) point source measurements were employed to determine approximate elemental compositions over surface and cross sections of the thin films.

Transmission electron microscope (TEM) + EDS line scan experiments were performed on GaSbP alloy nanowires to confirm composition of the ternary alloy. It is important to understand phase purity and composition of resulting samples using x-ray diffraction (XRD) data. GaSb and GaP both have zinc blende crystal structures and their XRD patterns have very similar signatures, just shifted in degrees of where peaks for each crystal plane occur. If GaSbP is present as a ternary alloy it will show a singular peak that is shifted somewhere between peaks for GaP and GaSb for that respective crystal plane. Starting with the lowest amount of antimonide alloying, XRD of these

films should exhibit GaP-like peaks but with a shift in lattice expansion as more antimonide is incorporated into the ternary lattice such as in previous work<sup>19</sup>. Ternary alloys in the GaSb regime should show GaSb-like peaks with a shift in lattice contraction as more phosphorus is incorporated into the lattice. From these shifts in XRD peaks, lattice constants were extracted and correlated with DFT results. Furthermore, utilizing Vegard's law for ternary alloys, approximate compositions based upon these shifts were obtained and compared the alloy composition measurements from EDS and band gap measurements.

Raman spectroscopy was also performed to investigate the vibrational and rotational modes exhibited by the bonds in GaSbP. The generated Raman spectrum effectively acts as a fingerprint for the molecule. Responses similar to that of GaSb and GaP can be expected along with new responses that result from the ternary interaction.

### 3.4.2 Optical Characterization

UV-Vis spectroscopy was used in order to determine band gap characteristics of the GaSbP alloy. Diffuse Reflection UV-Vis experiments were performed on GaSbP because they were opaque and grown on Si. Tauc plots were generated utilizing the Kubelka-Monk method for interpreting UV-VIS diffuse reflectance measurements and from it the band gap and transition type (direct/indirect) was determined. By coupling this band gap data with the alloy composition and lattice constant information inferred from XRD and EDS observations on band gap and Sb incorporation into GaP were made. Next, profilometry was conducted and the sample thickness was determined.

Photoluminescence (PL) experiments at 77 K were then undertaken to understand more about the optical transitions in the samples. Under low temperatures, excited electrons are less likely to utilize phonons to thermally excite to higher energy levels and at the same time less likely to relax by phonon release to non-radiative recombination centers. Therefore, PL should be observed from the true band edge and defect states of the material under low temperature conditions.

A review of impurity states in GaP can help to identify whether dopants are present in GaSbP and aid in determining whether a photoluminescence response is due to radiative recombination or due to photoluminescence from a direct band edge. Carbon could be introduced from the graphite susceptor used to heat the deposition zone. It can form a defect acting as an acceptor approximately .05 eV above the valence band of GaP<sup>127</sup>. Silicon can form gallium or phosphorus vacancies and acts as a donor .08 eV below the conduction band or an acceptor .21 eV above the valence band respectively<sup>128</sup>. Oxygen acts as a deep level donor with an impurity state almost directly in the middle of band gap of GaP at .89 eV below the conduction band<sup>129</sup>. Gallium can exist in three different acceptor vacancy states with energy levels approximately .38 eV, .8 eV and .9 eV above the valence band<sup>130</sup>. Phosphorus vacancies act as acceptor states however work to locate the vacancy energy levels has been inconclusive<sup>131</sup>.

### 3.5 Electrochemical and Photoelectrochemical Characterization

Prior to photoelectrochemical characterization, GaSbP alloy samples were prepared into electrodes for electrochemistry in such a way that they are electrically contacted but only the face of the sample is exposed to electrolyte. Photoelectrochemical experiments were carried out in a house-made three-port photoelectrochemical cell with a

quartz window for transmission of illumination. Measurements were taken in 3M H<sub>2</sub>SO<sub>4</sub> or sodium sulfate solution with a platinum mesh counter electrode and Accumet Ag/AgCl reference electrode filled with 4M KCl. Illumination was provided by a Newport Instruments Oriel 300W Xe lamp solar simulator that was calibrated to the AM 1.5 spectrum. A Thorlabs D10MM power meter with PM100 readout was used to measure illumination intensity and measurements were taken using a Princeton Applied Research Model 273A Potentiostat/Galvanostat.

### 3.5.1 Open circuit potential measurements

First, open circuit potential (OCP) measurements were performed under concentrated illumination to determine conductivity type of the material and the flat band potential. In OCP experiments, no current or voltage is applied to the semiconductor and the voltage between the working and reference electrodes is measured in the dark. Illumination is then applied to the working electrode and if the material is photoactive, a change in the measured voltage will occur. As discussed in Chapter 2, a shift to more positive energy levels upon illumination indicates a p-type response while a shift to more negative energy levels upon illumination indicates an n-type response.

### 3.5.2 Chopped I-V Measurements

The photocurrent of the material and onset potential, three electrode linear sweep voltammetry (LSV) testing was performed. Depending on the conductivity type obtained from OCP, voltages were applied and swept in the positive or negative direction and the

current at these voltages were measured in the dark and under illumination. The difference between the light and dark current at a given voltage is the photocurrent generated by the sample at that voltage.

### 3.5.3 Unbiased two-electrode chronoamperometry

Assuming photocorrosion at the semiconductor is not occurring, photocurrent observed under these measurements provides verification of true band straddling of the water splitting reaction redox potentials and demonstrates water splitting without external bias.

## CHAPTER 4

### COMPUTATION STUDIES AND EXPERIMENTAL VALIDATION OF GASBP ALLOYS

In this chapter, the preliminary studies involving computational predictions and experimental studies for validation for  $\text{GaSb}_x\text{P}_{1-x}$  alloys in the dilute antimonide regime are presented. First, DFT+U calculations are performed in collaboration with Professor Madhu Menon to understand the band gap and band edge energetics of GaSbP alloys. Experimentally, GaSbP alloys are synthesized as nanowires using reactive vapor transport schemes.

#### 4.1 Density function theory

The theoretical work modeled bulk GaP with zinc blende structure using a relatively large, 216 atom  $2 \times 2 \times 1$  gamma-centered pack supercell with periodic boundary conditions. The size of the supercell is large enough to allow for random distribution of Sb atoms.  $\text{GaSb}_x\text{P}_{(1-x)}$  structures are obtained by substituting P atoms with Sb. In each case considered, both the cell volume and the individual atomic positions have been fully optimized without any symmetry constraints. The optimized structure of the alloy with composition for four incorporations of Sb ( $x=0.036$ ) is shown in Figure 4.1a.



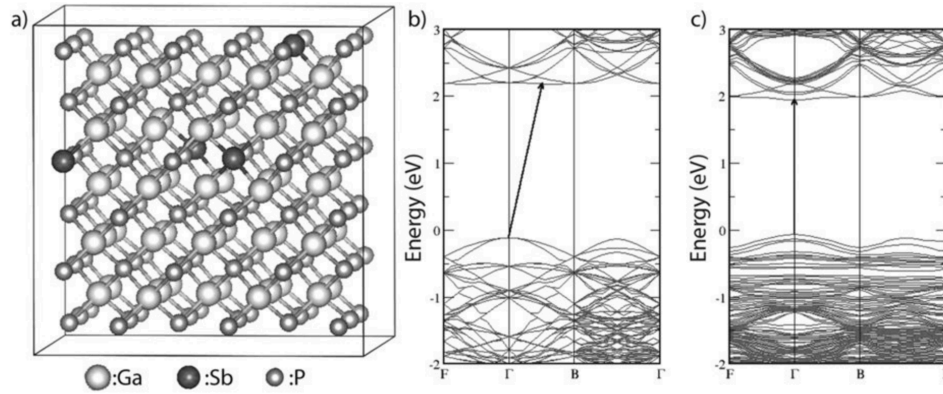


Figure 4.1 (a) 216 atom-supercell of  $\text{GaP}_{.963}\text{Sb}_{.037}$  optimized using DFT calculations and comparison of density of states diagrams for (b) GaP and (c)  $\text{GaP}_{.963}\text{Sb}_{.037}$  showing the direct optical band gap transition.

The alloying of GaP by Sb introduces impurity (*spd*-hybridized Sb-related) states at the gap edges. Those at the valence band maximum (VBM) are more pronounced (not shown). The Sb-related states lead to significant modifications in the energy bands. As evident from Figures 4.1b and 4.1c, the Sb-states induce a strong band repulsion at the conduction band minimum (CBM) of the GaP bands that lead to the lowering of the bands at the  $\Gamma$ -point which results in turning the indirect gap into a direct one. On the other hand, new Sb bands are introduced at the VBM. The new bands lead to a band repulsion that lifts the degeneracy of the GaP-bands at the  $\Gamma$ -point, which in turn, leads to a small reduction in the energy gap. This trend in band gap reduction is seen for increasing Sb incorporation alongside a corresponding increase in d-spacing (Figure 4.2).

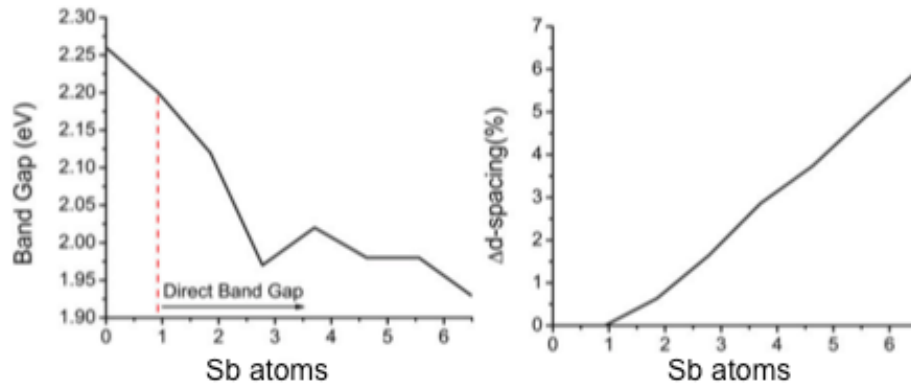


Figure 4.2 (a) Change in band gap and (b) percent change in d-spacing for # of Sb atoms incorporated in the 216 atom supercell. Both plots were obtained from DFT calculations.

The band gap data points depend on the configuration of the distributed Sb impurities. So there will be an error bar associated with each calculated point of the data. Unfortunately the estimation of the error bars is computationally prohibited. For this reason, the plot of band gap as a function of  $x$  can be better redrawn and instead of having the curve simply connect the data points, the calculated data can be fitted to a least square polynomial function. As long as no Sb-Sb interactions are present (i.e. the Sb atoms are far from each other) a linear variation of band gap vs.  $x$  could be expected as this results from the appearance of Sb states in the band edges and band repulsion effects. Both of these effects however, may not be simply proportional to  $x$  for large enough  $x$ . Nevertheless, in the range of the studied Sb concentrations, (maximum 3-4 Sb atoms in 108 set of P-atoms) no Sb-Sb interactions should be expected and therefore the effect from each Sb atom should be additive.

Another important study is to estimate the band edge location with respect to vacuum. Recall that the ionization potential (IP) of a (non-polar) semiconductor specifies

the energy of the VBM with respect to vacuum.<sup>132</sup> Very recently, the same group reported accurate IP estimation for a set of non-polar semiconductors in good agreement with experiment.<sup>133</sup> For GaP and GaSb, the corresponding ionization potential values are in the ranges [5.95-6.01] eV and [4.70-4.94] eV. In view of these, the VBM of GaP is at approximately 6.0 eV below the vacuum level while the CBM is approximately at the energy:  $\text{VBM} + E_{\text{gap}}$ . In order to find the variation of the VBM of GaP as the Sb concentration,  $x$ , is varied, the recently proposed<sup>134</sup>, virtual crystal approximation (VCA) extension of Harrison's method for evaluating the VBM was used<sup>135,136</sup>. The values so obtained are shifted in such a way that the VBM-value for  $x=0$  (i.e., that for GaP) coincides with values that are negative of the IP of GaP. In order to find the CBM as a function of Sb-concentration, the band gap values for each concentration are added to the corresponding VBM at the same concentration.

A plot of VBM and CBM with respect to vacuum in terms of Sb-concentration is presented in figure 4.3 in comparison to the HER and OER potentials. As can be seen from the position of these bands, theoretical results predict the straddling of the HER and OER for up to  $x = .074$  incorporation of Sb.

## 4.2 Amorphous GaSbP NWs

Initial growths were performed utilizing a reactive vapor transport scheme. Gallium antimonide and gallium phosphide powders were evaporated at temperatures between 650°C and 900°C in a boron nitride crucible and deposits reacted at a lower temperature quartz substrate placed at the top of the BN crucible. For samples grown at

heater temperatures between 750°C and 870°C, thin films with nanowire morphologies were synthesized.

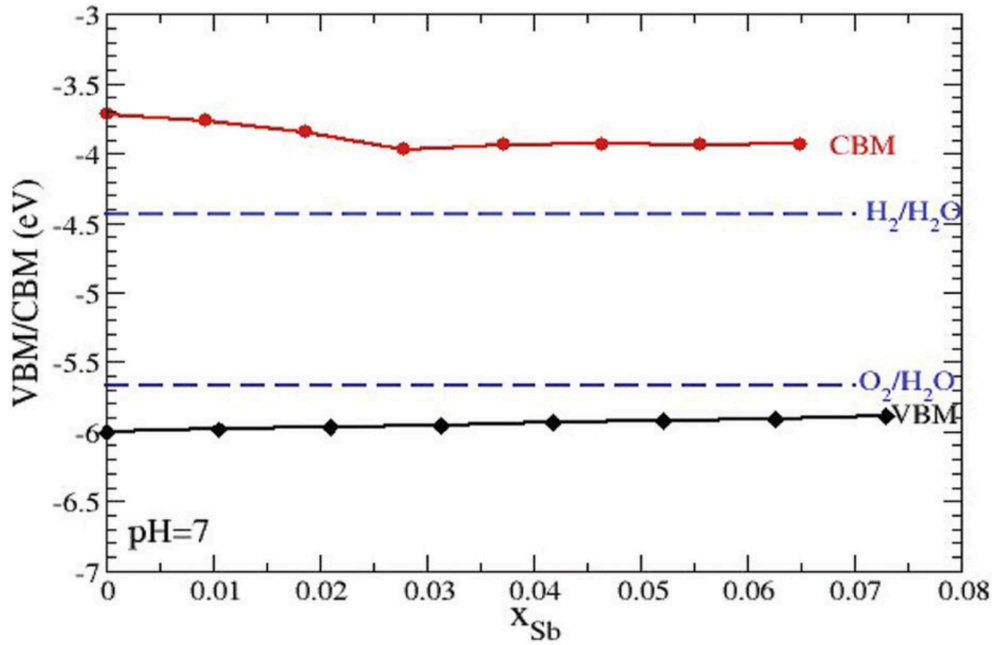


Figure 4.3 Valence band maximum and conduction band minimum positions calculated by the generalized Harrison's approach as a function of Sb concentration in Ga(Sb)P at pH = 7 alongside the redox potentials for the HER and OER.

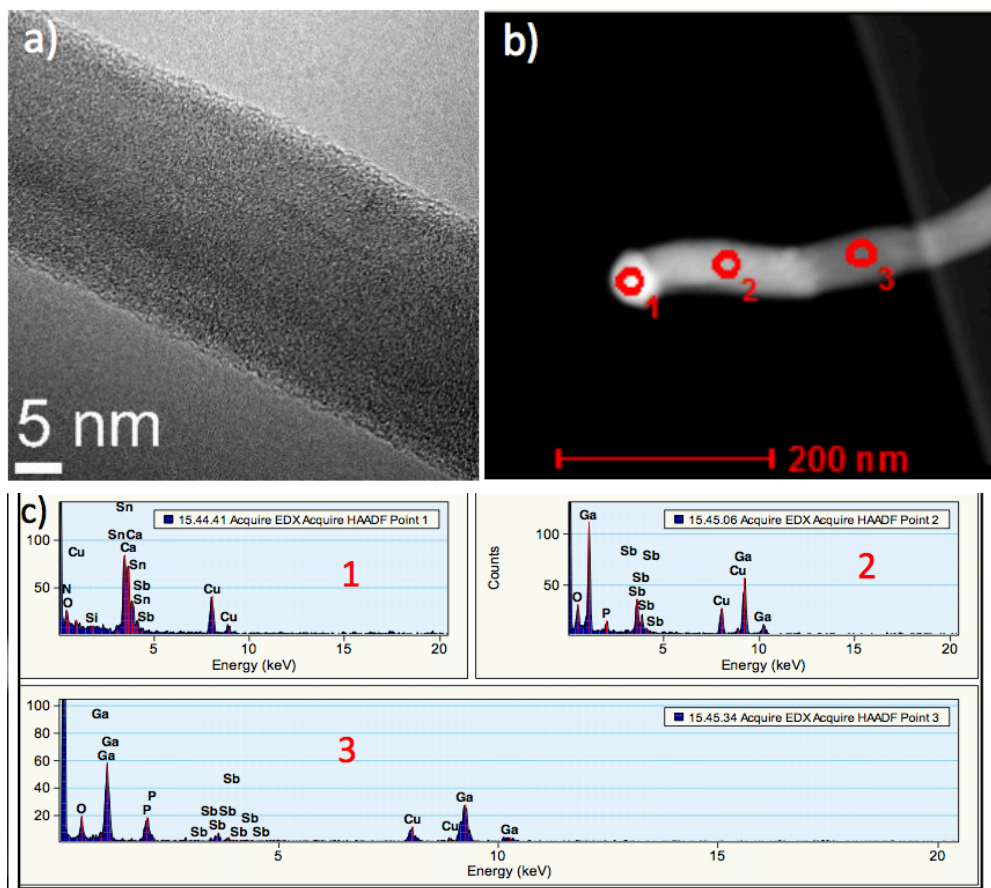


Figure 4.4 (a) HRTEM imaging of an amorphous nanowire that contains Ga, Sb, P, Cu and O. Figure 2b-c show 3 TEM-EDAX point source measurements along an nanowire indicating an antimony copper eutectic droplet led nanowire growth

HR-TEM shows that the nanowires possess an amorphous morphology (Figure 4.4a) and TEM-EDAX shows that they consist of gallium, antimony and phosphorus but also contain small amounts of copper and oxygen. The copper could have come from impurities within the reactor or ball mill while the oxygen may have been caused by a leak in the reactor. TEM EDAX on three points along the length of a single nanowire shows that the nanowires grew by copper-antimony tip lead growth. This can be seen in

Figure 4.4b-c, at point 1 (droplet) the composition is primarily antimony and copper and as you move along the wire the Sb and Cu concentrations go down while gallium and phosphorus concentrations go up. No UV-Vis nor photoelectrochemical responses were observed from these materials. From these experiments it could not be confirmed that any ternary alloy was made.

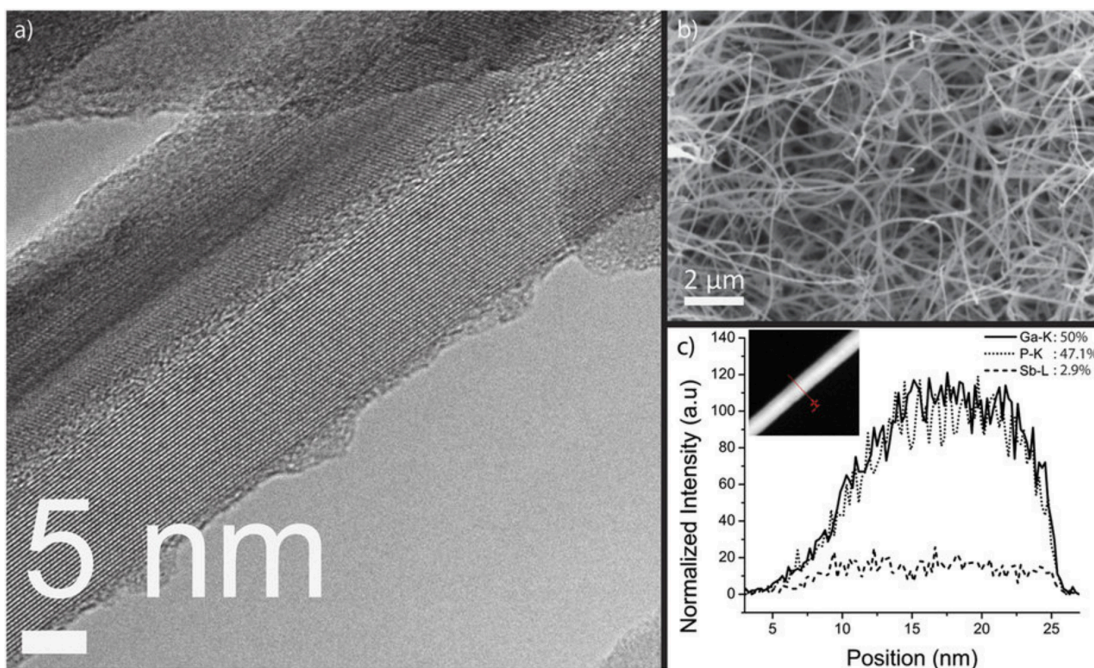


Figure 4.5 – (a) A high resolution transmission electron micrograph of a GaSbP nanowire; (b) A scanning electron micrograph of GaSbP Nanowires; and (c) An EDS line scan for composition using transmission electron microscopy showing Ga, Sb and P concentration across a radial cross section of the GaSbP nanowire from part a.

### 4.3 Single crystal GaSbP NWs

$\text{GaSb}_x\text{P}_{(1-x)}$  NW samples were grown by microwave plasma enhanced co-evaporation. Ga and Sb metals were placed on opposite sides of a graphite susceptor with clean growth substrates placed in between. The reactor was pressurized with  $\text{H}_2$  to

chamber pressure of 100 torr and microwave plasma was held over the susceptor at powers between 800 W and 1000 W. Upon stabilizing the plasma at the target operating power, DTBP was fed into the reactor. The reaction was allowed to take place for two hours. The growth mechanism is similar to that of self-catalyzed growth of nanowires in a reactive vapor transport mode.

The resulting  $\text{GaSb}_x\text{P}_{(1-x)}$  samples were investigated by both transmission electron microscopy (TEM) and scanning electron microscopy (SEM) and exhibited nanowire morphologies from 20 nm up to 1  $\mu\text{m}$  in diameter and several microns in length (Figure 4.5a). A cross section of the  $\text{GaSb}_x\text{P}_{(1-x)}$  sample was exposed by cleaving the sample and investigated using energy dispersive X-ray spectroscopy (EDS). At the interface between the silicon and film growth, only Ga and Sb are present at a 1:1 atomic ratio as a thin film. This formation of GaSb at the growth interface is expected, however, due to the operation of the plasma with only Ga and Sb present before the addition of the phosphorous precursor, DTBP. At the surface of the sample, however, the presence of phosphorus is observed in addition to Ga and Sb.

XRD of five  $\text{GaSb}_x\text{P}_{(1-x)}$  samples show major peaks for GaSb as well as a set of peaks similar to GaP, but shifted toward those of GaSb (Figure 4.6). The XRD peak at 25.3 degrees indicates the presence of GaSb which is expected to be formed in the initial stages of growth prior to the introduction of phosphorous precursor. For the (111) reflection, the observed Bragg angle shifts toward lower angles from 28.3 degrees expected for pure GaP (111); this peak shift can be used for estimating the Sb composition in the  $\text{GaSb}_x\text{P}_{(1-x)}$  alloy using Vegard's law. The Sb compositions based on

XRD peak shift for various samples were determined to be between  $x = 0.06$  and  $x = 0.12$ .

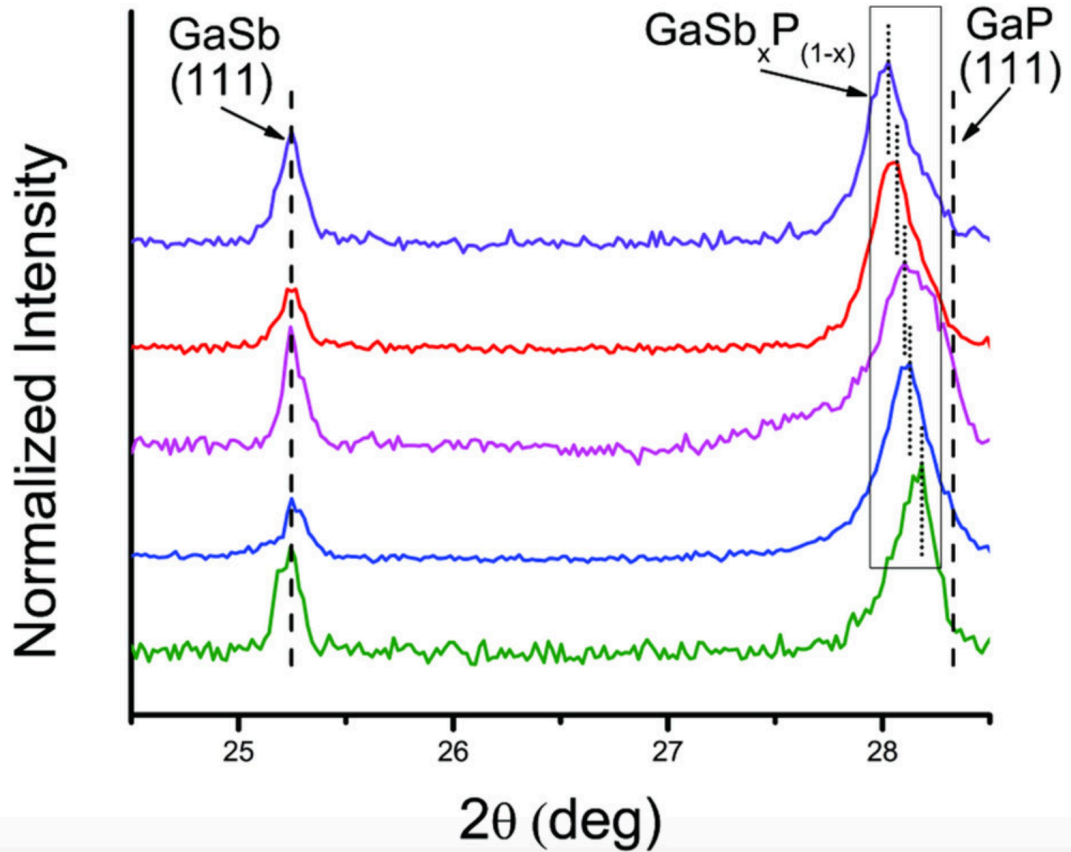


Figure 4.6 XRD pattern of GaSbP samples indicating alloy compositions. Individual concentrations were determined to be  $x_{Sb} = 0.121, 119, 106, 100$  and  $0.059$  (from top to bottom).

Diffuse reflectance ultraviolet-visible spectroscopy (UV-Vis) measurements for the above five  $\text{GaSb}_x\text{P}_{(1-x)}$  samples were performed. Tauc plots for the direct allowed transition indicating direct band gaps between 1.33 and 1.72 eV are shown in Figure 4.7. The measurement utilizes absorption over an area exceeding  $1 \text{ cm}^2$  such that the estimated optical band gap is an average value. Most importantly, the UV-Vis data and its



corresponding analysis using Tauc plots did not show the presence of binary III-V phases (GaSb or GaP) thus confirming the presence of primarily ternary III-V alloys.

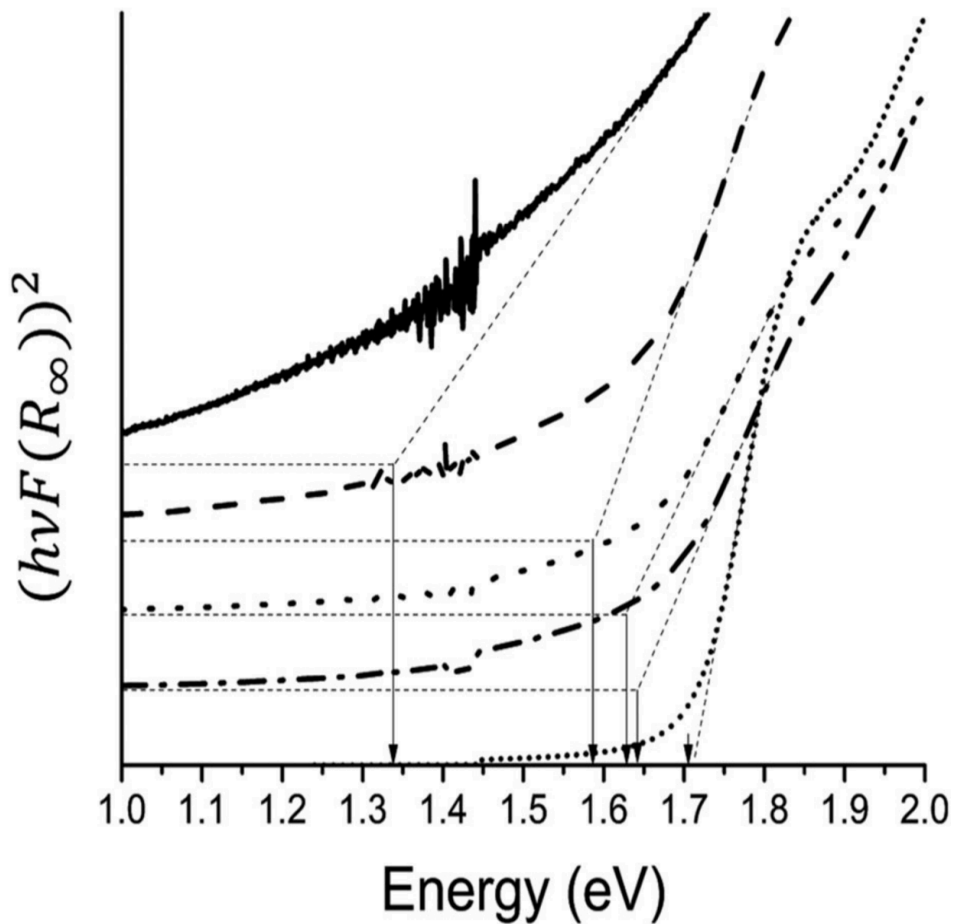


Figure 4.7 Tauc plot analysis for the direct allowed transition from UV-Vis diffuse reflectance for the  $\text{GaSb}_x\text{P}_{(1-x)}$  samples indicating direct band gap transitions from 1.33 eV up to 1.72 eV.

In all of the samples, there is a spatial variation for compositions of ternary alloys. In some samples, the variation for Sb composition can be anywhere from  $x = 0.02$  to  $x = 0.24$  over a two-inch area. However, there is little or no (less than  $x = .01$ ) variation in

Sb composition along the length of each nanowire. High resolution TEM images in Figure 4.5b reveal high single crystallinity for  $\text{GaSb}_x\text{P}_{(1-x)}$  nanowires with no defects and no amorphous sheath. Increased amount of stacking faults were observed in nanowires with high amounts of Sb composition. TEM-EDS line-scan profiles shown in Figure 4.5c radially across the nanowire diameter show similar profile curves for Ga, P, and Sb indicating true alloy formation with no segregation. Furthermore, no binary (GaSb or GaP) nanowires were observed.

Micro-photoluminescence (PL) measurements were performed using a spot size on the order of few microns on the 1.72 eV band gap GaSbP sample at liquid nitrogen (77K) and room temperature (300 K). At 77 K, a  $\text{GaSb}_x\text{P}_{(1-x)}$  nanowire film sample showed responses at 1.73 and 1.82 eV. A GaP control sample at this temperature showed a response at 2.3 eV as expected and no response was observed at 300 K due to the indirect nature of band gap. From the PL measurements at 77 K shown in Figure 4.8a, it can be inferred that there is no pure GaP phase present in the measured  $\text{GaSb}_x\text{P}_{(1-x)}$  nanowire film region. At liquid nitrogen temperatures, non-radiative recombination is minimized and electrons are trapped in the GaP conduction band edge only allowing them to emit PL from that band. Thus, if there was binary GaP present in the measurement area at 77 K, an emission at  $\sim 2.3$  eV would be expected. PL measurements at 300K have yielded varying PL peak positions at various locations indicating different direct band gap values with different compositions for nanowires. The observed PL peak positions ranged from 1.73 eV to 2.21 eV across the same sample as shown in Figure 4.8b. The range of band gaps estimated using PL are consistent with optical band gap measurements for this material obtained by UV-Vis spectroscopy. UV-Vis and XRD

techniques use averaged information over 1 cm<sup>2</sup> area while PL spectroscopy's information is from about few micron square area and TEM data corresponds to individual nanowire.

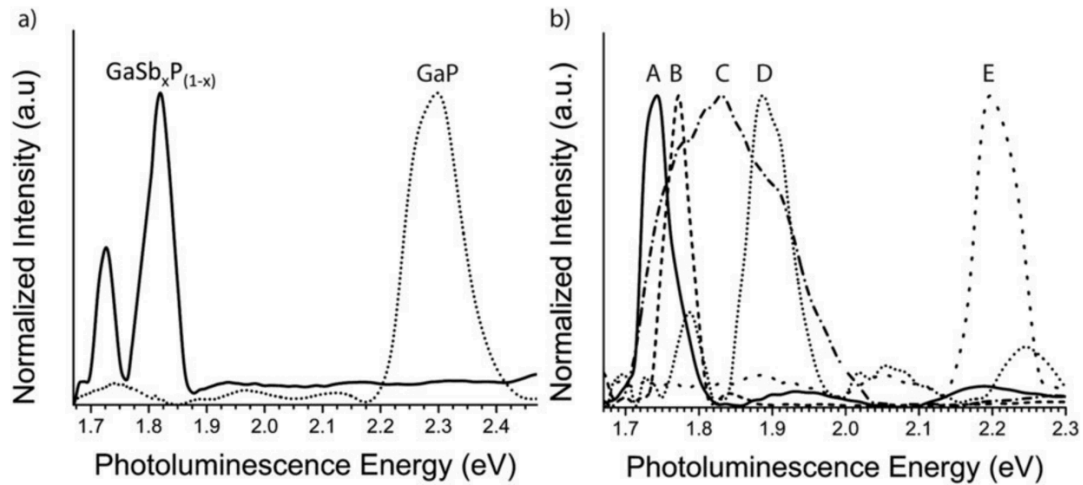


Figure 4.8 (a) Visible photoluminescence spectra at liquid nitrogen temperature (77 K) for GaSbP alloy containing peaks at 1.73 and 1.84 eV and a peak at 2.3 eV for GaP control sample; (b) Visible photoluminescence from various regions (A–E) of GaSbP nanowire film sample at room temperature that exhibit peaks at 1.74 eV (A), 1.77 eV (B), 1.84 eV (C), 1.89 eV (D), and 2.21 eV (E).

The room temperature PL peaks could also be due to the presence of impurity states within the band gap of the GaP semiconductor. As discussed previously, in order to be sure that these PL responses are not from other impurity donor and acceptor levels, the levels for possible donors and acceptors are reviewed. Silicon acts as a shallow donor ( $E_c - .085$  eV) when found in a Ga vacancy and a shallow acceptor ( $E_v + .21$  eV) when found in a phosphorus vacancy, if emission occurred from this donor to acceptor level, a PL

emission of approximately 2 eV would be expected. Oxygen can only be found in phosphorus vacancies and acts purely as a deep level donor ( $E_c - .89$  eV) so an approximate emission from this deep state would be expected at 1.41 eV<sup>137</sup>. Three levels of Ga vacancies can exist, all of which act as acceptors, and based upon MS XCK cluster model calculations by Fazzio, Brescansin and Leite have values as follows:  $V_{Ga}^0 \sim E_V + .38$  eV,  $V_{Ga}^1 \sim E_V + .8$  eV, and  $V_{Ga}^2 \sim E_V + .9$  eV<sup>138</sup>. If these vacancies were present expected emissions would occur at 1.92 eV, 1.5 eV and 1.4 eV. So, the observed room temperature and cold PL peaks correspond to band edge to band edge transitions and thus represent band gaps for the synthesized  $GaSb_xP_{1-x}$  alloy nanowires.

As can be seen in Figure 4.9a, the Raman peak observed at  $201\text{ cm}^{-1}$  is shifted from that expected for pure GaSb phase. This slight mismatch can be attributed to both the nanocrystalline and ternary nature of the  $GaSb_xP_{(1-x)}$  alloy. Peak shifts could arise from temperature rise within nanowire samples due to laser irradiation<sup>139</sup>. In Figure 4.9b, Raman spectra for a pure GaP control sample is presented along with that obtained for a  $GaSb_xP_{(1-x)}$  sample. The data shows a significant peak shift for the two major peaks expected for GaP phase and also an additional peak in that region. Additional peaks at  $464$ ,  $637$  and  $750\text{ cm}^{-1}$  are also observed. No previous Raman data exists for the  $GaSb_xP_{(1-x)}$  system. Similarly, additional peaks were observed in dilute ternary  $GaSb_xN_{1-x}$  alloys in addition to those expected for binary phase, GaN.<sup>19</sup> The origin of such peaks needs further investigation.

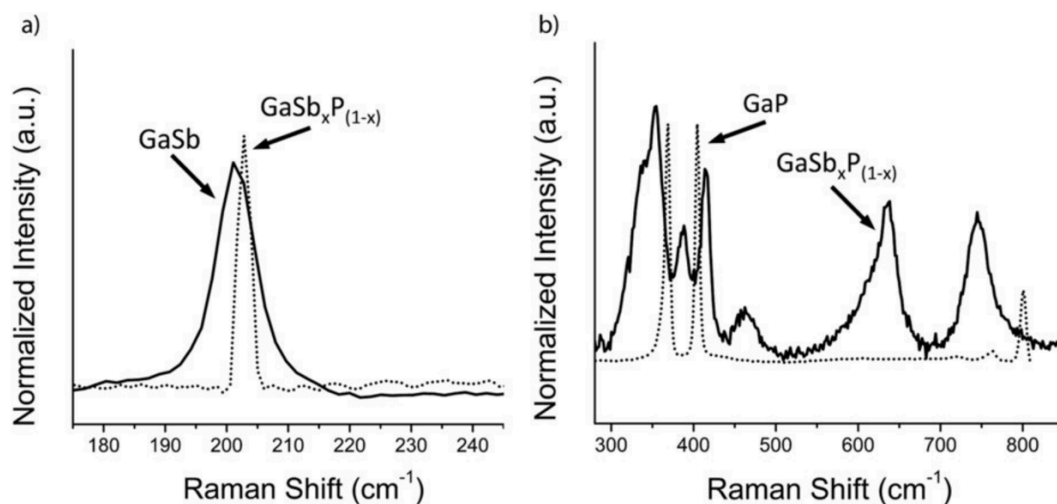


Figure 4.9 Raman of GaSbP against (a) GaSb and (b) GaP control samples. Major peaks for GaSbP are observed at  $201\text{ cm}^{-1}$ ,  $356\text{ cm}^{-1}$ ,  $390\text{ cm}^{-1}$ ,  $417\text{ cm}^{-1}$ ,  $464\text{ cm}^{-1}$ ,  $637\text{ cm}^{-1}$  and  $750\text{ cm}^{-1}$ .

Preliminary OCP measurements were performed on the GaSbP NW samples. All PEC measurements on these GaSbP NWs were performed at 1 sun of illumination. Upon illumination, a positive shift in potential was observed providing conclusive evidence of p-type conductivity making it a promising candidate for use as the photocathode in a water splitting cell (Figure 4.10a). Three electrode linear sweep voltammetry measurements under chopped illumination show a photocurrent density of approximately  $40\text{ }\mu\text{A}/\text{cm}^2$ , however the large cathodic current observed without illumination would suggest that, simultaneously, a corrosion reaction may be happening (Figure 4.10b). Furthermore, photoresponse is seen at potentials very close to the HER indicating an onset potential for photoactivity unbiased. As such, unbiased two electrode IV measurements were performed on the 1.6 eV band gap GaSbP sample grown on quartz substrate. A photocurrent of approximately  $15\text{ }\mu\text{A}/\text{cm}^2$  was observed (Figure 4.10c).

These chronoamperometry essays show that the photoactivity remains constant over time indicating it is a result of true water-splitting by  $\text{GaSb}_x\text{P}_{(1-x)}$ .

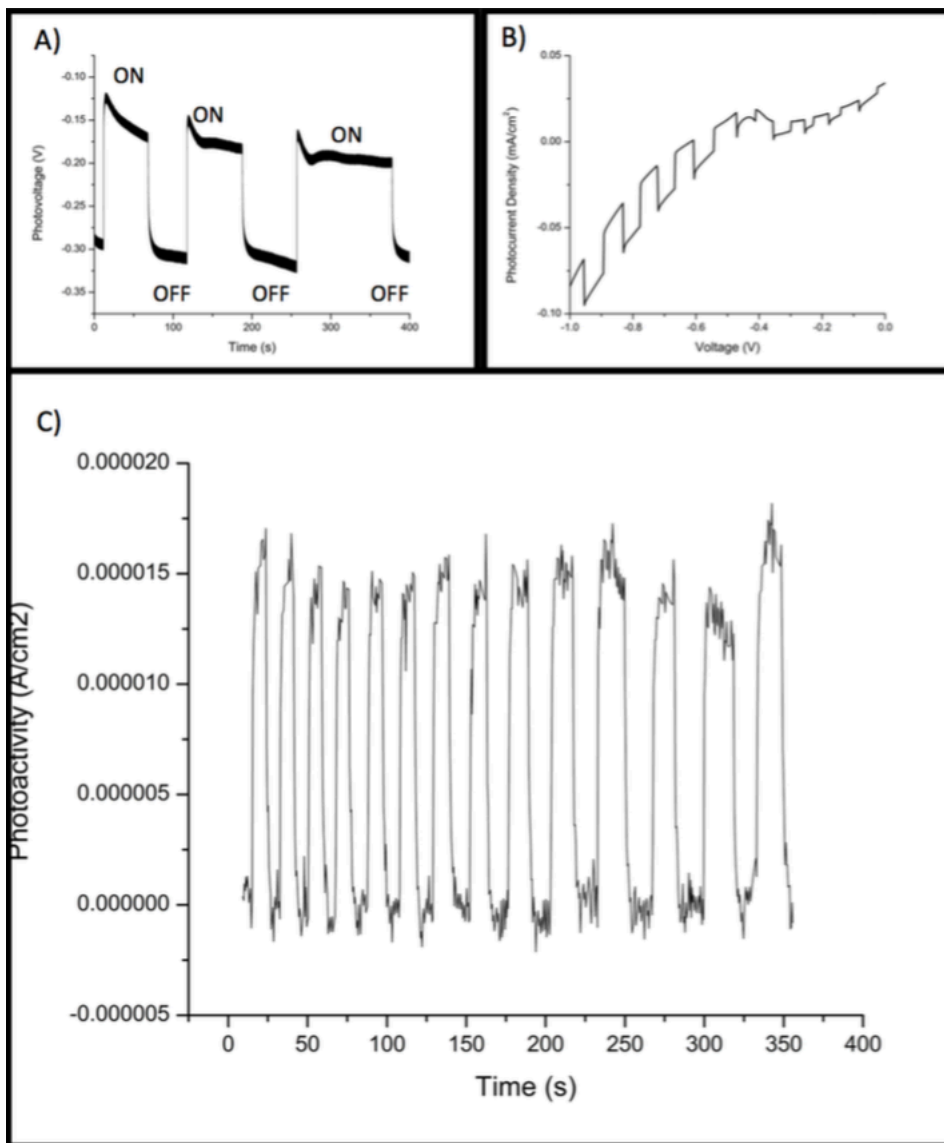


Figure 4.10 Fundamental photoelectrochemical characterization at 1 sun illumination including linear sweep voltammetry showing an approximate photocurrent density of 40  $\mu\text{A/cm}^2$  at -0.65 V (a), open circuit potential under chopped illumination indicating p-type conductivity (b) and unbiased two electrode chronoamperometry under chopped

illumination showing approximately  $15 \mu\text{A}/\text{cm}^2$  photoactivity and confirming true water splitting.

These studies served as a preliminary look into GaSbP and its potential as a photoabsorber. These studies however were not completed utilizing the reactor scheme for making a III-V semiconductor. The reactor was chosen because it was the only phosphorus source available in our lab but the variability inherent to the process did not yield samples that could clearly correlate composition to band gap. These studies did however serve to motivate the building of a halide vapor phase epitaxy (HVPE) reactor capable of making high quality GaSbP epi-layers. In the following chapter, the rationale for choosing HVPE as the reaction scheme to grow GaSbP is explained.

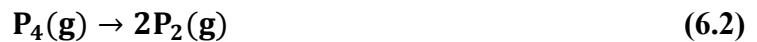
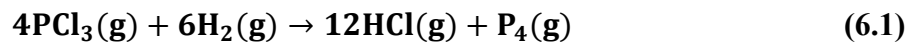
CHAPTER 5  
HALIDE VAPOR PHASE EPITAXIAL GROWTH AND  
PHOTOELECTROCHEMICAL CHARACTERIZATION OF GASBP FILMS

In this chapter, the experiments performed utilizing the HVPE reactor are discussed. The resulting samples were characterized using structural, optical and photoelectrochemical techniques to investigate properties such as morphology, elemental composition, band gap and photo-activity.

### 5.1 Reaction chemistry

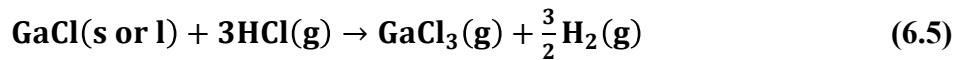
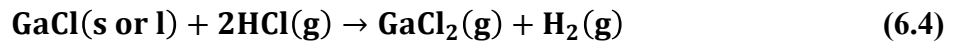
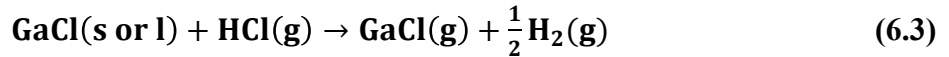
HVPE utilizes halogen containing gases such as HCl, HBr, or HI to react and transport both group III in the gas phase as metal halide gases such as  $\text{GaCl}_{(1-x<x<3)}$  or  $\text{InCl}_{(1-x<x<3)}$ . These metal halides then react with a group V gas precursor such as  $\text{NH}_3$ ,  $\text{PH}_3$  to form the III-V alloy. Group V precursors can also be provided in the form of halide gases such as  $\text{PCl}_{(1-x<x<3)}$  or  $\text{SbCl}_{(1-x<x<3)}$ .

For these experiments, phosphorus is provided in the form of a  $\text{PCl}_3$  bubbler. When hydrogen is used as a carrier gas to transport the  $\text{PCl}_3$  it readily reacts to form gaseous  $\text{P}_2$  and HCl as seen in equations 6.1 and 6.2.

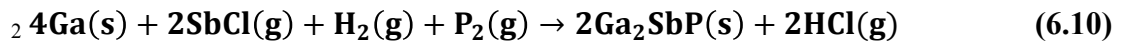
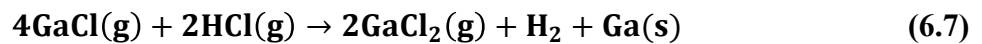




Ga has a +3 oxidation state and as such, when reacted with the HCl generated in equation 6.1 can form GaCl, GaCl<sub>2</sub>, GaCl<sub>3</sub> or 2(GaCl<sub>3</sub>) gaseous species by the reaction pathways shown in Equations 6.1-6.4. Experiments by Koukitsu et al have shown that at temperatures above 500°C the formation of GaCl as seen in Equation 6.1 dominates producing partial pressures of GaCl equivalent to the incoming partial pressure of HCl.<sup>111</sup> Antimony has an oxidation state of +5 and as such can form SbCl, SbCl<sub>2</sub>, SbCl<sub>3</sub>, SbCl<sub>4</sub> and SbCl<sub>5</sub> gaseous species. Thermodynamic analysis on the SbCl<sub>x</sub> system to see which forms dominate is not present in literature and further investigation of this is warranted.



At the deposition zone, GaCl, SbCl and P<sub>2</sub> will be present to react. The formation of GaP occurs as seen in Equations 6.7 and 6.8. The formation of GaSb is shown in Equation 6.9 and finally the reaction schemes are combined to shown the formation of GaSbP shown in Equation 6.10.



In order to provide compositional control of the gaseous precursors there are several variables available for controlling the materials growth using HVPE reaction scheme. To control the amount of Sb and Ga precursors available for reaction, the temperature in each precursor's temperature zone can be changed and an increase in temperature will produce more gas phase. Furthermore, the H<sub>2</sub>/HCl ratio in the reactor can be changed in order to change the ratio of Ga and Sb precursor flux for deposition. In Equations 6.7-6.10 suggest potential reactions that could happen during deposition of GaSbP films. Even though, the mechanism is not entirely clear, GaCl, SbCl and PCl species could potentially act as growth species in the formation of GaSb<sub>x</sub>P<sub>1-x</sub> films.

The amount of phosphorus precursor available for reaction can also be changed using multiple approaches including flow rate of precursor through the bubbler, the pressure that the bubbler is held at and the bubbler temperature. At room temperature, PCl<sub>3</sub> provides approximately 150 torr vapor pressure, which is more than adequate for the scope of these studies, and as such no control over the bubbler temperature is provided in this HVPE reactor.

Finally, the deposition temperature provides another variable for improving the crystal growth. Increasing the temperature increases the rate of desorption and decreases the rate of absorption for equations 6.7-6.10 to occur. When these rates are almost equal, conditions for epitaxy occur and crystal formation occurs without defects. Just above this temperature, the rate of absorption falls lower than the rate of desorption and no deposition is observed. Below this temperature, absorption will happen readily at locations besides the step edges of growths causing defects to occur.

## 5.2 Synthesis and Materials Characterization of HVPE grown GaSbP

Several experiments were performed using the HVPE reactor by keeping certain variables constant. The total reactor pressure was always held at 500 torr. The  $\text{PCl}_3$  bubbler pressure was set to 650 torr and was assumed to be at an average temperature of  $35^\circ\text{C} \pm 5^\circ\text{C}$ . The hydrogen flow during operation was set to 125 sccm and the hydrogen carrier gas flowing through the  $\text{PCl}_3$  bubbler was held at 30 sccm. This temperature was measured during reactor operation utilizing a handheld pyrometer. Reactions were held for 1 hour after gallium reached its operating temperature unless an unforeseen problem arose requiring the reaction to be stopped.

The goal of the initial set of experiments was to find appropriate levels of precursor reaction and deposition temperatures to provide enough precursors and the appropriate temperature to make deposits on the growth substrate. The first conditions used were borrowed mostly from Sudlow et al's HVPE growth of  $\text{GaP}^{114}$ . In these initial experiments, the Sb temperature zone was held at  $600^\circ\text{C}$  and the gallium temperature zone was held at  $800^\circ\text{C}$ . The deposition temperature was set to  $750^\circ\text{C}$ , however, thick clouds of gas and rapid depositions such as those seen in Figure 6.1 formed between the pyrometer and deposition stage so the temperature at this zone may have reached much higher temperatures. These thick clouds and depositions caused the reactor to be shut down prematurely. After the experiments, no deposit was evident at the deposition zone on the Si substrate. Further temperatures were explored before deposits were made at the substrate including  $T_{\text{Sb}}=750^\circ\text{C}$ ,  $T_{\text{Ga}}=970^\circ\text{C}$  and  $T_{\text{Dep}}=900^\circ\text{C}$ . It should be noted that at these higher temperatures, the entirety of the 25 g Sb boat was reacted/evaporated while

only approximately 5 g of Ga were reacted/evaporated. This was obtained by measuring the precursor boats before and after reactor operation.

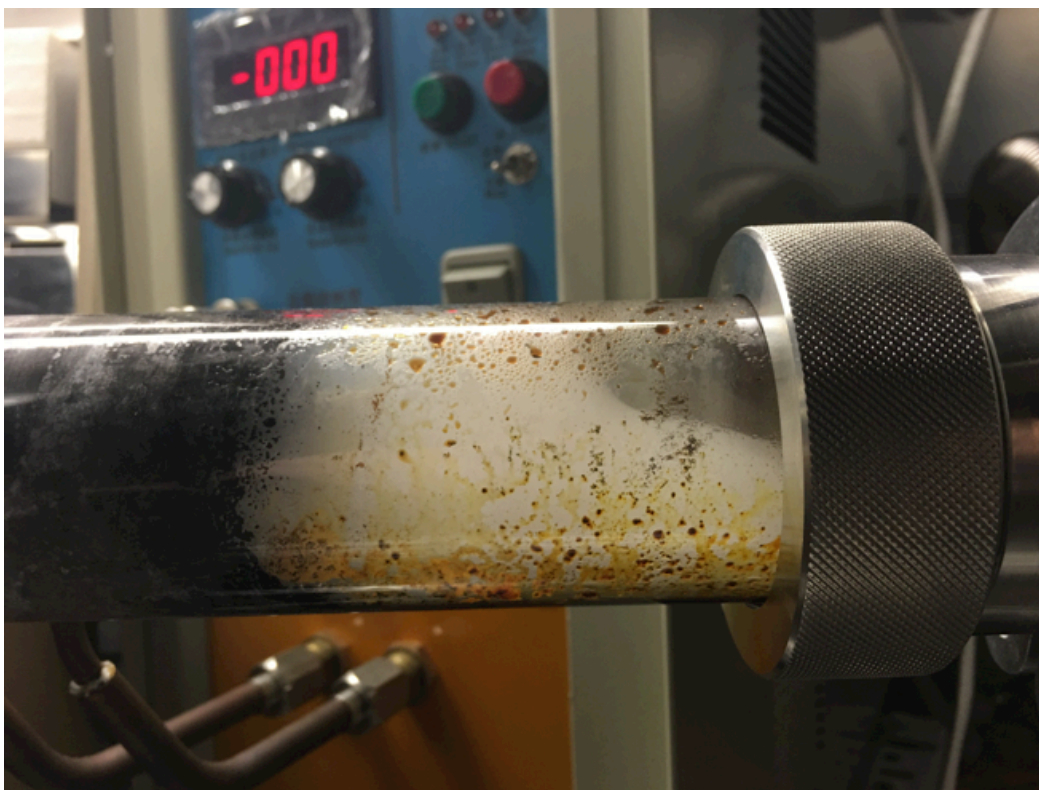


Figure 5.1 Photograph of reactor immediately following the induction heater zone. On the left, black and silver deposition can clearly be seen on the reactor tube, in the middle a thick gas cloud can clearly be seen in the quartz tube.

The experiments are summarized in Table 5.1. The first three experiments did not yield deposits at the Si substrate. In the case of the third experiment, depositions were present on the quartz tube. From this, it was inferred that the temperature at the deposition area was too high to enable GaSbP to deposit on the substrate however deposition was enabled on the quartz tube that was at a lower temperature than the

deposition heater. The deposits present on the tube after the third experiment were

Table 5.1 Summary of conditions used for several HVPE experiments

Sample ID:	T <sub>Sb</sub> (°C)	T <sub>Ga</sub> (°C)	T <sub>Dep</sub> (°C)	H <sub>2</sub> flow (sccm)	Deposit?	Procedural Changes
A1	600	800	750	125	NO	
A2	750	970	900	125	NO	Emergency shutdown
A3	750	970	900	125	TUBE	
A4	650		625	125	YES	
A5	650	970	660	125	NO	LEAK
A6	650	970	660	125	YES	
A7	650	970	700	125	NO	
A8	650	970	620	125	YES	PCl <sub>3</sub> off 1 <sup>st</sup> & first exact distance measurement of substrate heater
A9	650	970	620	125	YES	PCl <sub>3</sub> gradually off
A10	650	970	670	300	YES	Emergency shutdown
A11	650	970	670	125	YES	PCl <sub>3</sub> gradually off
A12	650	870	670	125	YES	PCl <sub>3</sub> gradually off
A13	650	770	670	125	NO	PCl <sub>3</sub> gradually off

collected and characterized. These samples will be referred to as experiment A3

hereafter. From the photographs and scanning electron microscopy images shown in Figure 5.2 it can be seen that 3 different distinct morphologies were grown along this tube growth for experiment A3. In Figure 5.2a, a macroscale photograph shows an orange deposit. In Figure 5.2b, an SEM image showing microwire morphology for resulting materials. Based upon TEM shown in

Figure 5.2c and EDAX analysis, these microwires are highly faceted single crystal GaP with no Sb present and diameters of approximately 1 μm. Figure 5.2d shows a macroscale photograph of the second tube deposit growth area. It is gray in color and under SEM shows a multi-crystalline structure as shown in Figure 5.2e. EDAX shows

that there is approximately 1% Sb in this sample and this is corroborated by XRD shown in Figure 5.3. XRD shows peaks at approximately  $27.8^\circ$  and  $27.9^\circ$  indicating ternary alloy compositions of  $\text{GaSb}_{0.17}\text{P}_{0.83}$  and  $\text{GaSb}_{0.13}\text{P}_{0.87}$  present in the sample. UV-Vis spectroscopy shows that this sample has approximately a 1.7 eV direct band gap and this was corroborated by room temperature photoluminescence as shown in Figure 5.4. Figure 5.2f shows a photograph of the third area of tube deposition. It is black in color and under scanning microscopy shows large tetrahedron-like structures with feature sizes as large as  $100\ \mu\text{m}$ . EDAX of this area shows an Sb composition of approximately 32% of the ternary alloy representing a chemical formula of  $\text{Ga}_3\text{Sb}_2\text{P}$  however the XRD spectrum does not confirm. It is possible that this is indicative of a different material phase with a different crystal lattice than expected for GaSbP however further study of this phenomenon is not within the scope of this study.

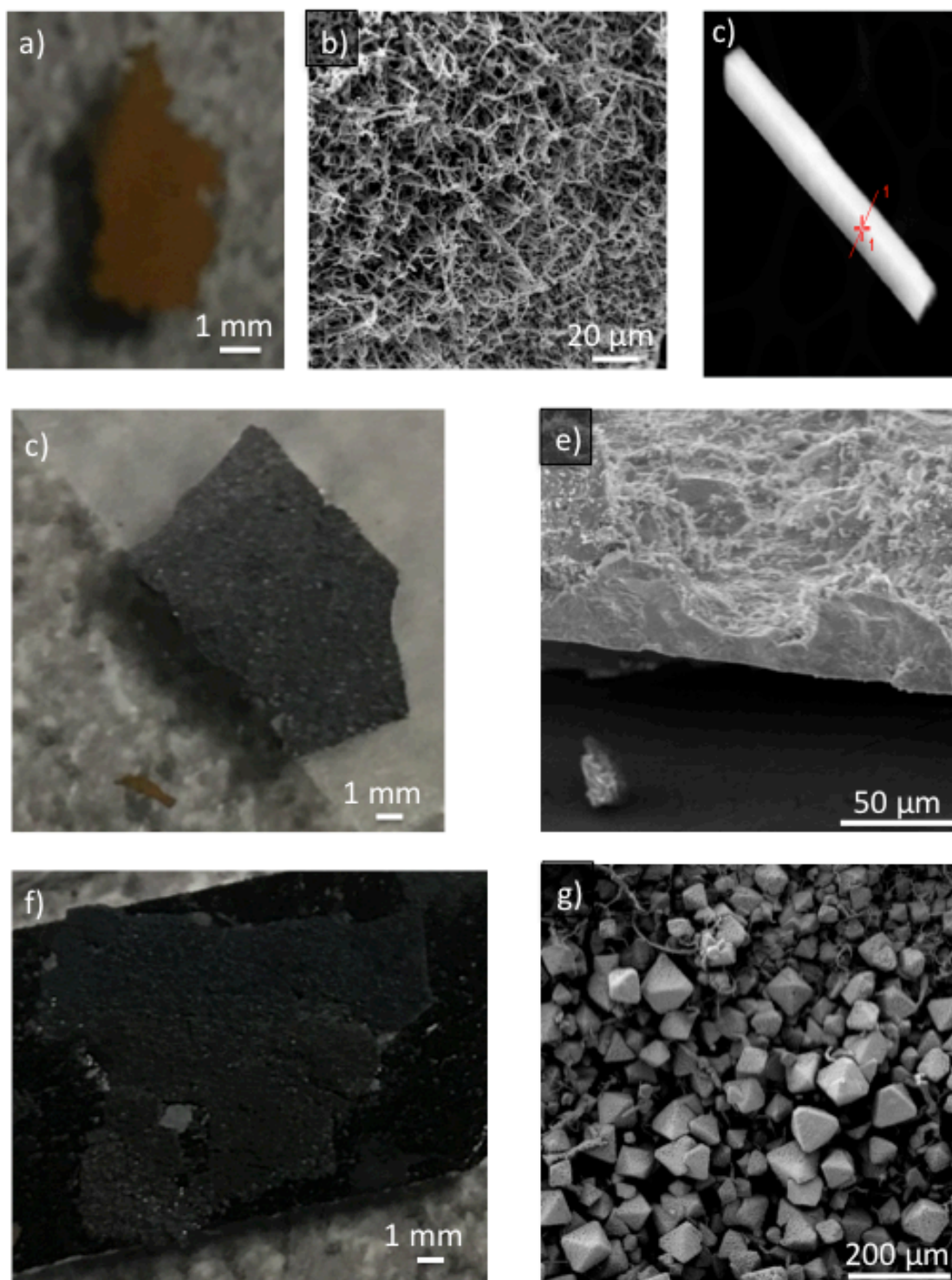


Figure 5.2 – Photography and electron microscopy for sample A3 grown. Sample was collected from quartz tube wall after attempting to deposit GaSbP at  $T_{\text{dep}} = 900^{\circ}\text{C}$ . (a) Photograph, (b) SEM and (c) TEM for A3-orange. (d) Photograph and (e) cross section SEM for A3-gray and (f) photograph and (g) SEM for A3-black.

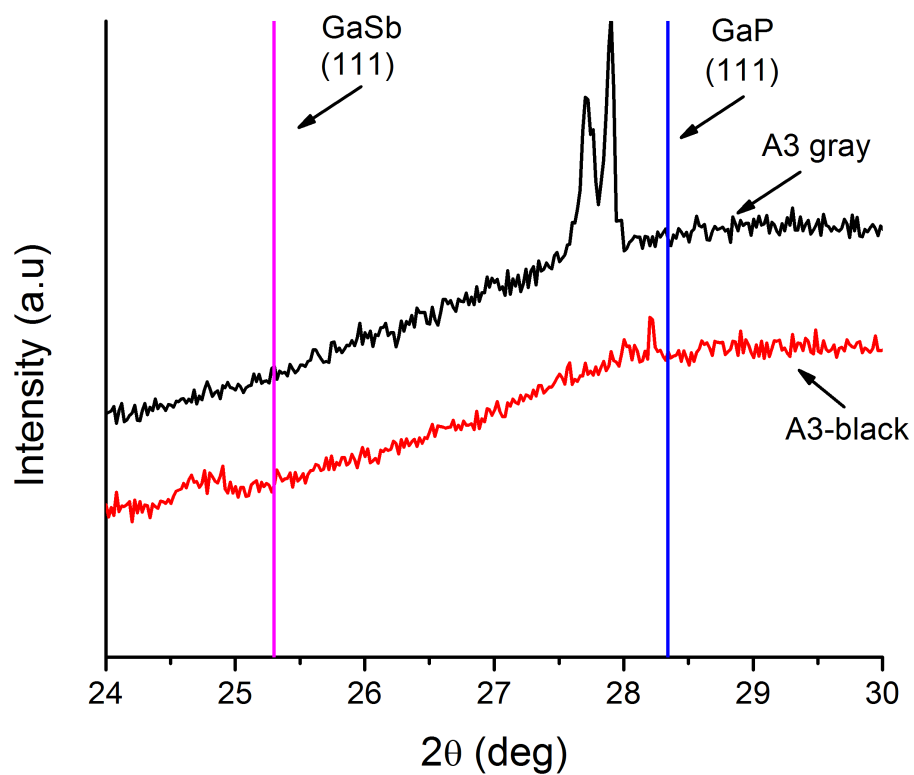


Figure 5.3 XRD pattern for sample A3-gray and A3-black showing the 111-peak region for GaSb and GaP. Peaks can clearly be seen for sample A3-gray at approximately  $27.8^\circ$  and  $27.9^\circ$  that indicate compositions of  $\text{GaSb}_{0.17}\text{P}_{0.83}$  and  $\text{GaSb}_{0.13}\text{P}_{0.87}$  respectively.



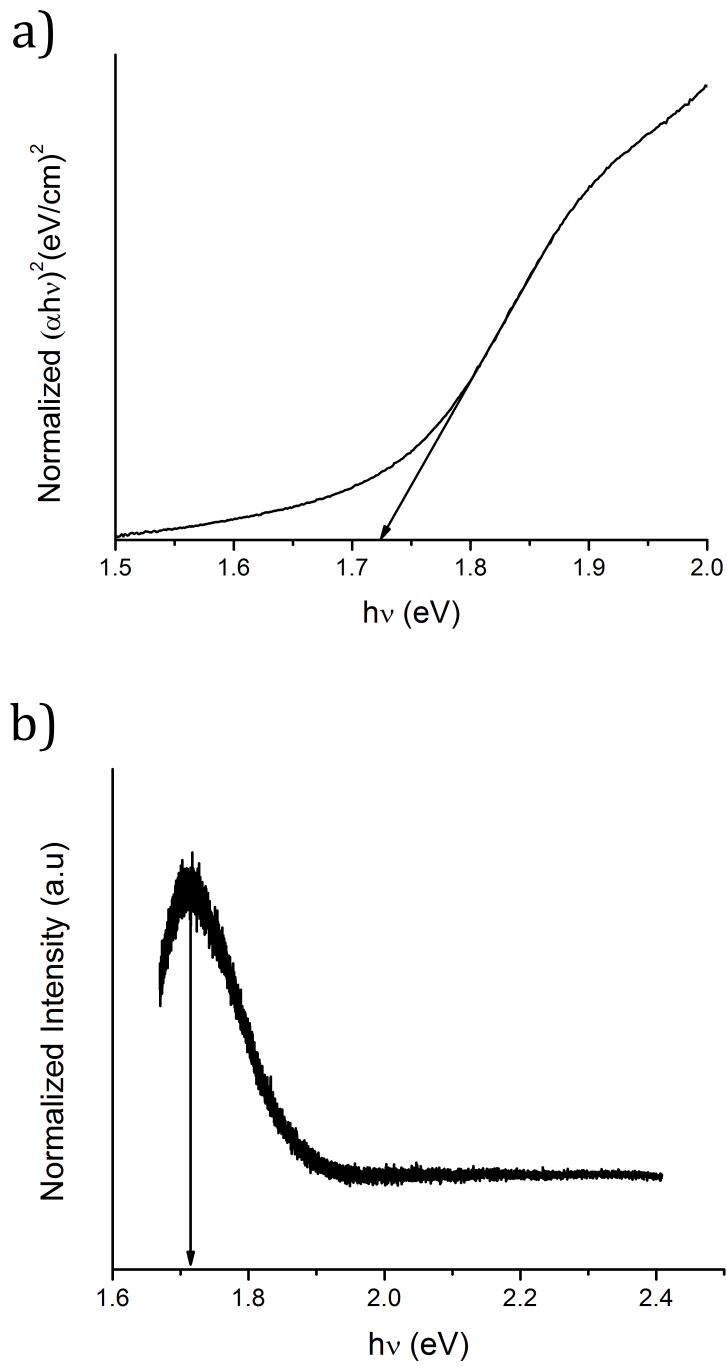


Figure 5.4 Optical band gap properties of sample A3-gray. (a) Tauc plot of the  $n=2$  direct allowed band gap transition indicating a 1.72 eV direct band gap and (b) Photoluminescence spectrum at 77K also indicating a 1.72 eV direct band gap.

In order to keep deposits on the quartz tube from stopping line of sight between the pyrometer and deposition stage, a glass viewport window was installed at the rear of the reaction chamber (as discussed in Chapter 3) and a line of sight was created between the back of the deposition stage and the pyrometer. This drastically improved our ability to maintain temperature at the deposition stage, however it did not fix all of the problems. When a gas cloud is created during reactor operation line of sight between the deposition zone and pyrometer is lost and the infinite process loop ensues.

After this first reconfiguration of the reactor, it was decided to utilize lower deposition temperatures for future experimentation.  $T_{Ga}$  was kept at 970°C,  $T_{Sb}$  was lowered to 650°C and the temperature at the deposition zone was lowered to 625°C. This experiment was successful in making a deposit on our silicon substrate.

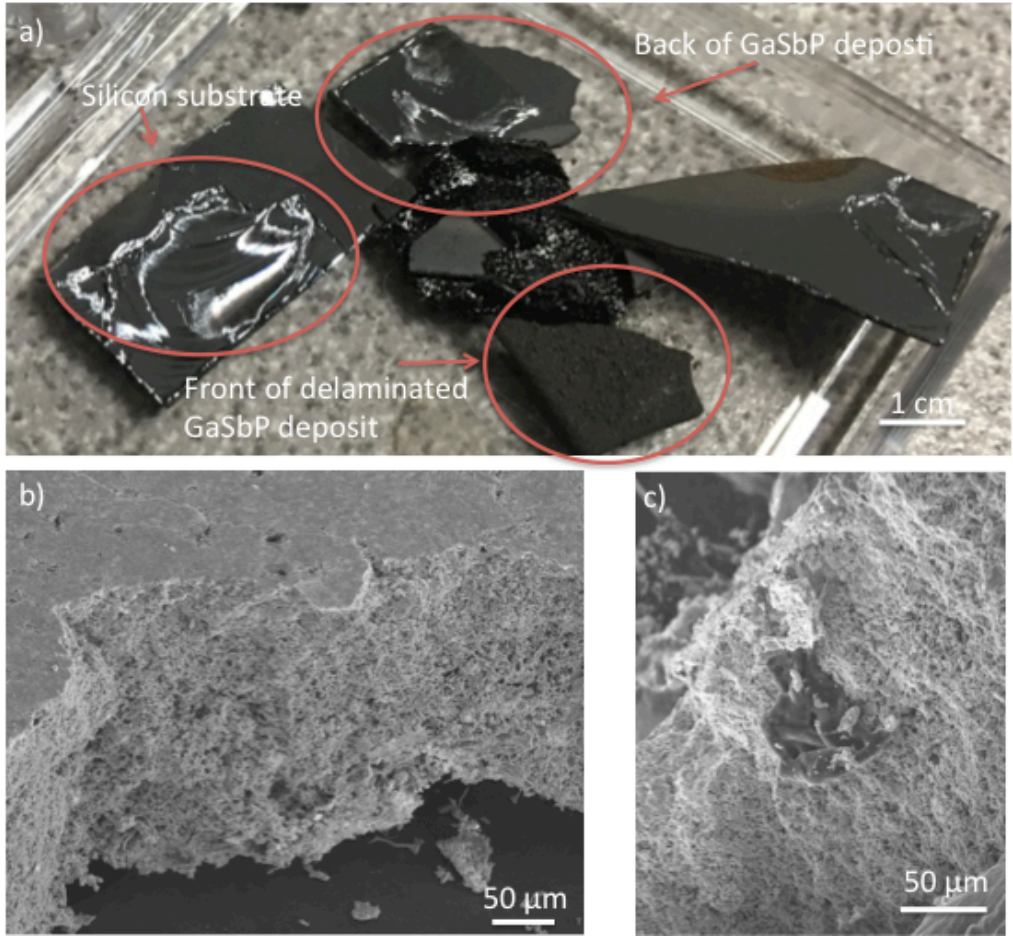


Figure 5.5 (a) Photograph and (b-c) cross section SEM images of sample A4. A thickness of approximately 250 micrometers was observed.

This sample will be referred to hereafter as sample A4. The deposit delaminated from the silicon substrate yielding a freestanding film. Photographs and SEM images of the resulting deposit are shown in Figure 5.5. Photograph shown in Figure 5.5a shows gallium pool on top of the silicon as well as on the back of the GaSbP deposit where the GaSbP film delaminated. The freestanding GaSbP film can also be seen.

As can be seen from the cross section SEM images in 5.5b and 5.5c, the deposit consists of a microwire conglomerate with a thickness of approximately 250

micrometers. EDAX of the deposit shows ratios indicating an incorporation of Sb of 2.5%. EDAX at the bottom of the sample showed that initial growth was primarily gallium with very little Sb or P present. This excess gallium at the growth interface is an indication that the growth mechanism seen in this sample is a vapor liquid solid mechanism and not true epitaxy. At initial growth conditions gallium deposits at the silicon substrate providing a pool for Sb and P precursor dissolution. At a certain solubility threshold, GaSbP crystalizes out of the gallium droplet forming microwire structures. These microwire structures grow together forming the microwire network. This phenomenon is well documented in GaSbN<sup>19</sup>. XRD of the freestanding wafer shows the same signature of GaP as shown in Figure 5.6b. Thus, it is inferred that the Sb present in EDAX is not incorporated as an alloy in sample A4.

A Tauc plot for sample A4 showing the direct allowed transitions from UV-Vis spectroscopy in the diffuse reflectance mode is shown in Figure 5.6a. The Tauc plot indicates a direct band gap of 1.72 eV. Room temperature photoluminescence measurements were performed at five discrete locations on the sample and showed responses ranging from 1.7 eV to 2.2 eV, this is shown next to the 2.26 eV band gap expected for GaP shown in Figure 5.6c.

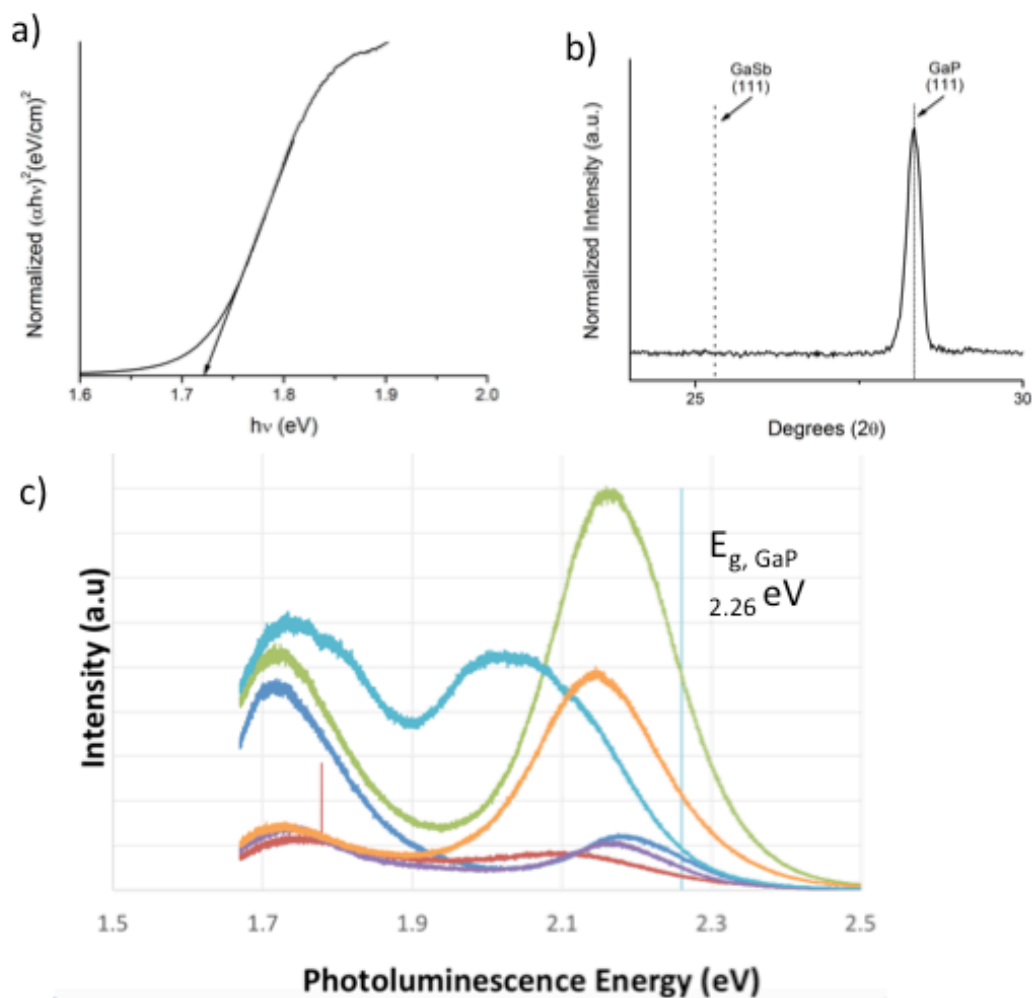


Figure 5.6 Optical and structural characterization of sample A4. (a) Tauc plot for  $n=2$  direct allowed band gap transition indicating a 1.72 eV direct band gap. (b) XRD pattern showing the 111-peak region for GaSb and GaP. A peak is clearly observed at  $28.3^\circ$  indicating the sample is pure GaP. (c) Multiple photoluminescence measurements at different discrete locations on sample A4 indicating several direct band gap responses between 1.72 eV and 2.2 eV.

The goals of the next set of experiments were two-fold. First, initial growth conditions were changed in order to keep Ga from condensing at the substrate. In order

to accomplish this, the deposition heater was heated up under flowing  $H_2$  first before the precursors were turned on. By maintaining the deposition zone at temperature before flowing any precursors, the condensation reaction will be thermodynamically limited and the epitaxial growth of GaSbP will be encouraged. Secondly, in order to improve crystal quality a slightly higher deposition temperature of  $660^\circ\text{C}$  was used. Hereafter this sample will be referred to as sample A6.

A photograph and cross section SEM of A6 is shown in Figure 5.7. The morphology is a microwire array with microwires that have radii of approximately  $5\ \mu\text{m}$ . EDAX of the microwires show that approximately 1.22% Sb incorporation. The EDAX spectrum also shows that there is excess gallium present throughout the sample. This sample did not delaminate from the silicon substrate.

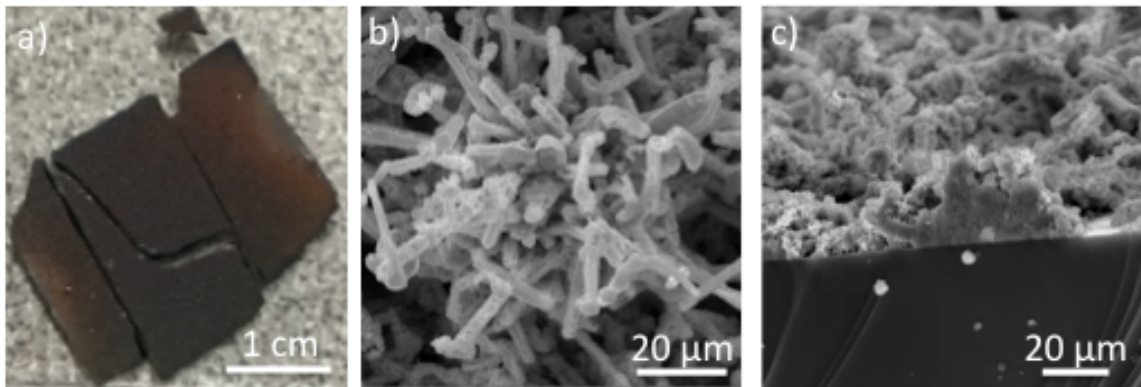


Figure 5.7 (a) Photograph and (b-c) cross section SEM images of sample A6. Faceted microwire geometries are clearly observed with diameters up to  $5\ \mu\text{m}$ .

A tauc plot of the direct allowable transitions for sample A6 is shown in Figure 5.8a indicating a  $1.9\ \text{eV}$  direct band gap. Room temperature photoluminescence

measurements were performed at five discrete locations on the sample A6 that confirm the 1.9 eV response as well as several other responses between 1.7 to 2.0 eV in Figure 5.8b.

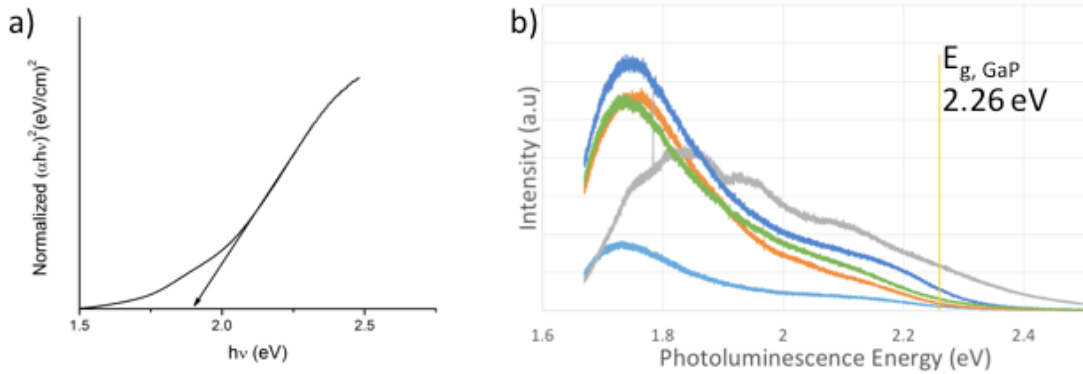


Figure 5.8 (a) Tauc plot for the n=2 direct allowed band gap transition band gap transition for sample A6 indicating a 1.9 eV direct band gap and (b) multiple photoluminescence measurements performed at 77 K at different discrete locations on sample A6 indicating several direct band gap responses between 1.7 eV and 2.2 eV.

XRD data for sample A6 as well as samples A8 through A12 is shown in Figure 5.9. The samples all had XRD peaks between 27.96 and 28.23 degrees indicating GaSbP alloy values of GaSb<sub>.037</sub>P<sub>.963</sub> to GaSb<sub>.127</sub>P<sub>.833</sub> with the exception of A12 that had an identical XRD to GaP. Sample A6 particularly has a peak at 28.23 degrees. This shift in XRD peak away from GaP at 28.34 represents an x of .037 (GaSb<sub>.037</sub>P<sub>.963</sub>). XRD spectra and their ternary alloy composition will be discussed case by case for samples A8-A12.

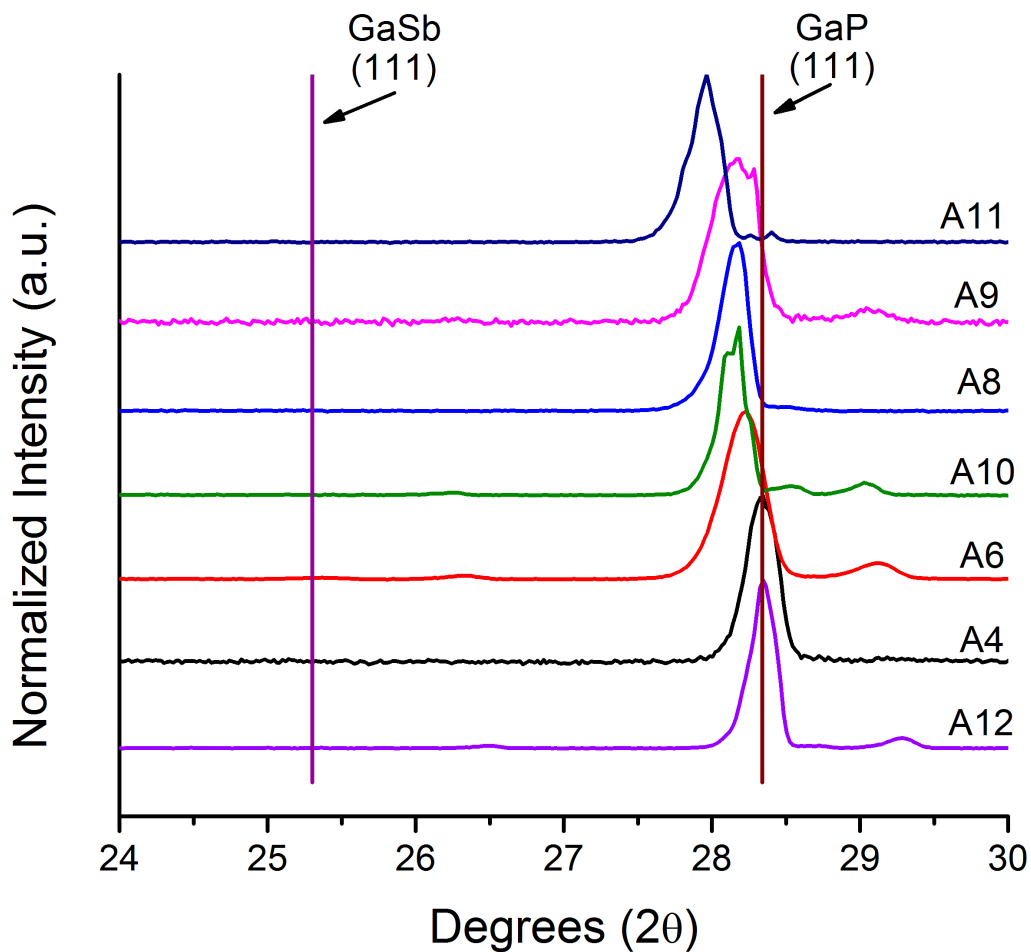


Figure 5.9 Normalized XRD data of the region around the (111) peaks of GaP and GaSb for samples A4 through A12. Peaks are clearly observed from 27.8° up to 28.3° indicating compositions between  $\text{GaSb}_{.037}\text{P}_{.963}$  to  $\text{GaSb}_{.127}\text{P}_{.833}$ . Samples A4 and A12 show XRD peaks identical to GaP.

The change in start-up procedure was successful in limiting the excess pure gallium at the surface but not in completely stopping the microwire growth from occurring and subsequently from improving the crystal quality of the thin film. Growth



temperature seems to be important for growing films. For the first four experiments, the measurement of deposition temperature is not reliable. In the following experiments, the deposition temperature is monitored more accurately and also the shut down procedure is changed to reduce precursors during shut down period. Samples A8 and A9 both utilized the same operating conditions.  $T_{\text{Sb}}$  was set to 650°C,  $T_{\text{Ga}}$  was set to 970°C and  $T_{\text{Dep}}$  was set to 620°C. For the shutdown procedure in sample A8, the phosphorus trichloride precursor was turned off immediately when the reaction was finished and the hydrogen flow was increased to 300 sccm in order to decrease the partial pressure of precursor reactants present during cooldown. The tube furnace was then immediately turned off and the lid cracked to vent heat more rapidly. The deposition stage was kept at the deposition temperature until the precursor temperature zones were both below 100°C. The shutdown procedure for sample A9 was very similar except the only difference was the  $\text{PCl}_3$  was gradually shut off at the same rate in which it was turned on during start-up.

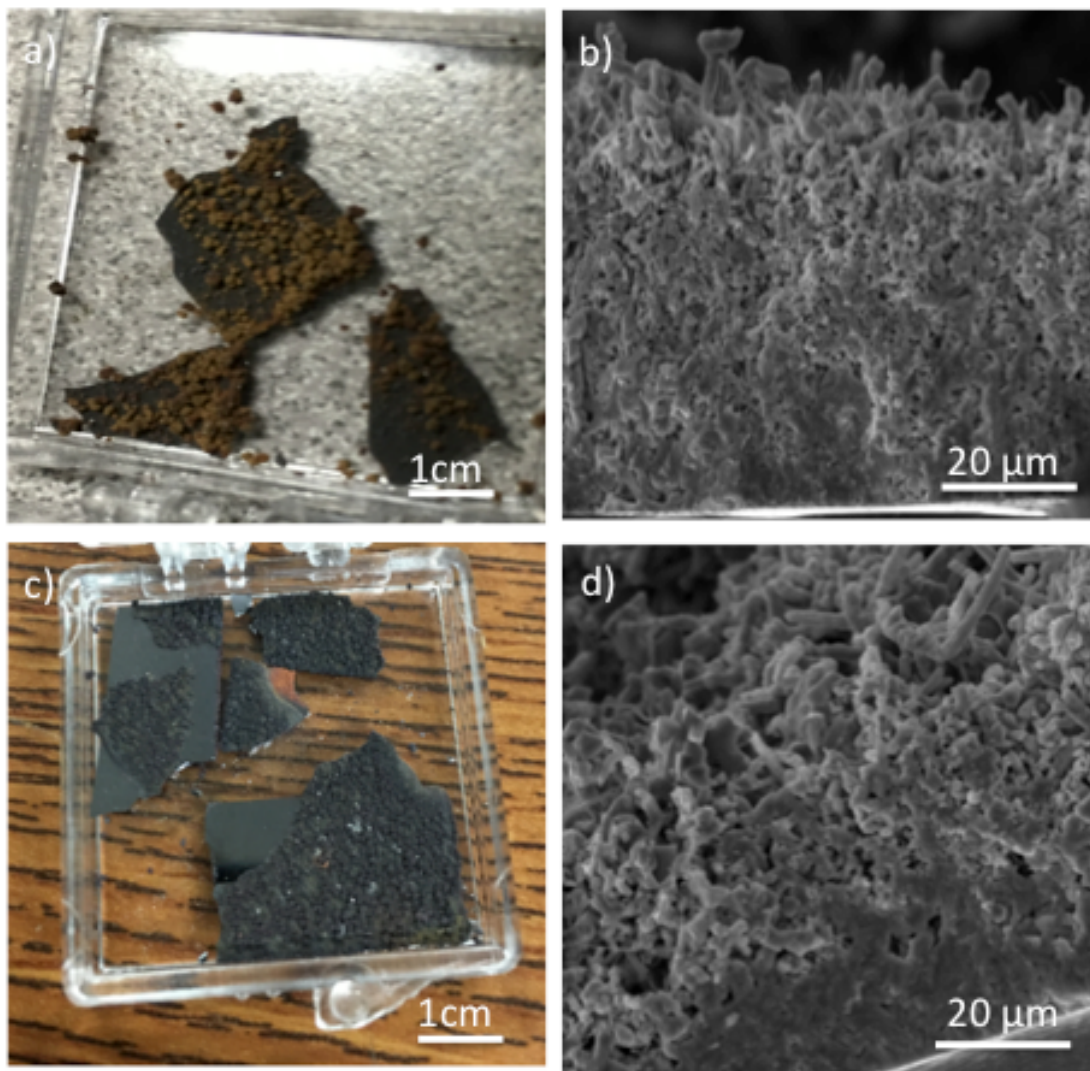


Figure 5.10 (a,c) Photographs and (b,d) cross section SEM images of samples A8 and A9 respectively. Both samples exhibit microwire conglomerate geometries with thicknesses of approximately  $150\ \mu\text{m}$  and more densely packed growth near the growth interface.

Photographs and SEM images of samples A8 and A9 are shown in Figure 5.10. As can be clearly seen in the photographs of each sample, there is a clear difference in the final deposition at the surface when the shutdown procedure is changed. When the phosphorus precursor was shut off first, gallium phosphide nanowires were deposited at

the surface of A8 as shown in Figure 5.10a. These nanowires were easily removed by blowing using compressed air. As evidenced from the cross section SEM images in Figures 5.10b and 5.10d, the growths are very similar in nature. Both samples consist of microwire conglomerates approximately 150  $\mu\text{m}$  thick with more densely packed growth near the growth interface.

Samples A8 and A9 show excellent correlation between XRD and EDAX measurements. EDAX analysis showed that there is 2.49% Sb in A8 and 2.31% Sb in A9 which would indicate alloy compositions of  $\text{GaSb}_{0.05}\text{P}_{0.95}$  and  $\text{GaSb}_{0.046}\text{P}_{0.954}$ . XRD from Figure 5.9 shows a peak for A8 at 28.18 and a peak for A9 at 28.16 indicating alloy compositions of  $\text{GaSb}_{0.053}\text{P}_{0.947}$  and  $\text{GaSb}_{0.06}\text{P}_{0.94}$  by Vegard's law. The Tauc plots in Figures 5.11a and 5.11b for these samples show direct band gaps of between 1.3 and 1.5 eV for A8 and 1.2 and 1.6 eV for A9. Photoluminescence in Figures 5.11c and 5.11d show ranges of responses for both materials similar to previous samples, all peaks are less than 2.26 eV, indicating the response is from GaSbP and not GaP.

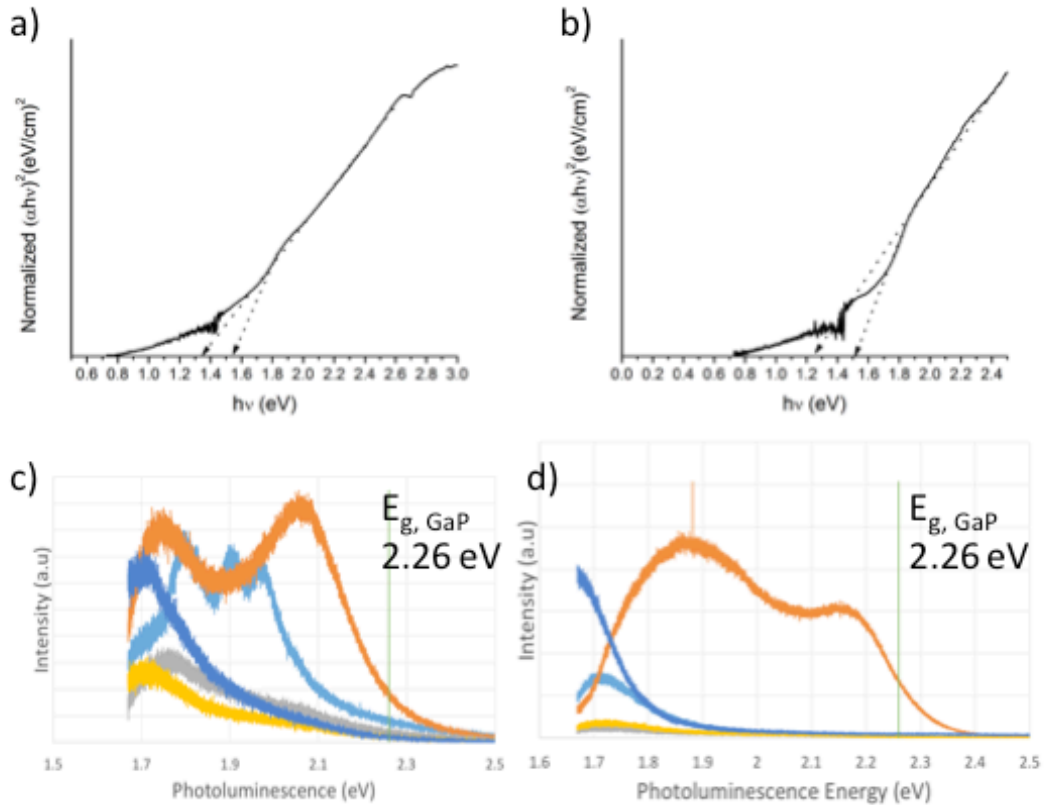


Figure 5.11 Optical measurements for samples A8 and A9. (a,b) Tauc plots for the  $n=2$  direct allowed band gap transition for samples A8 and A9, respectively, indicating a 1.3 eV and 1.5 eV direct band gaps for sample A8 and 1.2 eV to 1.6 eV direct band gaps for sample A9. (c,d) Multiple photoluminescence measurements performed at 77 K at different discrete locations on samples A8 and A9, respectively, indicating several direct band gap responses between 1.7 eV and 2.2 eV in each sample.

For samples, A10 and A11, the same operating conditions were used as in A8 and A9 except the deposition temperature was increased to 670°C. A10 had to be abruptly shutdown immediately after completing the reaction due to a gas cloud that caused deposition on the viewport and complete loss of sight between the pyrometer substrate

heater. Furthermore, the H<sub>2</sub> flow was inadvertently left at 300 sccm during operation for A10. Sample A11 was shutdown in the same manner as A9.

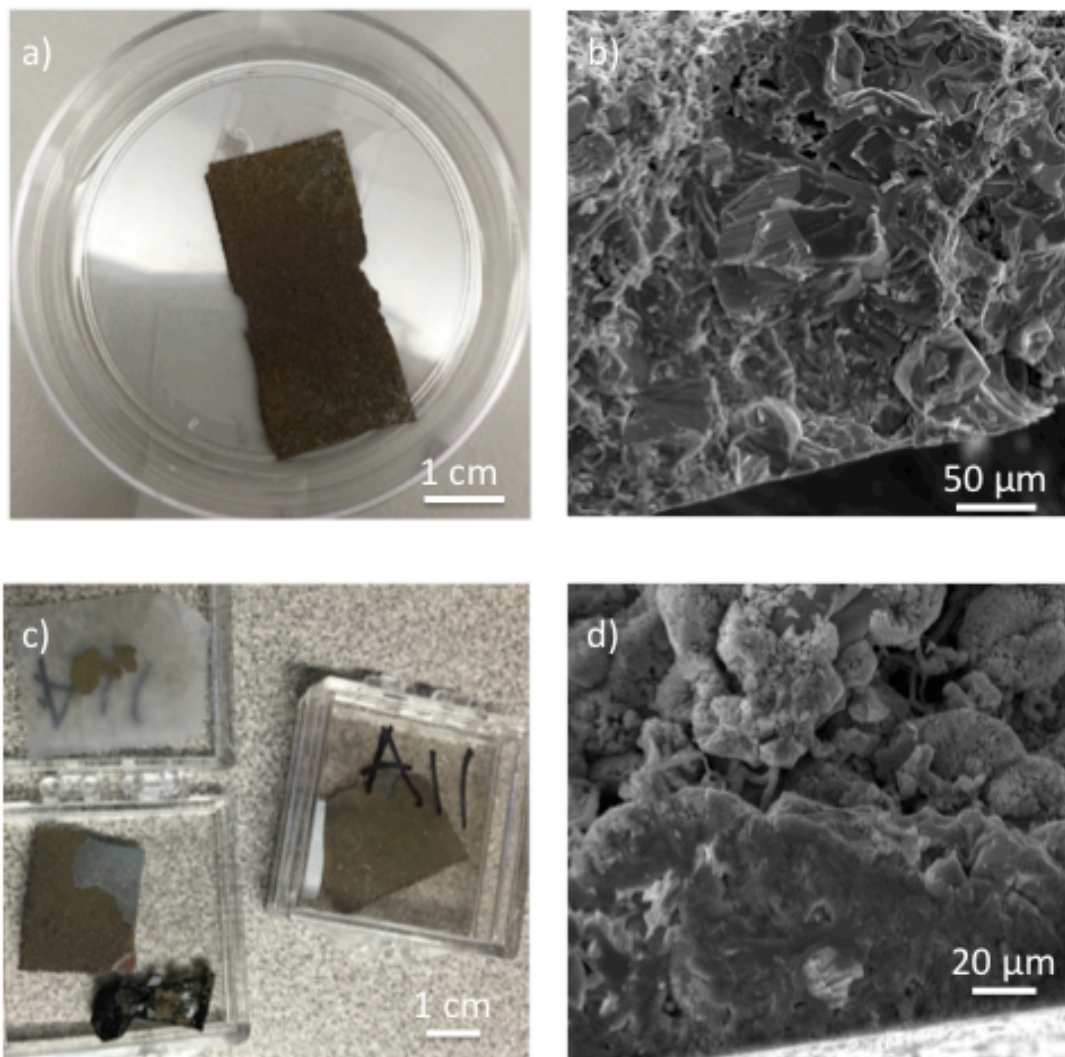


Figure 5.12 – (a,c) Photographs and (b,d) cross section SEM images of samples A10 and A11 respectively. Both samples exhibit microwire conglomerate geometries with thicknesses of approximately 200 μm and highly oriented crystallinity with boulder-like features in excess of 10 μm.

Photographs and SEM images of samples A10 and A11 are shown in Figure 6.12. As shown in Figure 5.12b, near the growth interface, boulder-like features are clearly observed with crystals in excess of 10  $\mu\text{m}$ . The total sample thickness is approximately 200  $\mu\text{m}$ . As the sample nears the growth surface, a clear morphological change is seen as the growth begins to change into a microwire growth. EDAX of sample A10 shows that it contains 8.05% Sb. In Figure 5.12d, the SEM image for A11 is shown. It also shows a compact crystalline growth but with smaller feature sizes than A10. EDAX of A11 shows that it has approximately 2.77% Sb representing an alloy composition of  $\text{GaSb}_{0.54}\text{P}_{0.946}$ .

Tauc plots of the direct allowable transitions for samples A10 and A11 are shown in Figures 5.13a and 5.13b. They clearly show direct band gaps of 2.1 eV for A10 and 2.1 eV for A11. Figure R9 shows the XRD of samples A10 and A11 with peaks at 28.18 and 27.96 degrees indicating alloy compositions of  $\text{GaSb}_{0.53}\text{P}_{0.947}$  and  $\text{GaSb}_{0.127}\text{P}_{0.873}$  respectively. Figure 5.13c and 5.13d shows photoluminescence of samples A10 and A11. Peaks are observed between 1.7 eV and 2.2 eV for each sample.

In samples A8-A11, EDAX also consistently showed small amounts of oxygen and aluminum. This was most likely due to the insulators used to help secure the silicon at the deposition zone. In sample A12 these insulators were replaced with machined graphite holders. The presence of aluminum and oxygen were not detected in EDAX analysis.

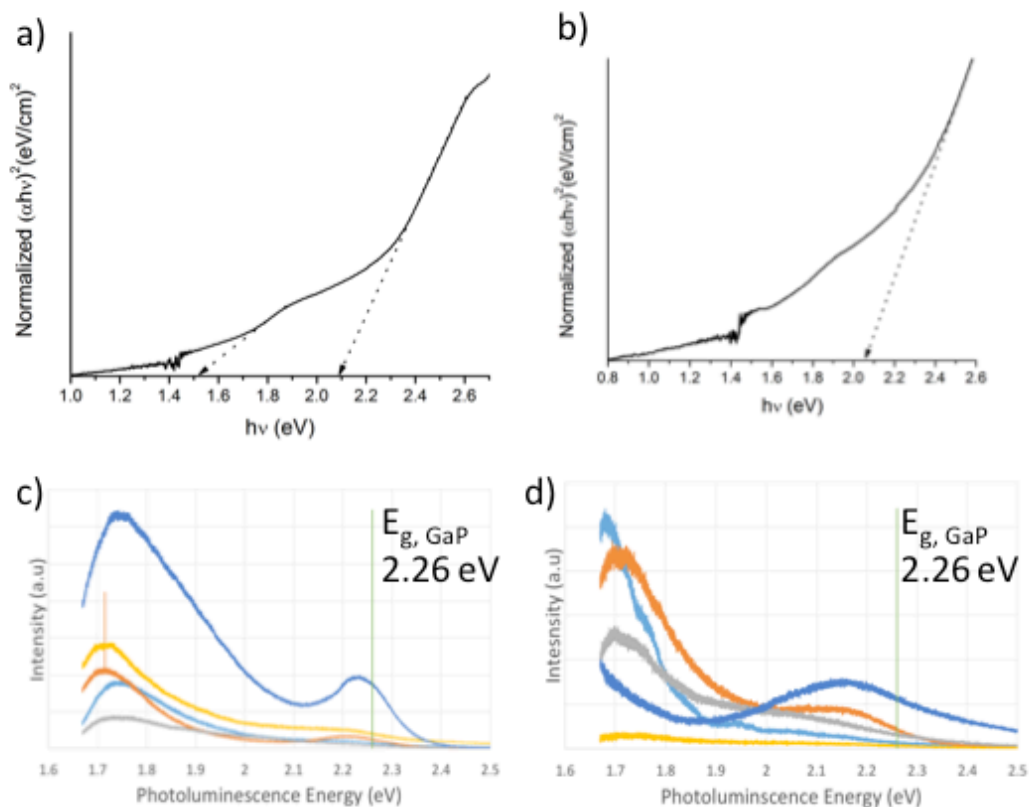


Figure 5.13 Optical measurements for samples A10 and A11. (a,b) Tauc plots for the  $n=2$  direct allowed band gap transition for samples A10 and A11, respectively, indicating a 1.3 eV and 1.5 eV direct band gaps for sample A8 and 1.2 eV to 1.6 eV direct band gaps for sample A9. (c,d) Multiple photoluminescence measurements performed at 77 K at different discrete locations on samples A10 and A11, respectively, indicating several direct band gap responses between 1.7 eV and 2.2 eV in each sample.

Analysis of reactant flow during HVPE: One of the major factors in these experiments has been the excess production of gas phase precursors, primarily GaCl that results in not only growth issues but operational, maintenance and safety issues as well. When possible, Ga and Sb precursor boats were weighed before and after experiments in order to determine the mass of precursors that reacted during the experiment. Conversion of

these masses to moles of desirable reactants will serve to show the amount of moles available for reaction during the experiment. By tuning these molar flow rates, precise compositional control can be achieved in future experiments.

At 970°C, the Ga boat lost approximately 5.5 g of mass and at 650°C the Sb boat lost an average of 3.0 g of mass during a 1 hour experiment. This experiment also includes 30-35 minutes of temperature ramp to get to the precursor zones to operating conditions and approximately 1 hour of precursor cooldown time after the experiment where precursors could still be being generated. Utilizing the atomic masses of Ga (69.7 g/mol) and Sb (121.8 g/mol), it can be seen that 78.9 mmol of Ga and 24.6 mmol of Sb are generated over the course of a single experiment at these temperatures. The amount of moles of phosphorus provided by the carrier gas flowing through the  $\text{PCl}_3$  bubbler can also be estimated. Utilizing the JANAF thermochemical data for  $\text{PCl}_3$ , the partial pressure of  $\text{PCl}_3$  in the gas phase ready to be transported by the carrier gas can be known. Based upon a bubbler pressure of 650 torr, average bubbler temperature of 35°C and 30 sccm of  $\text{H}_2$  carrier gas flowing through the bubbler for an operating time of 1 hour, between 27.8 and 37.1 mmol of P are provided for reaction during a 1-hour experiment.

There are about 78.9 mmol of group III column precursors compared to at most 61.7 mmol of group V precursors and serves to clearly explain the observation of excess GaCl being generated. Future experiments should focus on lowering the amount of GaCl generated tremendously. MOCVD and MBE III-V growths have required as little as 7:3 ratio of group V precursors to group III precursors and in some cases in excess of 40:1 the amount of group V precursors as group III precursors. In these two cases, if Sb and  $\text{PCl}_3$  conditions are kept the same, as little as 1.5 mmol of Ga or as much as 26.4 mmol



would be required to limit the excess Ga, representing almost a two order of magnitude decrease in generation of GaCl.

The primary goal of the final experiment set was to lower the amount of available GaCl available for reaction so that excess gallium conditions would not be present and hopefully an improvement in crystallinity is observed. In order to accomplish this goal, temperatures of 870°C and 770°C were used in the gallium temperature zone. This is 100°C and 200°C below the 970°C used in previous experiments. The temperatures chosen for the antimony and deposition zones for this set of experiments is the same as that used for samples A10 and A11 of 670°C, this is because these samples showed the highest quality crystallinity. The resulting deposit using  $T_{\text{Ga}}$  of 870°C will be referred to here-after as A12. No deposit was observed when using  $T_{\text{Ga}}$  of 770°C. Unfortunately,

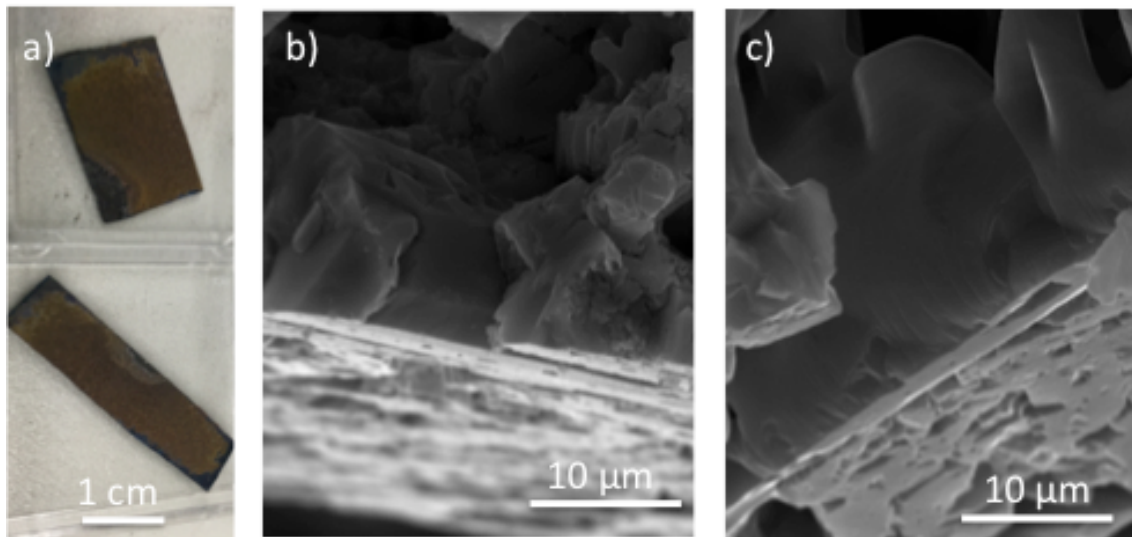


FIGURE 5.14 (a) Photograph and (b,c) cross section SEM images of sample A12.

The sample exhibits single crystal features in excess of 30  $\mu\text{m}$  and displays clear evidence of epitaxial growth at the growth interface. The marks perpendicular to the growth interface where the crystal was cleaved are another clear sign of the single crystallinity exhibited.

operational circumstances kept mass measurements from being taken on the Sb and Ga precursor boats and the mass of precursor lost at these temperatures is unknown.

A photograph and SEM images of sample A12 are shown in Figure 5.14. As can be seen, the growth thickness is not nearly as thick as samples A10 and A11, measuring approximately 50  $\mu\text{m}$ . The SEM cross section images shown in Figures 5.14c and 5.14d clearly show that the epitaxial growth has been achieved. The cleave marks observed in Figure 5.13d are clear indication of the single crystalline nature of the film. EDAX of the sample show an approximate Sb incorporation of 1.27% Sb representing a composition of  $\text{GaSb}_{.026}\text{P}_{.974}$ . Furthermore, neither  $\text{O}_2$  nor Al peaks were observed in EDAX, indicating that replacing the insulators used to hold the samples to the substrate heater with graphite holders remedied these impurities.

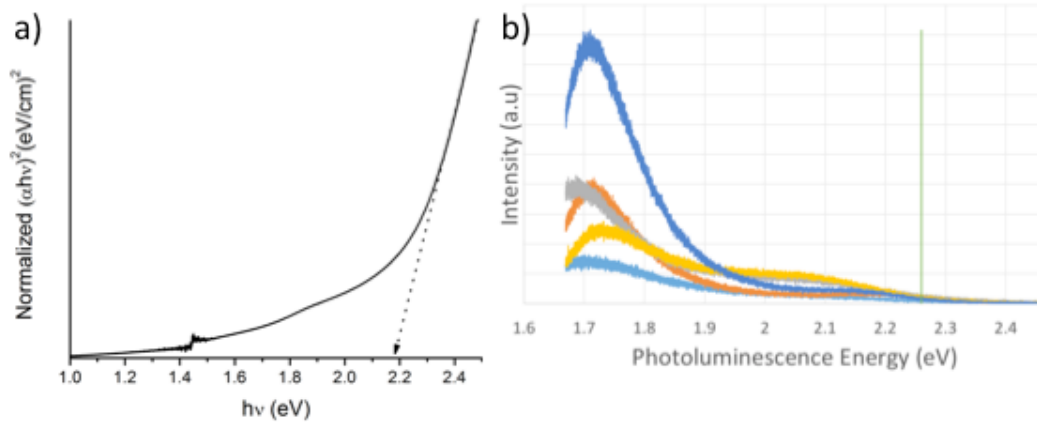


Figure 5.15 Optical measurements for sample A12. (a) Tauc plot for the  $n=2$  direct allowed band gap transition for samples A12 indicating a 2.15 eV direct band gap. (b) Multiple photoluminescence measurements performed at 77 K at different discrete locations on samples A12 indicating several direct band gap responses between 1.7 eV and 2.15 eV.

A Tauc plot of sample A12 indicates a direct band gap of 2.15eV shown in Figure 5.15a. XRD of the sample showed nearly identical peaks to GaP indicating an incorporation of 0% Sb. It is possible that the incorporation of less than 1% Sb would be difficult to observe in XRD however and the indication of direct band gap and high quality crystallinity with 1% Sb in EDAX lends itself to the hypothesis that ternary GaSbP with a formula close to  $\text{GaSb}_{.026}\text{P}_{.974}$  was formed. Room-temperature photoluminescence measurements showed peaks mostly centered around 1.7 eV but some less intense peaks all the way up to 2.15 eV in Figure 6.15b.

Table 5.2 Summary of structural and optical properties of relevant  $\text{GaSb}_x\text{P}_{1-x}$  films A4 through A12 as a function of deposition temperature including general morphology type, elemental compositions from EDS, alloy composition from XRD and measurements of direct band gaps from Tauc plots from UV-VIS diffuse reflectance and photoluminescence measurements performed at 77 K.

	<b>Deposition Temperature (°C)</b>	<b>Morphology</b>	<b>EDS (xSb)</b>	<b>XRD (xSb)</b>	<b>UV-VIS (eV)</b>	<b>PL (eV)</b>
A4	625	Microwire	.05	0	1.72	1.7-2.2
A6	660	Microwire	.024	.037	1.9	1.7-2.0
A8	620	Microwire	.05	.053	1.3-1.5	1.7-2.2
A9	620	Microwire	.046	.06	1.2-1.6	1.7-2.2
A10	670	Microwire/Highly Oriented Crystal	.16	.053	2.1	1.7-2.2
A11	670	Microwire/Highly Oriented Crystal	.054	.127	2.1	1.7-2.2
A12	670	Microwire/Single Crystal	.026	0	2.15	1.7

**Processing-Property Relationships:** As can be seen from Table 5.2 below, a clear improvement in crystal growth occurred with controlling Ga/P precursor ratio and adjustment of deposition temperature. Initial experiments (A4 and A5) exhibited microwire conglomerate geometries with different microwire packing densities. EDAX clearly shows that there is Sb present in the growths with ternary alloy compositions of  $\text{GaSb}_{.024}\text{P}_{.976}$  to  $\text{GaSb}_{.16}\text{P}_{.84}$ . XRD measurements for samples from experiments labeled A6 to A11 confirm that the observed growth resulted in ternary GaSbP films with compositions between  $\text{GaSb}_{.037}\text{P}_{.963}$  and  $\text{GaSb}_{.127}\text{P}_{.873}$ . The XRD of samples A4 and A12 suggest that antimony may not be incorporated into the alloy. UV-Vis confirmed direct band gaps in all of the samples with values from 1.2 eV up to 2.15 eV. Photoluminescence corroborated these UV-Vis measurements but also showed other energies between 1.7 eV to 2.2 eV for each sample.

The high quality crystal growth shown in samples A10-A12 is a tremendous step forward toward large-scale epilayers of GaSbP being grown. There is no doubt that with a reconfiguration of the reactor and a rigorous design of experiments that in short time this process will be capable of generating freestanding wafers of single crystal GaSbP.

### 5.3 Photoelectrochemical testing of HVPE grown GaSbP

Photoelectrochemical characterization for samples A4, A6 and A8 through A12 are presented here. Three electrode linear sweep voltammetry and open-circuit potential (OCP) under saturated illumination conditions were performed for each sample. When

photo-response was good enough, two electrode chronoamperometry under unbiased conditions was performed. The results from these GaSbP alloys are extremely promising and have potential to open up an entire field of research in the PEC water splitting community.

Photoelectrochemical characterization on samples A4 and A6 serve as a preliminary look into the behavior observed thus far in HVPE grown GaSbP films. Three-electrode linear sweep voltammetry (LSV) and open circuit potential testing for sample A4 is shown in Figures 5.16a and 5.16b respectively at a concentrated illumination of 4 suns in sodium sulfate solution with  $\text{pH} = 9$ . Unexpectedly, OCP shows a negative step in voltage upon illumination indicating an n-type behavior. This is contrary to previous results from plasma transport experiments that exhibited p-type conductivity. This phenomenon is seen in all HVPE grown samples tested thus far. The source of n-type doping in HVPE is not known and needs to be investigated further. I-V analysis further corroborated with the highest photoactivity of  $0.5 \text{ mA/cm}^2$  being generated at OER potentials. A high background current is also observed in the dark. This could be due to electrolyte migrating through the microwire network to exposed electrical contact at where the microwire mesh is contacted. If these microwire geometries are utilized in the future, the background dark current needs to be reduced by passivating high surface area.

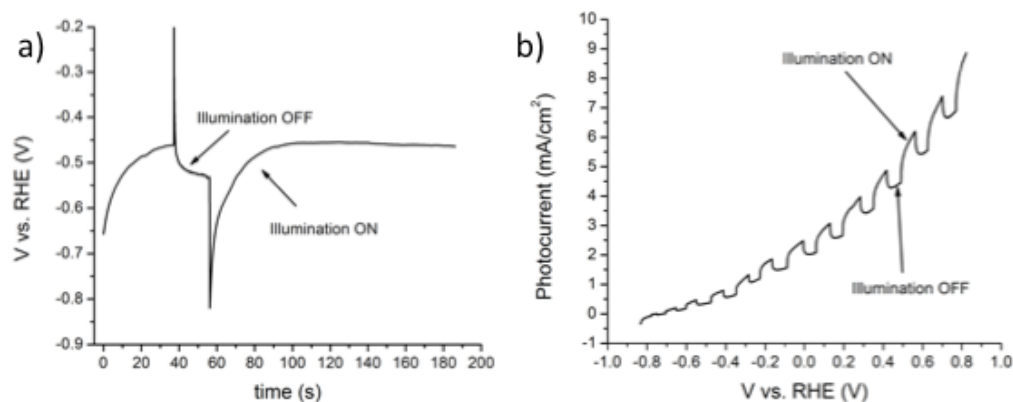


Figure 5.16 – Fundamental PEC studies of sample A4 at 4 suns illumination in sodium sulfate solution (pH = 9). (a) OCP under chopped illumination for 200 seconds indicating n-type conductivity and (b) chopped illumination LSV measurements exhibiting approximately  $.5 \text{ mA/cm}^2$  photoactivity under bias and high background currents in the dark.

A previously mentioned, sample A6 did not delaminate from the silicon substrate. As such, two different electrodes for sample A6 were prepared. One electrode was fabricated in the same manner as all other electrodes, by making an InGa eutectic contact to the back of the sample, in this case the Si substrate that growth occurred on, causing generated carriers to flow through this GaSbP/Si junction. A second sample was fabricated by making an InGa contact to the top of the GaSbP microwire film instead of on the back of the Si. If the film is conductive enough, generated carriers will flow directly to the InGa contact and bypass the Si altogether. This was done in order to see if there is any observed benefit to having this built in junction to Si junction. In the design phase for HVPE experimentation, p-type silicon was chosen as the deposition substrate of choice because it was believed that the GaSbP growth would also be p-type. With HVPE

GaSbP showing n-type conductivity, this creates a built-in p-n junction into the cell. The junction is in the wrong direction to provide extra bias for water splitting however and should cause a site of major recombination within the electrode.

OCP and IV measurements are shown in Figures 5.17a and 5.17b respectively for the bottom contacted A6 sample and 5.17c and 5.17d for the top contacted A6 sample. Contrary to what is expected, the bottom contacted sample both showed a higher photovoltage in OCP and a higher photoactivity in IV testing. This could be due to poor conductivity in the top contacted film however. Further study of this phenomenon is warranted in future experimentation, however investigating this type of p-n junction further is not within the scope of this study.

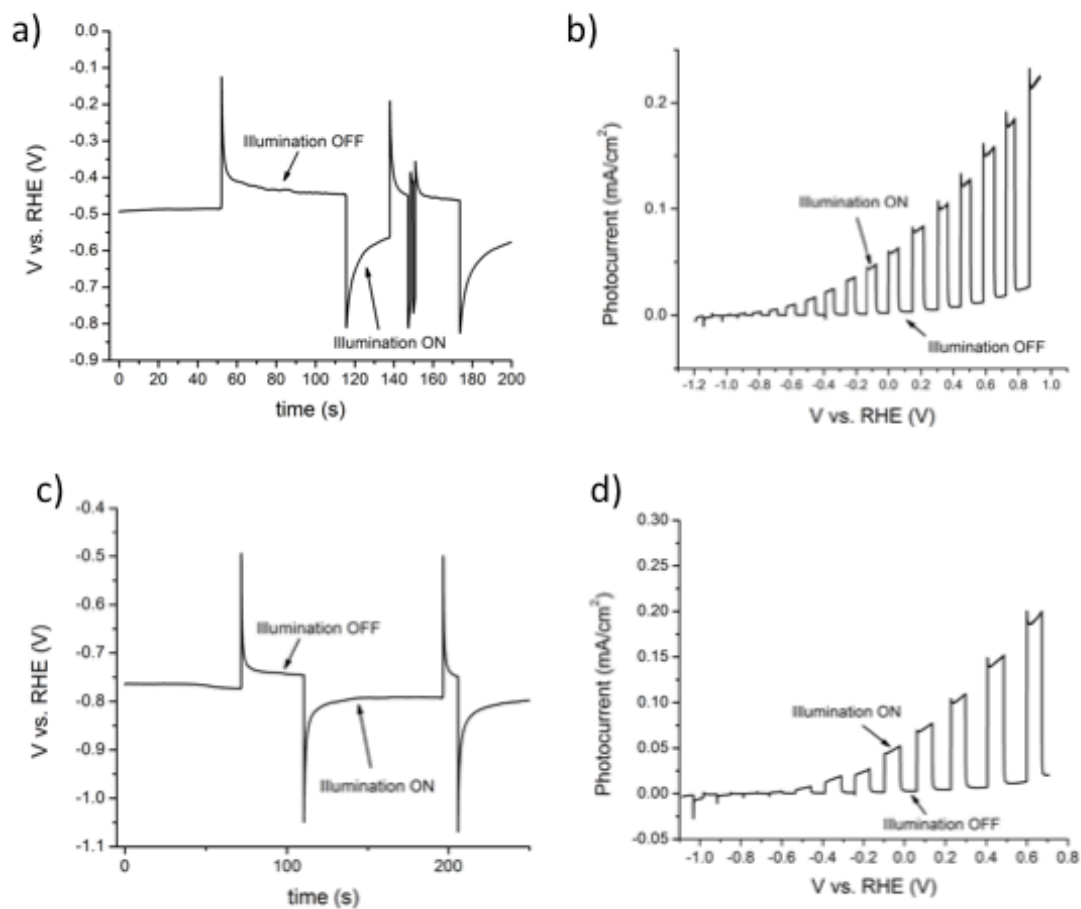


Figure 5.17 Fundamental PEC studies for samples A6 with bottom and top contacts, respectively, at 4 suns illumination in sodium sulfate solution (pH = 10). (a,c) OCP under chopped illumination for 200+ seconds indicating n-type conductivity for both samples and (b,d) chopped illumination LSV measurements exhibiting approximately 0.2 mA/cm<sup>2</sup> and 0.15 mA/cm<sup>2</sup> maximum photocurrents under bias respectively.

OCP and IV measurements at 4 suns illumination were also performed for sample A8 and A9 which were grown under the same conditions except for a change in the



shutdown procedure. The OCP measurement from sample A8 in Figure 5.18a indicates an n-type conductivity and sizable photovoltage response of .7 V. This is an incredibly promising result as large photovoltages are a sign of a highly photoactive material. LSV measurements for sample A8 are shown in Figure 5.18b. The sample has a photoactivity

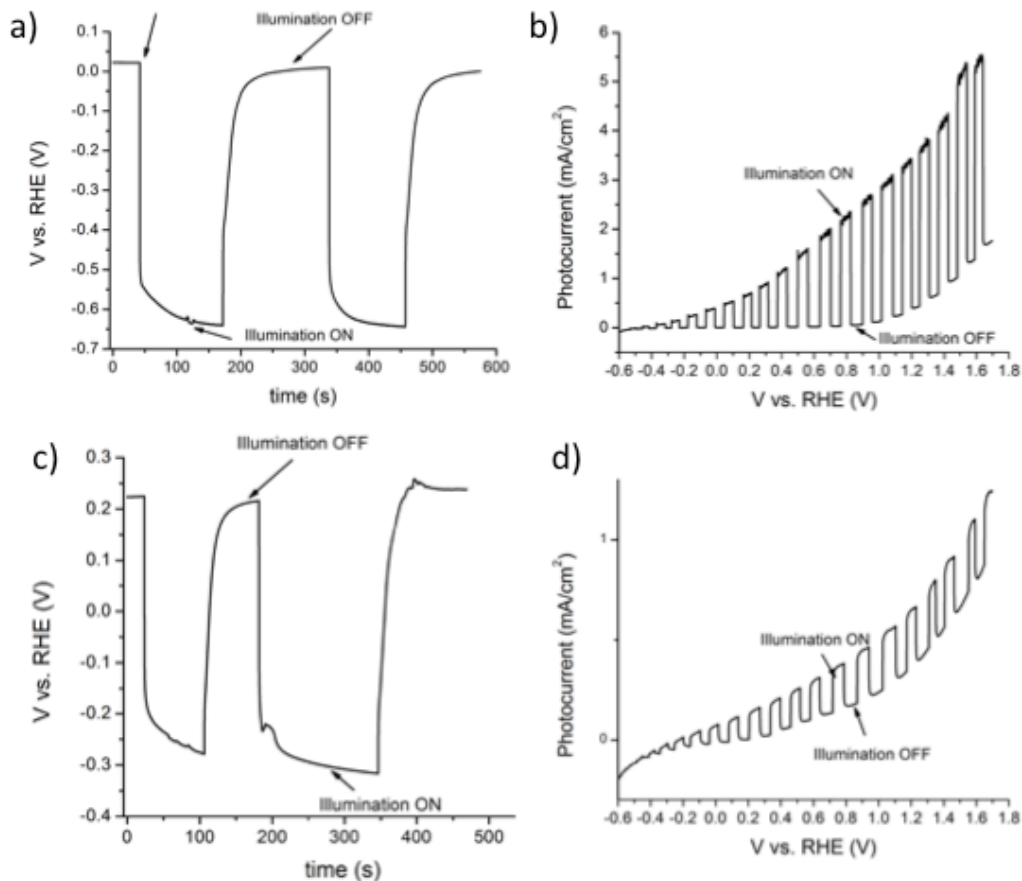


Figure 5.18 Fundamental PEC studies for samples A8 and A9, respectively, at 4 suns illumination in 3M sulfuric acid (pH = 0). (a,c) OCP under chopped illumination for 500+ seconds indicating n-type conductivity for both samples and (b,d) chopped illumination LSV measurements exhibiting approximately 3 mA/cm<sup>2</sup> and 0.2 mA/cm<sup>2</sup> maximum photocurrents under bias respectively.

of approximately  $1.5 \text{ mA/cm}^2$  at  $0 \text{ V}$  vs RHE and a maximum of  $3 \text{ mA/cm}^2$  before the onset of dark current. PEC results for sample A9 are also promising, but did not perform as well as sample A8. Figure 5.18c shows the OCP for sample A9. Again, n-type behavior and a high photovoltage of  $.5 \text{ V}$  was observed. IV measurements were quite poor however showing less than  $.1 \text{ mA/cm}^2$  even at  $1 \text{ V}$  vs RHE shown in Figure 5.18d.

Samples A10 and A11 were also grown under almost the same conditions. In this case however, the  $\text{H}_2$  flow rate of A10 was inadvertently left at  $300 \text{ sccm}$  instead of  $125 \text{ sccm}$ . There were also major complications during shutdown causing an abrupt shutdown of the reactor. These factors seem to have yielded beneficial results, however, as sample A10 is the best performing PEC sample in this study. As can be seen in Figure 5.19a, OCP for sample A10 has an excellent photovoltage of  $.75 \text{ V}$ , the highest observed in this study. IV measurements yielded an incredible  $8 \text{ mA/cm}^2$  photocurrent at  $0 \text{ V}$  vs. RHE and a saturated photoactivity of  $11 \text{ mA/cm}^2$  before the onset of dark current as shown in Figure 5.19b. Chopped illumination 2-electrode chronoamperometry further confirmed this behavior under unbiased conditions as showing Figure 5.19c. Over the course of 10 minutes, photocurrents between  $5$  and  $8 \text{ mA/cm}^2$  were observed with no external bias. Sample A11 on the other hand, showed very poor performance in comparison to A10. OCP measurements shown in Figure 5.19d show that n-type behavior with only  $.35 \text{ V}$  photovoltage is observed. IV measurements yielded photocurrents less than  $50 \text{ }\mu\text{A/cm}^2$  even under external bias as shown in Figure 5.19e. In the case of samples A8-A11, it seems that shutting off the  $\text{PCl}_3$  immediately after operation of the reactor rather than gradually provides superior PEC properties.

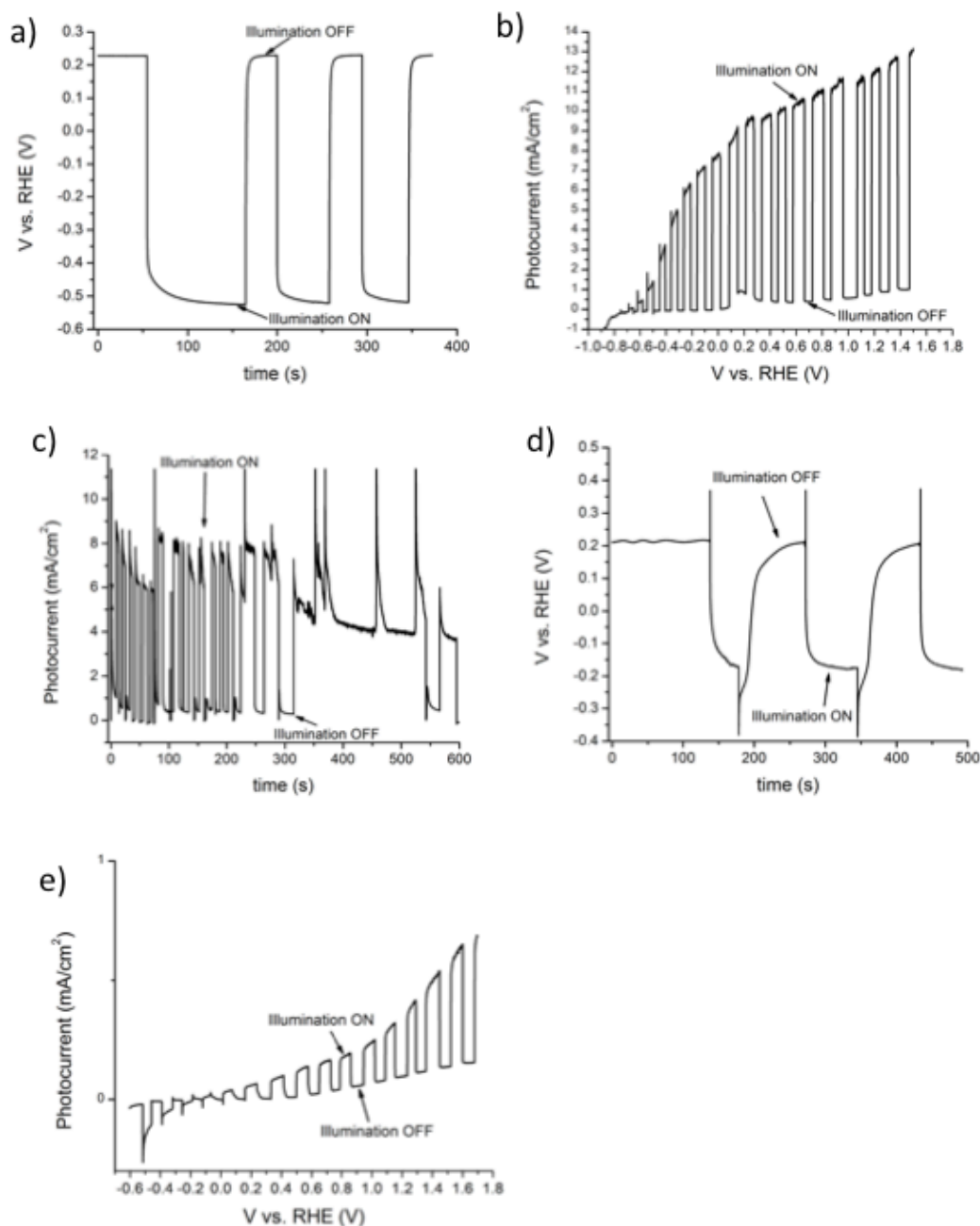


Figure 5.19 Fundamental PEC studies for samples A10 and A11, respectively, at 4 suns illumination in 1M sulfuric acid (pH = 0). (a,d) OCP under chopped illumination for 500+ seconds indicating n-type conductivity for both samples. (b) Unbiased two-electrode chronoamperometry measurements under chopped illumination for sample A10 exhibiting steady photocurrents between 4 mA/cm<sup>2</sup> and 8 mA/cm<sup>2</sup> for 10 minutes. (b,e) chopped illumination LSV measurements exhibiting approximately 11 mA/cm<sup>2</sup> and 0.02 mA/cm<sup>2</sup> maximum photocurrents under bias respectively.

Finally, PEC characterization was performed on sample A12. Figure 5.20a shows OCP for sample A12 indicating an appreciable photovoltage of .5 V. IV measurements, shown in Figure 5.20b, also yielded appreciable photocurrents of .5 mA/cm<sup>2</sup>. These are not nearly as high as those seen for sample A10 but are still very promising results.

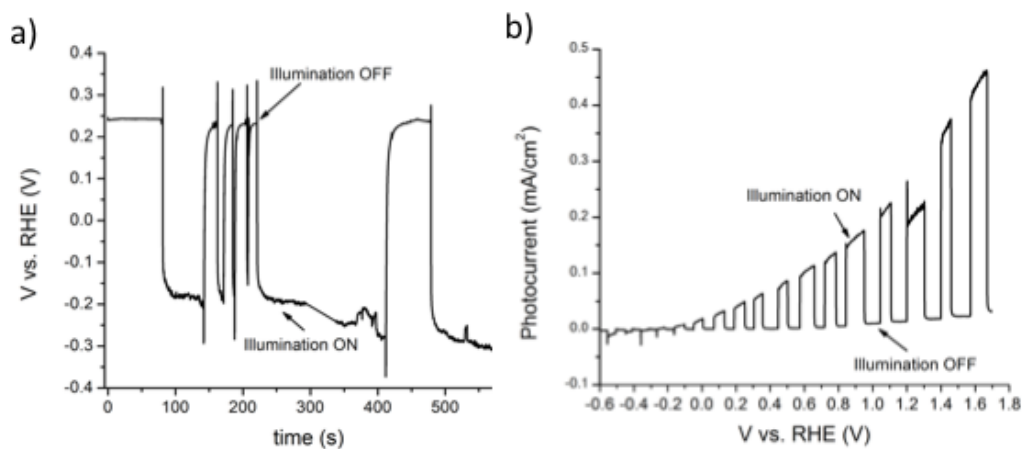


Figure 5.20 Fundamental PEC studies for sample A12 at 4 suns illumination in 3M sulfuric acid (pH = 0). (a) OCP under chopped illumination for 500+ seconds indicating n-type conductivity and (b) chopped illumination LSV measurements showed approximately 0.05 mA/cm<sup>2</sup> maximum photocurrents under bias.

Table 5.3 Summary of photoelectrochemical data obtained for relevant GaSb<sub>x</sub>P<sub>1-x</sub> samples A4 through A12 vs. the temperature at which they were deposited. Maximum photoactivities observed under bias and photoactivities at 0 V vs. RHE from LSV measurements are reported as well as the observed flatband potentials from OCP measurements. All samples were measured at 4 suns illumination while samples A4 and A6 were measured in sodium sulfate solution (pH 9-10) and samples A8-A12 were measured in 3 M sulfuric acid (pH = 0).

<b>Sample ID</b>	<b>Deposition Temperature (°C)</b>	<b>Maximum Photoactivity (mA/cm<sup>2</sup>)</b>	<b>Photoactivity at 0V vs RHE (mA/cm<sup>2</sup>)</b>	<b>FLATBAND POTENTIAL (V vs. Ag/AgCl)</b>
A4	625	.5	.3	-0.55
A6	660	.05	.005	-0.55
A8	620	3	1.5	-.65
A9	620	.2	.1	-0.35
A10	670	11	8	-0.55
A11	670	.02	.05	-0.2
A12	670	.05	.2	-0.25

Summary on photoelectrochemical performance: As can be observed from Table 6.3, each sample exhibits a flat band potential negative of the HER, implying that the conduction band and Fermi level of the synthesized semiconductors is appropriate to provide energetically favorable electrons to the counter-electrode that can drive the HER spontaneously under illumination. Furthermore, by incorporating what is known about the band gap from UV-Vis and PL, valence band positions can be obtained. The observed band placement based upon the flat-band potentials and band gaps for samples A4, A6 and A8-A12 are shown in Figure 6.21. As can be clearly seen. All samples

should straddle the watersplitting reaction with the exception of portions of A8, A9 and A10.

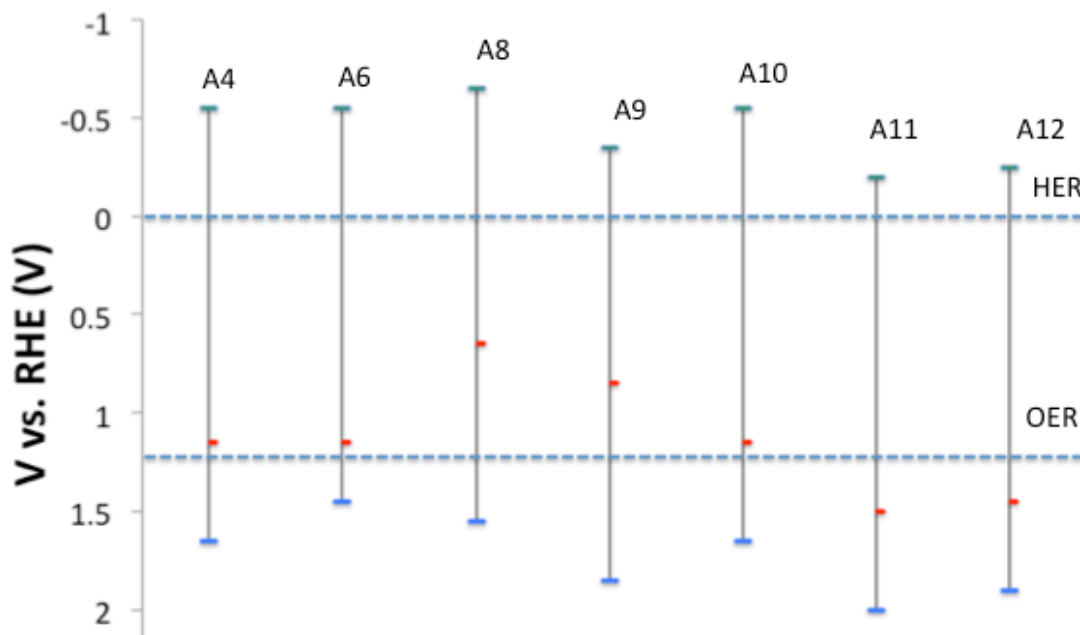


Figure 5.21 – Approximate band edge placement for each sample based upon the observed flatband potentials and band gaps. All samples exhibit n-type conductivity thus the observed flatband potential is used to place the conduction band for the material. The band gap is then used to determine the position of the valence band. The green marker indicates the conduction band energy level, the red marker represents the valence band level based upon the lowest observed bandgap and the blue marker represents the valence band level for the highest observed band gap.

Summary: The photoelectrochemical data observed for several samples grown using HVPE method are very promising. The data shows that the band edges of  $\text{GaSb}_x\text{P}_{1-x}$  films can straddle water splitting reactions for antimony concentrations between 4-6%. The photoelectrochemical performance of samples improved with crystallinity of the samples, i.e., crystallite size and orientation. The best performing sample (A10) utilized higher flow rates of  $\text{H}_2$  resulting in higher concentrations of Sb than any other sample and highly oriented crystallinity. This sample exhibited the highest photovoltage of more than .7 V and photoactivities of  $11 \text{ mA/cm}^2$  at 4 suns of illumination. Most importantly, the electrode also exhibited over  $2 \text{ mA/cm}^2$  under two electrode measurements indicating unassisted water splitting. As expected, improvements in crystallinity also yielded superior PEC performance such as in the case of samples A8 through A12, each exhibiting photovoltages in excess of .5 V. Samples A8 and A10 also had abrupt shut-off of the  $\text{PCl}_3$  precursor instead of gradually shutting off the  $\text{PCl}_3$  indicating that this gradual flow of  $\text{PCl}_3$  may have modified the surface in a way that makes it less photoactive.

Samples A8-A11 also contained higher amounts of antimony (between 4-6% Sb) and exhibited higher photovoltages than the samples with lower concentrations of Sb while still straddling the water splitting reaction. This increase in photoactivity could be a direct result of increased carrier mobility in the conduction band of GaSbP with increased Sb concentration. Lastly and most surprisingly, HVPE grown GaSbP samples are capable of providing the photovoltage and catalysis necessary for driving the OER and relatively stable with limited decrease in photoactivity after fundamental PEC testing and 10 minutes of continuous operation in highly acidic conditions ( $\text{pH} = 0$ ). GaP has

been stabilized for water oxidation as a photoanode utilizing  $\text{TiO}_2$  coating previously<sup>140</sup> but has not been shown to be stable for water oxidation as reported here.

The studies presented in this chapter uniquely establish  $\text{GaSb}_x\text{P}_{1-x}$  alloys as promising materials for both un-assisted and tandem cells for solar water splitting.



## CHAPTER 6

### CONCLUSIONS

The growth of gallium antimonide phosphide ( $\text{GaSb}_x\text{P}_{1-x}$ ) alloys within the regime of 0-10% antimonide composition is studied using reactive vapor transport and halide vapor phase epitaxy methods. The resulting films were characterized for structural, optical and photoelectrochemical activity for the water splitting reaction. The experimental results on structure and optical properties are compared with theoretical computations using the DFT+U technique. The following are the conclusions from this dissertation study.

DFT+U calculations predicted that the GaSbP alloys in the dilute antimonide regime will exhibit transition from indirect to direct band gap and straddling of conduction and valence band edge positions for water splitting reactions. Theoretical computations using DFT+U type methodology were specifically used to investigate the  $\text{GaSb}_x\text{P}_{(1-x)}$  alloy system with  $x$  ranging from 0 to 0.065. The computations predicted direct optical band gap transition for alloys containing  $x = 0.0092$  or more. Theoretical results also showed that for up to  $x = 0.065$ , the band edges straddle the HER and OER reactions.

Reactive vapor transport was utilized as an exploratory technique to synthesize

GaSbP NW alloys in the dilute antimonide regime as confirmed by electron microscopy and diffraction techniques.  $\text{GaSb}_x\text{P}_{(1-x)}$  nanowires were obtained using a reactive transport method without the use of any additional catalyst. TEM and SEM confirmed synthesis of single crystal  $\text{GaSb}_x\text{P}_{(1-x)}$  alloy NWs with uniform compositions of Ga, Sb and P. Sb concentrations in these NWs ranged from  $x=0.02$  to  $x=0.24$ . XRD both confirmed the presence of the  $\text{GaSb}_x\text{P}_{(1-x)}$  at the length scale of the sample, and that there is no GaP present in the samples. Most importantly, the experimental findings corroborate the DFT+U calculations which predicted the incorporation of Sb in the GaP lattice, without phase segregation at the studied concentrations, as well as the band gaps and band edge positions of the alloys with respect to water splitting.

Optical band gap measurements confirm an indirect to direct transition in dilute antimonide GaSbP alloys and fundamental PEC testing shows that GaSbP is photoactive. UV-Vis diffuse reflectance measurements taken over a  $1 \text{ cm}^2$  area of multiple samples, confirmed direct band gaps between 1.33 eV and 1.72 eV. Room temperature photoluminescence micro-measurements confirmed direct band gaps for  $\text{GaSb}_x\text{P}_{1-x}$  nanowires while cold photoluminescence (77 K) confirmed the lack of GaP. Photoelectrochemical linear sweep voltammetry measurements indicated the material is photoactive. OCP measurements indicated the alloy has an extrinsic p-type response and two electrode voltammetry showed a consistent photoresponse indicating the material straddles the water splitting reaction and is capable of splitting water as a photocathode in a Schottky type water splitting device.

A halide vapor phase epitaxy method was developed and used to grow highly oriented crystal morphology GaSbP films that exhibited direct band gaps from 1.2 to 2.2 eV. GaSb<sub>x</sub>P<sub>1-x</sub> alloys were grown using a custom-designed HVPE reactor using PCl<sub>3</sub>, hydrogen, Ga and Sb as precursors. Experiments using various III/V precursor flux ratios resulted in films with morphologies from microwire geometries to highly crystalline layers. Resulting films had antimony compositions up to 6% confirmed by both EDS and XRD techniques. Optical characterization using UV-Vis spectroscopy and room temperature photoluminescence spectroscopy (PL) showed direct band gaps in the range of 1.7 to 2.1 eV.

Fundamental photoelectrochemical testing of the HVPE samples unveiled HVPE grown GaSbP as highly photoactive electrodes for performing the OER with the champion sample showing a 0.75 V photovoltage and 8 mA/cm<sup>2</sup> at unbiased photocurrents that is relatively stable in highly acidic conditions under 4 suns illumination. Photoactivity of the samples seem to correlate with sample quality in terms of crystal size and film texturing. The sample exhibited stability under oxidizing conditions at this photoactivity for over 10 minutes of two electrode chronoamperometry measurements in highly acidic electrolyte (pH = 0). This photocurrent saturated at 11 mA/cm<sup>2</sup> at 1 V vs. Ag/AgCl external bias as seen in LSV measurements.

Synthesis of GaSbP in the dilute antimonide regime has been confirmed and it's indirect to direct band gap transition at these compositions along with its highly active photoelectrochemical properties as either a photocathode or photoanode for water

splitting have been confirmed thus corroborating exploratory DFT+U calculations. Highlights of both experimental and theoretical studies include the transition from indirect to direct band gap with minimal antimonide incorporation, and the straddling of the water splitting reaction under dilute antimony alloying. The data presented here represent first of its kind use of HVPE to grow GaSbP films and the photoelectrochemical studies suggest as significant activity for a semiconductor with unassisted water splitting.

## CHAPTER 7

### RECOMMENDATIONS

#### 7.1 Changes with reactor design and operation

The operation of the reactor can be made more reliable and easier to operate by making the following changes.

The first recommendation is the addition of a N<sub>2</sub> or Ar purge gas to allow the chamber to be purged and refilled with an inert gas during cooldown of the reactor. This would keep deposition from occurring during cooldown after the experiment has finished and may keep the formation of the varying compositional range microwires at the surface of the samples from occurring. Another recommendation is to utilize individual quartz tubes for each precursor. This will serve to both limit the amount of Ga produced during a reaction by splitting the gas flow into three isolated zones until it reaches the deposition zone and to keep the Ga from diffusing backwards and condensing at the Sb quartz boat. Furthermore, a carbon-coated quartz liner tube should be used at the deposition zone for each experiment and disposed of afterwards. This will keep deposition from accumulating in this area and presenting a health hazard when it is disturbed. This would also provide a method of reliably placing the substrate heater from the front of the reactor and accessing the back of the reactor where unwanted depositions occur, thus decreasing any safety risks associated with the reactor tremendously.

Accompanying this change should be a reconfiguration of the pyrometer to have a line of sight from the front of the reactor. The focus of the pyrometer is very accurate and has as much as a 60" focal length. This would easily allow for the measurement of the front of the substrate heater, through the entirety of the quartz tube from a viewport placed at the front of the reactor. In order to accomplish this, a T-junction will need to be installed at the front of the reactor in order to provide access for gases to enter the reactor. By moving the pyrometer to the front of the reactor, the gas clouds generated will no longer stop the pyrometer from losing line of sight to the substrate heater. Once the pyrometer is moved to the front of the reactor, the line of sight required from the back of the reactor will no longer be needed. This will allow installation of a manual valve immediately following the quartz tube adapter between the 4 way cross. By installing a manual valve here, the area of the reactor with unwanted depositions can be closed off while the precursor boats and substrate heater are removed from the stage, keeping the operator from being exposed from any of these unwanted deposits.

In order to keep the pressure control valve from getting stuck with metal condensation, a larger pressure control valve needs to be installed that can overcome these depositions readily. Foreline traps should be installed immediately following the pressure control. Metal mesh foreline traps are typically used for trapping condensation products, a sodasorb trap can be used to trap acidic gases and a carbon filter can be used to catch any other excess reactants. Alternatively, a liquid N<sub>2</sub> trap can be used to the same effect however this requires a dewar of liquid nitrogen on-hand to be used.

If the liquid N<sub>2</sub> trap were used, the dewar could also conveniently be used for the utilization of a dry gas pump in place of the rotary vane pump being used. Reaction of

the generated species with the current rotary vane pump oil causes a damage to the pump and added maintenance time. A dry pump does not use oil for lubrication and as such there is nothing for the exhaust gases to react with. Dry pumps are expensive and require liquid N<sub>2</sub> as previously stated however a dry pump may be necessary for reliable operation of the HVPE reactor.

After experimentation is done and the tube furnace is opened in order to vent heat faster, the temperature inside of the safety enclosure spikes to 140°F. In order to mitigate this as well as to provide a stronger negative pressure on the safety enclosure itself, a strong ventilation fan should be installed on the safety enclosure. As an added precaution, an inline carbon filter should be installed to catch any gases before they are vented from the safety enclosure. This endeavor is already underway.

A diagram of the reactor scheme after the recommended implementations has

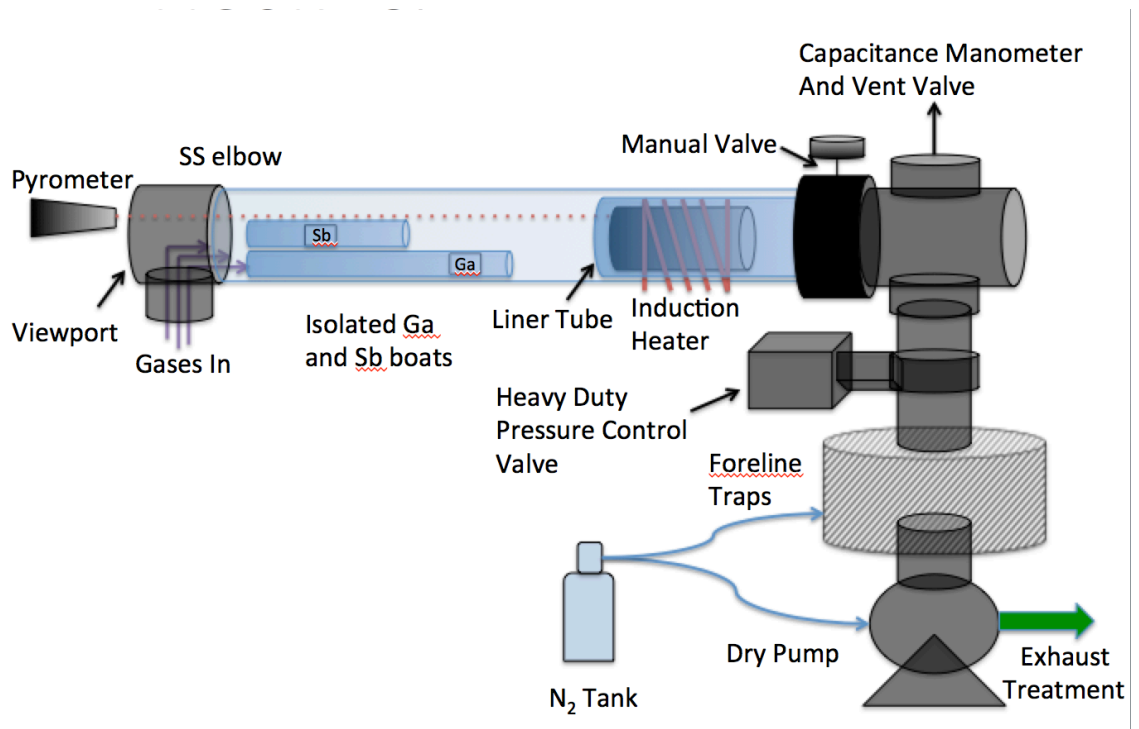


Figure 7.1 Reactor scheme after implementation of proposed changes

been made is seen in Figure 7.1. With these recommendations, future experimentation with the HVPE reactor should be much safer and more reliable.

## 7.2 Recommended experiments using HVPE

Future experiments are recommended to grow single crystalline, epitaxial films of varying thicknesses on silicon substrates using HVPE reactor. There is a large amount of parametric space for obtaining GaSbP alloys with different antimonide compositions. This can be done by performing a rigorous design of experiments around the Ga temperature zone to reliably tune the amount of moles of Ga generated during a reaction by weighing the precursors before and after an experiment. Once this is known, a Ga temperature that generates between 1.5 mmol and 26.4 mmol of Ga should be chosen. Once this is known, another design of experiments around the deposition temperatures should be performed in order to find the appropriate deposition for large-scale epitaxy to occur. Once large-scale epilayers have been grown at a given composition, changes in the available Sb and P for reaction should be changed in order to see if  $\text{GaSb}_x\text{P}_{1-x}$  should be grown throughout the compositional range. Experiments should also be undertaken to appropriately dope the epilayers either n-type or p-type. It will also be interesting to grow thin, single crystal layers of GaSbP using the existing MOCVD reactor.

## 7.3 Electrical and PEC device testing

Initial PEC characterization of HVPE grown GaSbP samples has shown them to be some of the best performing PEC materials grown to date. A future PEC experimentation path should look at the stability of the material, the effects of doping on the observed PEC



behavior, performance in a highly active redox couple and the addition of catalyst to the surface.

## REFERENCES

- 1 Sheetz, R. M. *et al.* Visible-light absorption and large band-gap bowing of GaN<sub>1-x</sub>Sb<sub>x</sub> from first principles. *Phys. Rev. B* **84**, 4, doi:10.1103/PhysRevB.84.075304 (2011).
- 2 G173-03(2012), A. (ASTM International, West Conshohocken, PA, 2012, <http://www.astm.org>, 2012).
- 3 Wang, D. *et al.* Wafer-Level Photocatalytic Water Splitting on GaN Nanowire Arrays Grown by Molecular Beam Epitaxy. *Nano Letters* **11**, 2353-2357, doi:10.1021/nl2006802 (2011).
- 4 Walter, M. G. *et al.* Solar water splitting cells. *Chemical reviews* **110**, 6446-6473 (2010).
- 5 Khaselev, O. & Turner, J. A. Electrochemical stability of p-GaInP<sub>2</sub> in aqueous electrolytes toward photoelectrochemical water splitting. *J. Electrochem. Soc.* **145**, 3335-3339, doi:10.1149/1.1838808 (1998).
- 6 Harrison, W. A. *Elementary electronic structure*. (World Scientific, 1999).
- 7 Lewis, N. S. & Nocera, D. G. Powering the planet: Chemical challenges in solar energy utilization. *Proceedings of the National Academy of Sciences* **103**, 15729-15735, doi:10.1073/pnas.0603395103 (2006).
- 8 Hansen, J. S., Makiko; Kharecha, Pushker; Beerling, David; Berner, Robert; Masson-Delmotte, Valerie; Pagani, Mark; Raymo, Maureen; Royer, Dana L.; Zachos, James C. Target Atmospheric CO<sub>2</sub>: Where Should Humanity Aim? *The Open Atmospheric Science Journal* **2**, 217-231 (2008).
- 9 OECD. *OECD Environmental Outlook to 2050* (2011).
- 10 Bard, A. J. & Fox, M. A. Artificial photosynthesis: solar splitting of water to hydrogen and oxygen. *Accounts Chem. Res.* **28**, 141-145 (1995).
- 11 Miller, E. L. Photoelectrochemical water splitting. *Energy Environ. Sci.* **8**, 2809-2810, doi:10.1039/C5EE90047F (2015).
- 12 Verlage, E. *et al.* A monolithically integrated, intrinsically safe, 10% efficient, solar-driven water-splitting system based on active, stable earth-abundant electrocatalysts in conjunction with tandem III-V light absorbers protected by amorphous TiO<sub>2</sub> films. *Energy Environ. Sci.* **8**, 3166-3172, doi:10.1039/C5EE01786F (2015).
- 13 Kuykendall, T., Ulrich, P., Aloni, S. & Yang, P. Complete composition tunability of InGaN nanowires using a combinatorial approach. *Nature materials* **6**, 951-956 (2007).
- 14 Kibria, M. G. *et al.* Visible light-driven efficient overall water splitting using p-type metal-nitride nanowire arrays. *Nat Commun* **6**, doi:10.1038/ncomms7797 (2015).

- 15 Nozik, A. J. P-N photoelectrolysis cells. *App. Phys. Letters* **29**, 150-153, doi:10.1063/1.89004 (1976).
- 16 Halmann, M. Photoelectrochemical reduction of aqueous carbon-dioxide on p-type gallium-phosphide in liquid junction solar-cells. *Nature* **275**, 115-116, doi:10.1038/275115a0 (1978).
- 17 McCann, J. F. & Handley, L. J. Photoelectrochemical effect at a p-GaP electrode. *Nature* **283**, 843-845, doi:10.1038/283843a0 (1980).
- 18 Dutta, P., Bhat, H. & Kumar, V. The physics and technology of gallium antimonide: An emerging optoelectronic material. *J. App. Phys.* **81**, 5821-5870 (1997).
- 19 Sunkara, S. *et al.* New Visible Light Absorbing Materials for Solar Fuels, Ga(Sbx)N<sub>1-x</sub>. *Advanced Materials* **26**, 2878-2882, doi:10.1002/adma.201305083 (2014).
- 20 Fujishima, A. & Honda, K. Photolysis-decomposition of water at the surface of an irradiated semiconductor. *Nature* **238**, 37-38 (1972).
- 21 Nozik, A. J. & Memming, R. Physical Chemistry of Semiconductor-Liquid Interfaces. *The Journal of Physical Chemistry* **100**, 13061-13078, doi:10.1021/jp953720e (1996).
- 22 Dudarev, S. L., Botton, G. A., Savrasov, S. Y., Humphreys, C. J. & Sutton, A. P. Electron-energy-loss spectra and the structural stability of nickel oxide: An LSDA+U study. *Physical Review B* **57**, 1505-1509 (1998).
- 23 Heinze, J. *Electrochemistry, Principles, Methods, and Applications.* Von C. M. A. Brett und A. M. O. Brett. Oxford University Press, Oxford, 1993. 427 S., Broschur 25.00 £. – ISBN 0-19-855388-9. *Angewandte Chemie* **106**, 2441-2442, doi:10.1002/ange.19941062240 (1994).
- 24 Bard, A. J. & Faulkner, L. R. *Electrochemical Methods: Fundamentals and Applications.* (Wiley, 2000).
- 25 Parsons, R. The electrical double layer: recent experimental and theoretical developments. *Chemical Reviews* **90**, 813-826, doi:10.1021/cr00103a008 (1990).
- 26 Nozik, A. J. Photoelectrochemistry: Applications to solar energy conversion. *Annual Review of Physical Chemistry* **29**, 189-222 (1978).
- 27 Bak, T., Nowotny, J., Rekas, M. & Sorrell, C. C. Photo-electrochemical hydrogen generation from water using solar energy. Materials-related aspects. *International Journal of Hydrogen Energy* **27**, 991-1022, doi:http://dx.doi.org/10.1016/S0360-3199(02)00022-8 (2002).
- 28 Varghese, O. K. & Grimes, C. A. Appropriate strategies for determining the photoconversion efficiency of water photoelectrolysis cells: A review with examples using titania nanotube array photoanodes. *Solar Energy Materials and Solar Cells* **92**, 374-384, doi:http://dx.doi.org/10.1016/j.solmat.2007.11.006 (2008).
- 29 Paracchino, A., Laporte, V., Sivula, K., Grätzel, M. & Thimsen, E. Highly active oxide photocathode for photoelectrochemical water reduction. *Nature materials* **10**, 456-461 (2011).

- 30 Quinn, R. K., Nasby, R. & Baughman, R. Photoassisted electrolysis of water using single crystal  $\alpha\text{-Fe}_2\text{O}_3$  anodes. *Materials Research Bulletin* **11**, 1011-1017 (1976).
- 31 Itoh, K. & Bockris, J. M. Thin film photoelectrochemistry: iron oxide. *J. Electrochem. Soc.* **131**, 1266-1271 (1984).
- 32 Rosso, K. M., Smith, D. M. & Dupuis, M. An ab initio model of electron transport in hematite ( $\alpha\text{-Fe}_2\text{O}_3$ ) basal planes. *The Journal of chemical physics* **118**, 6455-6466 (2003).
- 33 Hu, Y.-S. *et al.* Pt-doped  $\alpha\text{-Fe}_2\text{O}_3$  thin films active for photoelectrochemical water splitting. *Chemistry of Materials* **20**, 3803-3805 (2008).
- 34 Turner, J., Hendewerk, M., Parmeter, J., Neiman, D. & Somorjai, G. The characterization of doped iron oxide electrodes for the photodissociation of water stability, optical, and electronic properties. *J. Electrochem. Soc.* **131**, 1777-1783 (1984).
- 35 Kay, A., Cesar, I. & Grätzel, M. New benchmark for water photooxidation by nanostructured  $\alpha\text{-Fe}_2\text{O}_3$  films. *Journal of the American Chemical Society* **128**, 15714-15721 (2006).
- 36 Chernomordik, B. D. *et al.* Photoelectrochemical activity of as-grown,  $\alpha\text{-Fe}_2\text{O}_3$  nanowire array electrodes for water splitting. *Nanotechnology* **23**, 194009 (2012).
- 37 Miller, E., Rocheleau, R. & Deng, X. Design considerations for a hybrid amorphous silicon/photoelectrochemical multijunction cell for hydrogen production. *International Journal of Hydrogen Energy* **28**, 615-623 (2003).
- 38 Wang, H., Deutsch, T. & Turner, J. A. Direct water splitting under visible light with nanostructured hematite and  $\text{WO}_3$  photoanodes and a  $\text{GaInP}_2$  photocathode. *J. Electrochem. Soc.* **155**, F91-F96 (2008).
- 39 Gaillard, N., Chang, Y., Kaneshiro, J., Deangelis, A. & Miller, E. in *SPIE Solar Energy+ Technology*. 77700V-77700V-77714 (International Society for Optics and Photonics).
- 40 Pandey, P. K., Bhave, N. & Kharat, R. Spray deposition process of polycrystalline thin films of  $\text{CuWO}_4$  and study on its photovoltaic electrochemical properties. *Materials Letters* **59**, 3149-3155 (2005).
- 41 Chen, L. *et al.* Amorphous copper tungsten oxide with tunable band gaps. *Journal of Applied Physics* **108**, 043502 (2010).
- 42 Park, Y., McDonald, K. J. & Choi, K.-S. Progress in bismuth vanadate photoanodes for use in solar water oxidation. *Chemical Society Reviews* **42**, 2321-2337 (2013).
- 43 Kudo, A., Ueda, K., Kato, H. & Mikami, I. Photocatalytic  $\text{O}_2$  evolution under visible light irradiation on  $\text{BiVO}_4$  in aqueous  $\text{AgNO}_3$  solution. *Catalysis Letters* **53**, 229-230 (1998).
- 44 Bookbinder, D. C., Bruce, J. A., Dominey, R. N., Lewis, N. S. & Wrighton, M. S. Synthesis and characterization of a photosensitive interface for hydrogen generation: Chemically modified p-type semiconducting silicon photocathodes. *Proceedings of the National Academy of Sciences* **77**, 6280-6284 (1980).

- 45 Abdi, F. F. *et al.* Efficient solar water splitting by enhanced charge separation in a bismuth vanadate-silicon tandem photoelectrode. *Nat Commun* **4**, 2195, doi:10.1038/ncomms3195 (2013).
- 46 Han, L. *et al.* Efficient water-splitting device based on a bismuth vanadate photoanode and thin-film silicon solar cells. *ChemSusChem* **7**, 2832-2838, doi:10.1002/cssc.201402456 (2014).
- 47 Hamann, T. W. & Lewis, N. S. Control of the stability, electron-transfer kinetics, and pH-dependent energetics of Si/H<sub>2</sub>O interfaces through methyl termination of Si (111) surfaces. *The Journal of Physical Chemistry B* **110**, 22291-22294 (2006).
- 48 Nakato, Y., Yano, H., Nishiura, S., Ueda, T. & Tsubomura, H. Hydrogen photoevolution at p-type silicon electrodes coated with discontinuous metal layers. *Journal of electroanalytical chemistry and interfacial electrochemistry* **228**, 97-108 (1987).
- 49 Rocheleau, R. E., Miller, E. L. & Misra, A. High-efficiency photoelectrochemical hydrogen production using multijunction amorphous silicon photoelectrodes. *Energy & Fuels* **12**, 3-10 (1998).
- 50 Madan, A. & Shaw, M. P. *The physics and applications of amorphous semiconductors*. (Elsevier, 1988).
- 51 Zhu, F. *et al.* in *Solar Energy+ Applications*. 66500S-66500S-66509 (International Society for Optics and Photonics).
- 52 Zhu, F. *et al.* Amorphous silicon carbide photoelectrode for hydrogen production directly from water using sunlight. *Philosophical Magazine* **89**, 2723-2739 (2009).
- 53 Zhu, F. *et al.* Amorphous Silicon Carbide Photoelectrode for Hydrogen Production from Water using Sunlight. *Solar Energy, edited by Radu D. Rugescu, ISBN, 978-953* (2010).
- 54 Baglio, J. A. *et al.* Electrochemical characterization of p-type semiconducting tungsten disulfide photocathodes: efficient photoreduction processes at semiconductor/liquid electrolyte interfaces. *Journal of the American Chemical Society* **105**, 2246-2256 (1983).
- 55 Tributsch, H. & Bennett, J. Electrochemistry and photochemistry of MoS<sub>2</sub> layer crystals. I. *Journal of Electroanalytical Chemistry and Interfacial Electrochemistry* **81**, 97-111 (1977).
- 56 Wilcoxon, J. & Samara, G. Strong quantum-size effects in a layered semiconductor: MoS<sub>2</sub> nanoclusters. *Physical Review B* **51**, 7299 (1995).
- 57 Fernandez, A. *et al.* Photoelectrochemical characterization of the Cu (In, Ga) S<sub>2</sub> thin film prepared by evaporation. *Solar energy materials and solar cells* **85**, 251-259 (2005).
- 58 Repins, I. *et al.* 19.9% - efficient ZnO/CdS/CuInGaSe<sub>2</sub> solar cell with 81.2% fill factor. *Progress in Photovoltaics: Research and applications* **16**, 235-239 (2008).
- 59 Bar, M. *et al.* Determination of the band gap depth profile of the pentenary Cu (In (1-X) Ga X)(S Y Se (1-Y))<sub>2</sub> chalcopyrite from its composition gradient. *Journal of applied physics* **96**, 3857-3860 (2004).

- 60 Jackson, P. *et al.* New world record efficiency for Cu (In, Ga) Se<sub>2</sub> thin - film solar cells beyond 20%. *Progress in Photovoltaics: Research and Applications* **19**, 894-897 (2011).
- 61 Aharon - Shalom, E. & Heller, A. Efficient p - InP (Rh - H alloy) and p - InP (Re - H alloy) Hydrogen Evolving Photocathodes. *J. Electrochem. Soc.* **129**, 2865-2866 (1982).
- 62 Nozik, A. J. P-N PHOTOELECTROLYSIS CELLS. *Appl. Phys. Lett.* **29**, 150-153, doi:10.1063/1.89004 (1976).
- 63 Ginley, D. S. & Chamberlain, M. B. Interfacial chemistry at para-GaP photoelectrodes. *J. Electrochem. Soc.* **129**, 2141-2145, doi:10.1149/1.2124394 (1982).
- 64 Memming, R. & Schwandt, G. Electrochemical properties of gallium phosphide in aqueous solutions. *Electrochimica Acta* **13**, 1299-1310 (1968).
- 65 Huang, S. R., Xuesong, L., Barnett, A. & Opila, R. L. in *Photovoltaic Specialists Conference (PVSC), 2009 34th IEEE*. 000241-000243.
- 66 Olson, J. M., Aljassim, M. M., Kibbler, A. & Jones, K. M. MOCVD growth and characterization of GaP on Si. *J. Cryst. Growth* **77**, 515-523, doi:10.1016/0022-0248(86)90346-5 (1986).
- 67 Dietz, N., Miller, A., Kelliher, J. T., Venables, D. & Bachmann, K. J. MIGRATION-ENHANCED PULSED CHEMICAL BEAM EPITAXY OF GAP ON SI(001). *J. Cryst. Growth* **150**, 691-695, doi:10.1016/0022-0248(95)80297-p (1995).
- 68 Aspnes, D. & Studna, A. Dielectric functions and optical parameters of si, ge, gap, gaas, gasb, inp, inas, and insb from 1.5 to 6.0 ev. *Physical Review B* **27**, 985 (1983).
- 69 Dutta, P., Bhat, H. & Kumar, V. The physics and technology of gallium antimonide: An emerging optoelectronic material. *Journal of applied physics* **81**, 5821-5870 (1997).
- 70 Khaselev, O. & Turner, J. A. Electrochemical stability of p-GaInP<sub>2</sub> in aqueous electrolytes toward photoelectrochemical water splitting. *J. Electrochem. Soc.* **145**, 3335-3339, doi:10.1149/1.1838808 (1998).
- 71 Pendyala, C. *et al.* Nanowires as semi-rigid substrates for growth of thick, In<sub>x</sub>Ga<sub>1-x</sub>N (x > 0.4) epi-layers without phase segregation for photoelectrochemical water splitting. *Nanoscale* **4**, 6269-6275 (2012).
- 72 Maeda, K. *et al.* Photocatalyst releasing hydrogen from water. *Nature* **440**, 295-295 (2006).
- 73 Deutsch, T. G., Koval, C. A. & Turner, J. A. III-V nitride epilayers for photoelectrochemical water splitting: GaPN and GaAsPN. *The Journal of Physical Chemistry B* **110**, 25297-25307 (2006).
- 74 Jou, M. J., Cherng, Y. T., Jen, H. R. & Stringfellow, G. B. Organometallic vapor-phase epitaxial-growth of a new semiconductor alloy - GaP<sub>1</sub>-XSbX. *Appl. Phys. Lett.* **52**, 549-551, doi:10.1063/1.99413 (1988).
- 75 Loualiche, S. *et al.* GaPSb - A new ternary material for schottky diode fabrication on InP. *Appl. Phys. Lett.* **59**, 423-424, doi:10.1063/1.105450 (1991).

- 76 Shimomura, H., Anan, T. & Sugou, S. Growth of AlPSb and GaPSb on InP by gas-source molecular beam epitaxy. *J. Cryst. Growth* **162**, 121-125, doi:10.1016/0022-0248(95)00950-7 (1996).
- 77 Nakajima, K., Ujihara, T., Miyashita, S. & Sazaki, G. Thickness dependence of stable structure of the Stranski-Krastanov mode in the GaPSb/GaP system. *J. Cryst. Growth* **209**, 637-647, doi:10.1016/s0022-0248(99)00735-6 (2000).
- 78 Lo, S. T. *et al.* Electron transport in a GaPSb film. *Nanoscale Res. Lett.* **7**, 5, doi:10.1186/1556-276x-7-640 (2012).
- 79 Glasscock, J. A., Barnes, P. R., Plumb, I. C. & Savvides, N. Enhancement of photoelectrochemical hydrogen production from hematite thin films by the introduction of Ti and Si. *The Journal of Physical Chemistry C* **111**, 16477-16488 (2007).
- 80 Hu, Y.-S., Kleiman-Shwarsstein, A., Stucky, G. D. & McFarland, E. W. Improved photoelectrochemical performance of Ti-doped  $\alpha$ -Fe<sub>2</sub>O<sub>3</sub> thin films by surface modification with fluoride. *Chem. Commun.*, 2652-2654 (2009).
- 81 Ingler, W. B. & Khan, S. U. Photoresponse of spray pyrolytically synthesized copper-doped p-Fe<sub>2</sub>O<sub>3</sub> thin film electrodes in water splitting. *International Journal of Hydrogen Energy* **30**, 821-827 (2005).
- 82 Ingler, W. B. & Khan, S. U. A Self-Driven p/n - Fe<sub>2</sub>O<sub>3</sub> Tandem Photoelectrochemical Cell for Water Splitting. *Electrochemical and solid-state letters* **9**, G144-G146 (2006).
- 83 Ingler Jr, W. B. & Khan, S. U. Photoresponse of spray pyrolytically synthesized magnesium-doped iron (III) oxide (p-Fe<sub>2</sub>O<sub>3</sub>) thin films under solar simulated light illumination. *Thin Solid Films* **461**, 301-308 (2004).
- 84 Iordanova, N., Dupuis, M. & Rosso, K. M. Charge transport in metal oxides: a theoretical study of hematite  $\alpha$ -Fe<sub>2</sub>O<sub>3</sub>. *The Journal of chemical physics* **122**, 144305 (2005).
- 85 Kennedy, J. H. & Frese, K. W. Photooxidation of water at  $\alpha$  - Fe<sub>2</sub>O<sub>3</sub> electrodes. *J. Electrochem. Soc.* **125**, 709-714 (1978).
- 86 Beermann, N., Vayssieres, L., Lindquist, S. E. & Hagfeldt, A. Photoelectrochemical studies of oriented nanorod thin films of hematite. *J. Electrochem. Soc.* **147**, 2456-2461 (2000).
- 87 Chen, Z., Cvelbar, U., Mozetic, M., He, J. & Sunkara, M. K. Long-Range ordering of oxygen-vacancy planes in  $\alpha$ -Fe<sub>2</sub>O<sub>3</sub> nanowires and nanobelts. *Chemistry of Materials* **20**, 3224-3228 (2008).
- 88 Cvelbar, U., Chen, Z., Sunkara, M. K. & Mozetič, M. Spontaneous Growth of Superstructure  $\alpha$  - Fe<sub>2</sub>O<sub>3</sub> Nanowire and Nanobelt Arrays in Reactive Oxygen Plasma. *Small* **4**, 1610-1614 (2008).
- 89 Lindgren, T. *et al.* Aqueous photoelectrochemistry of hematite nanorod array. *Solar Energy Materials and Solar Cells* **71**, 231-243 (2002).
- 90 Jitputti, J., Suzuki, Y. & Yoshikawa, S. Synthesis of TiO<sub>2</sub> nanowires and their photocatalytic activity for hydrogen evolution. *Catalysis Communications* **9**, 1265-1271 (2008).

- 91 Park, J. H., Kim, S. & Bard, A. J. Novel carbon-doped TiO<sub>2</sub> nanotube arrays with high aspect ratios for efficient solar water splitting. *Nano letters* **6**, 24-28 (2006).
- 92 Khan, S. U. & Sultana, T. Photoresponse of n-TiO<sub>2</sub> thin film and nanowire electrodes. *Solar energy materials and solar cells* **76**, 211-221 (2003).
- 93 Ahn, K.-S. *et al.* Enhancement of photoelectrochemical response by aligned nanorods in ZnO thin films. *Journal of Power Sources* **176**, 387-392 (2008).
- 94 Green, M. A. Solar cell efficiency tables (version 46). *Prog. in Photovoltaics* **23**, 1202-1202, doi:10.1002/pip.2667 (2015).
- 95 Bliss, D., Tassev, V., Weyburne, D. & Bailey, J. Aluminum nitride substrate growth by halide vapor transport epitaxy. *J. Cryst. Growth* **250**, 1-6 (2003).
- 96 Leroux, M. *et al.* Comparative optical characterization of GaN grown by metal-organic vapor phase epitaxy, gas source molecular beam epitaxy and halide vapor phase epitaxy. *Materials Science and Engineering: B* **43**, 237-241 (1997).
- 97 Kim, D. H., Farva, U., Jung, W. S., Kim, E. J. & Park, C. Epitaxial growth of GaN on (0001) Al<sub>2</sub>O<sub>3</sub> via solution-cast seed layer formation process using Ga (mDTC) 3. *Korean Journal of Chemical Engineering* **25**, 1184-1189 (2008).
- 98 Hemmingsson, C., Pozina, G., Khromov, S. & Monemar, B. Growth of GaN nanotubes by halide vapor phase epitaxy. *Nanotechnology* **22**, 085602 (2011).
- 99 Takahashi, N. *et al.* Growth of InN pillar crystal films by means of atmospheric pressure halide chemical vapor deposition. *Journal of Materials Chemistry* **12**, 1573-1576 (2002).
- 100 Yoshioka, M., Takahashi, N. & Nakamura, T. Growth of the AlN nano-pillar crystal films by means of a halide chemical vapor deposition under atmospheric pressure. *Materials chemistry and physics* **86**, 74-77 (2004).
- 101 Sanders, A. *et al.* Homoepitaxial n-core: p-shell gallium nitride nanowires: HVPE overgrowth on MBE nanowires. *Nanotechnology* **22**, 465703 (2011).
- 102 Darakchieva, V., Monemar, B., Usui, A., Saenger, M. & Schubert, M. Lattice parameters of bulk GaN fabricated by halide vapor phase epitaxy. *J. Cryst. Growth* **310**, 959-965 (2008).
- 103 Fialho, M. *et al.* Lattice site location and luminescence studies of Al<sub>x</sub>Ga<sub>1-x</sub>N alloys doped with thulium ions. *Nuclear Instruments and Methods in Physics Research Section B: Beam Interactions with Materials and Atoms* **307**, 495-498 (2013).
- 104 Zhang, R. & Kuech, T. F. Photoluminescence of carbon in situ doped GaN grown by halide vapor phase epitaxy. *Appl. Phys. Lett.* **72**, 1611-1613 (1998).
- 105 Kovalenkov, O., Soukhoveev, V., Ivantsov, V., Usikov, A. & Dmitriev, V. Thick AlN layers grown by HVPE. *J. Cryst. Growth* **281**, 87-92 (2005).
- 106 Kumagai, Y., Kikuchi, J., Nishizawa, Y., Murakami, H. & Koukitu, A. Hydride vapor phase epitaxy of InN by the formation of InCl<sub>3</sub> using In metal and Cl<sub>2</sub>. *J. Cryst. Growth* **300**, 57-61 (2007).
- 107 Koukitu, A. & Kumagai, Y. Thermodynamic analysis of group III nitrides grown by metal-organic vapour-phase epitaxy (MOVPE), hydride (or halide)



- vapour-phase epitaxy (HVPE) and molecular beam epitaxy (MBE). *Journal of Physics: Condensed Matter* **13**, 6907 (2001).
- 108 Kumagai, Y., Takemoto, K., Koukitu, A. & Seki, H. Thermodynamics on halide vapor-phase epitaxy of InN using InCl and InCl<sub>3</sub>. *J. Cryst. Growth* **222**, 118-124 (2001).
- 109 Kumagai, Y., Takemoto, K., Hasegawa, T., Koukitu, A. & Seki, H. Thermodynamics on tri-halide vapor-phase epitaxy of GaN and In<sub>x</sub>Ga<sub>1-x</sub>N using GaCl<sub>3</sub> and InCl<sub>3</sub>. *J. Cryst. Growth* **231**, 57-67 (2001).
- 110 Takahashi, N., Ogasawara, J. & Koukitu, A. Vapor phase epitaxy of InN using InCl and InCl<sub>3</sub> sources. *J. Cryst. Growth* **172**, 298-302 (1997).
- 111 Hemmingsson, C., Monemar, B., Kumagai, Y. & Koukitu, A. in *Springer Handbook of Crystal Growth* (eds Govindhan Dhanaraj, Kullaiyah Byrappa, Vishwanath Prasad, & Michael Dudley) 869-896 (Springer Berlin Heidelberg, 2010).
- 112 Koukitu, A. *et al.* Solid Composition of In<sub>1-x</sub>Ga<sub>x</sub>As Grown by the Halogen Transport Atomic Layer Epitaxy. *Japanese journal of applied physics* **27**, L744 (1988).
- 113 Taki, T. & Koukitu, A. Atomic layer epitaxy of GaAs using GaBr and GaI sources. *Applied surface science* **112**, 127-131 (1997).
- 114 Mottram, A., Peaker, A. & Sudlow, P. The Growth of Epitaxial Gallium Phosphide from the Vapor Phase by Halogen Transport. *J. Electrochem. Soc.* **118**, 318-324 (1971).
- 115 Park, J., Barnes, P., Tin, C. & Allerman, A. Lateral overgrowth and epitaxial lift-off of InP by halide vapor-phase epitaxy. *J. Cryst. Growth* **187**, 185-193 (1998).
- 116 Andriotis, A. N., Mpourmpakis, G., Lisenkov, S., Sheetz, R. M. & Menon, M. U-calculation of the LSDA + U functional using the hybrid B3LYP and HSE functionals. *Phys. Stat. Sol. (b)* **250**, 356-363, doi:10.1002/pssb.201248215 (2013).
- 117 Nakamura, H., Hayashi, N., Nakai, N., Okumura, M. & Machida, M. First-principle electronic structure calculations for magnetic moment in iron-based superconductors: An LSDA + negative U study. *Physica C: Superconductivity* **469**, 908-911, doi:10.1016/j.physc.2009.05.096 (2009).
- 118 Jang, J. K. & Rhee, J. Y. Magnetic states of iron-based superconducting compounds: A comparative study with Fe<sub>3</sub>Al alloy. *Journal of the Korean Physical Society* **66**, 646-650 (2015).
- 119 Paudel, T. R. & Lambrecht, W. R. First-principles calculation of the O vacancy in ZnO: A self-consistent gap-corrected approach. *Physical Review B* **77**, 205202 (2008).
- 120 Persson, C. & Mirbt, S. Improved electronic structure and optical properties of sp-hybridized semiconductors using LDA+ U SIC. *Brazilian journal of physics* **36**, 286-290 (2006).
- 121 Fukushima, T. *et al.* Computational materials design of negative effective U system in hole-doped chalcopyrite CuFeS<sub>2</sub>. *Journal of Physics: Condensed Matter* **26**, 355502 (2014).

- 122 Sarma, D., Mahadevan, P., Saha-Dasgupta, T., Ray, S. & Kumar, A. Electronic Structure of Sr<sub>2</sub>FeMoO<sub>6</sub>. *Physical review letters* **85**, 2549 (2000).
- 123 Perdew, J. P., Burke, K. & Ernzerhof, M. Generalized gradient approximation made simple. *Phys. Rev. Lett.* **77**, 3865-3868 (1996).
- 124 Kresse, G. & Hafner, J. Ab initio molecular dynamics for liquid metals. *Phys. Rev. B* **47**, 558-561 (1993).
- 125 Kresse, G. & Joubert, D. From ultrasoft pseudopotentials to the projector augmented-wave method. *Phys. Rev. B* **59**, 1758-1775 (1999).
- 126 Blöchl, P. E. Projector augmented-wave method. *Phys. Rev. B* **50**, 17953-17979 (1994).
- 127 Dean, P. Inter-impurity recombinations in semiconductors. *Progress in Solid State Chemistry* **8**, 1-126 (1973).
- 128 Kopylov, A. & Pikhtin, A. Shallow impurity states and the free exciton binding energy in gallium phosphide. *Solid State Communications* **26**, 735-740 (1978).
- 129 Bergh, A. A. & Dean, P. J. Light-emitting diodes. *Oxford, Clarendon Press, 1976. 598 p 1* (1976).
- 130 Fazzio, A., Brescansin, L. & Leite, J. Electronic structure of neutral and negatively charged gallium vacancies in GaP. *Journal of Physics C: Solid State Physics* **15**, L1 (1982).
- 131 Makiuchi, N., Leite, J. & Fazzio, A. Electronic structure of a single neutral ideal phosphorus vacancy in GaP. *Journal of Physics C: Solid State Physics* **17**, 3423 (1984).
- 132 Hinuma, Y., Oba, F., Kumagai, Y. & Tanaka, I. Ionization potentials of (112) and (112-) facet surfaces of CuInSe and CuGaSe. *Phys. Rev. B* **86**, 245433 (2012).
- 133 Grüneis, A., Kresse, G., Hinuma, Y. & Oba, F. Ionization potentials of solids: The importance of vertex corrections. *Phys. Rev. Lett.* **112**, 096401 (2014).
- 134 Andriotis, N. A., Sheetz, R. M., Ernst, R. & Madhu, M. Band alignment and optical absorption in Ga(Sb)N alloys. *J. Phys: Cond. Matt.* **26**, 055013 (2014).
- 135 Harrison, W. A. & Tersoff, J. Tight - binding theory of heterojunction band lineups and interface dipoles. *J. Vac. Sci. Tech. B* **4**, 1068-1073, doi:10.1116/1.583544 (1986).
- 136 Harrison, W. H. *Elementary Electronic Structure*. Revised edn, (World Scientific, 2004).
- 137 Dean, P. Inter-impurity recombinations in semiconductors. *Prog. Solid State Chem.* **8**, 1-126 (1973).
- 138 Fazzio, A., Brescansin, L. & Leite, J. Electronic structure of neutral and negatively charged gallium vacancies in GaP. *J. Phys. C: Solid State Phys.* **15**, L1 (1982).
- 139 Jalilian, R., Sumanasekera, G. U., Chandrasekharan, H. & Sunkara, M. K. Phonon confinement and laser heating effects in Germanium nanowires. *Phys. Rev. B* **74**, 6, doi:10.1103/PhysRevB.74.155421 (2006).

- 140 Hu, S. *et al.* Amorphous TiO<sub>2</sub> coatings stabilize Si, GaAs, and GaP photoanodes for efficient water oxidation. *Science* **344**, 1005-1009, doi:10.1126/science.1251428 (2014).

## CURRICULUM VITAE

Harry Russell

### EDUCATION

PhD Chemical Engineering (May 2016), University of Louisville, Louisville, Kentucky

Advisor: Dr. Mahendra Sunkara, GPA: 3.51/4.0

Masters of Engineering in Chemical Engineering (May 2011) Chemical Engineering,

University of Louisville, Louisville, Kentucky GPA: 3.51/4.0

Bachelor of Science in Chemical Engineering (May 2009) Chemical Engineering,

University of Louisville, Louisville, Kentucky GPA: 3.05/4.0

### SKILLS

- Six years research experience in synthesis of materials for photo-electrochemical water splitting;
- Designed and built reactor for III-V deposition utilizing halide precursors
- Regular maintenance and ownership of Atmospheric Microwave Plasma Discharge reactor, trained fellow students on operating this reactor

- Hands on experience in troubleshooting of Atmospheric Plasma, Atomic Layer Deposition, Sulfurization and Hot-wire CVD reactor.
- Extensive Materials Characterization using techniques like Scanning Electron Microscopy, X-Ray Diffraction, and UV- Vis Spectroscopy.
- Photoelectrochemical Characterization of semiconductors
- Installed Atmospheric Plasma Reactor for Mass Production of MO Nanowires
- *Acted as safety officer for the lab*

## RESEARCH EXPERIENCE

Research Assistant, Conn Center, U of Louisville (Aug. 2010 – Present)

- Rebuilt a sulfurization reactor that led to more productivity and safety
- Synthesized novel GaP based alloys using reactive plasma transport in the low antimonide regime.
- Developed systematic fundamental photoelectrochemical characterization to understand the factors affecting the photoelectrochemical performance
- Developed methodology for synthesizing highly oriented hematite nanowire arrays using atmospheric microwave plasma oxidation.
- Teaching assistant for chemical vapor deposition

## PUBLICATIONS

1. H.B. Russell, A.N. Andriotis, M. Menon, J. Jasinski and M.K. Sunkara, “Direct Band Gap Gallium Antimony Phosphide ( $\text{GaSb}_x\text{P}_{1-x}$ ) Alloys”, Nature Scientific Reports 2016

2. B. Chernomordik, H.B. Russell, V. Kumar, J. Jasinski, U. Cvelbar and M.K. Sunkara, "Photoelectrochemical performance of plasma grown  $\alpha$ -Fe<sub>2</sub>O<sub>3</sub> NW arrays on iron foils", Nanotechnology (May 2012)
3. M K Sunkara, C Pendyala, D Cummins, P Meduri, J. Jasinski, V Kumar, H B Russell, E L Clark, and J H Kim, "Inorganic nanowires: a perspective about their role in energy conversion and storage applications", J. Phys. D, 44, 174032 (2011)
4. P. Meduri, J.H. Kim, H.B. Russell, J. Jasinski, G.U. Sumanasekera and M.K. Sunkara, "Thin Walled Carbon Microtubes as High Capacity and High Rate Anodes in Lithium Ion Batteries", J. Phys. Chem. C., 114, 10621 (2010)
5. S. Gubbala, H. B. Russell, H. Shah, B. Deb, J. Jasinski, H. Rypkema, M. K. Sunkara, "Surface properties of SnO<sub>2</sub> nanowires for enhanced performance with dye-sensitized solar cells", Energy Environ. Science, 2, 1302-1309 (2009).

#### US PATENTS

1. Sunkara, M.K., Vendra, V, Russell, H.B., Encapsulation of Perovskite Materials, invention disclosure completed, seeking provisional patent.

#### CONFERENCE PRESENTATIONS

1. D. R. Cummins, H. B. Russell, J. B. Jasinski, M. Menon, and M. K. Sunkara, Iron Sulfide (FeS) Nanotubes Using Phase Transformation of Hematite Nanowires,

MRS Fall 2013, Poster Presentation, 12/4/13, Boston, MAAICHE (I know I need to put all the information for this)

2. H. B. Russell; U. Cvelbar; J. Jasinski; T. Deutsch; M. Sunkara, Plasma Oxidation of Iron Foils to Synthesize Hematite Nanowire Arrays for Photoelectrochemical Water Splitting Z2.10, Oral, MRS Spring Meeting, San Francisco, CA, April 1-5 (2013).
3. H. B. Russell, U. Cvelbar, J. B. Jasinski, T. G. Deutsch and M.K. Sunkara, "Photoelectrochemical Activity of Hematite Nanowire Arrays Synthesized Using Plasmas for Poster presentation in Renewable Energy and Fuels, 222<sup>nd</sup> meeting of the Electrochemical Society, Oct. 7-12,2012,Honolulu,Hawaii
4. D. Cummins, H. Russell, J. Jasinski, M. Sunkara, "Transformation of Hematite Nanowires into One-Dimensional Pyrite Nanostructures", 2012 Materials Research Society Fall Meeting, Nov. 25-30, 2012, Boston, MA.
5. D. Cummins, H. Russell, J.Jasinski, and M. Sunkara, "Synthesis of Phase Pure Pyrite Nanowires/Nanotubes for Solar Energy Applications", PRiME 2012, Oct 7-12, 2012, Honolulu, HI.
6. S. Gubbala, H. Russell, H. Shah,B. Deb, J. Jasinski, H. Rypkema, and M.K. Sunkara, "Surface Properties of SnO<sub>2</sub> Nanowires forEnhanced Performance with Dye-sensitized Solar Cells", 216<sup>th</sup> Electrochemical Society Meeting, Vienna, Austria, October 4-9, 2009.

## AWARDS

- Third Prize for Poster presentation at RE3 workshop, Louisville, KY (2013)

## COURSEWORK

- Specialized graduate courses on Chemical Vapor Deposition, Micro Electro Mechanical Systems (MEMS), Semiconductor Principles, Materials Characterization, Electroanalytical Chemistry, Energy and Environmental Science;
- Trained on photoelectrochemical characterization of semiconductors at Joint Center for Artificial Photosynthesis winter school, CALTECH, Pasadena , CA
- Trained on making electrical contacts for solar water splitting at NREL, Colorado

## MENTORSHIP AND OUTREACH

- Founded the RE3 club and acted as officer from 2010 to 2012
- Mentored multiple undergraduate and high school students.
- Participated in outreach efforts at the Louisville Science Center, Forecastle Music Festival and University events; hands-on workshops for assembling dye sensitized solar cells for a wide range of participants.
- Held bourbon tastings for Conn Center events.